

Czech Technical University in Prague
Faculty of Information Technology
Department of Theoretical Computer Science



Texture modeling applied to medical images

by

Václav Remeš

A dissertation thesis submitted to
the Faculty of Information Technology, Czech Technical University in Prague,
in partial fulfilment of the requirements for the degree of Doctor.

Dissertation degree study programme: Informatics

Prague, August 2017

Supervisor:

Prof. Ing. Michal Haindl, DrSc.
Department of Theoretical Computer Science
Faculty of Information Technology
Czech Technical University in Prague
Thákurova 9
160 00 Prague 6

Department of Pattern Recognition
Institute of Information Theory and Automation
Czech Academy of Sciences
Pod Vodárenskou Věží 4
182 08 Prague 8
Czech Republic

Copyright © 2017 Václav Remeš

Abstract and contributions

This thesis presents novel descriptive multidimensional Markovian textural models applied to computer aided diagnosis in the field of X-ray mammography. These general mathematical models, applicable in wide areas of texture modeling outside X-ray mammography as well, provide ideal visual verification using synthesis of the corresponding measured data spaces, contrary to standard discriminative models. All achieved results in the thesis are extensively benchmarked.

The thesis presents two methods for breast density classification in X-ray mammography. The methods were tested on the widely known MIAS database and the state-of-the art INbreast database, with competitive results.

Several methods for completely automatic mammogram texture enhancement are presented. These methods are based on the descriptive textural models developed in the thesis which automatically adapt to the analyzed X-ray texture, thus being universal for any type of input without the need of further manual tuning of specific parameters. The methods' outputs highlight regions of interest, detected as textural abnormalities. The methods provide the possibility of enhancement tuned to specific types of mammogram tissue. Hence, the enhanced mammograms can help radiologists to decrease their false negative evaluation rate. It has been shown that the algorithms work well both for small findings, such as microcalcifications, and for bigger lesions.

The pseudocolour method offers a unique way of mammogram feature fusion for visual evaluation and vastly enriches the the information content of the enhanced mammogram. The results were verified also by radiologist consultants.

New contrast criterion was implemented which outperforms previously published contrast criteria.

The focus of our study is mammogram texture and the following search for its optimal mathematical representation.

The main contributions of the dissertation thesis are as follows:

1. Descriptive multidimensional texture models development for texture analysis and synthesis applications

-
- a) Hierarchical Potts MRF model
 - b) Directional CAR models
 - c) Spiral CAR models
 - d) Compound Potts MRF model (CMRF^{P3AR})
 - e) Compound Potts Voronoi MRF model (CMRF^{PV3AR})
 - f) Algorithm for estimation of Potts model parameters for texture mimicking
2. X-ray mammograms tissue analysis based on the descriptive multidimensional texture models
 - a) Algorithm for breast composition classification
 - o A sub-result is the classification of texture in mammograms into fatty and dense
 - b) Potts model based classification of breast composition
3. Development of methods for mammogram parenchymal patterns enhancement
 - a) Unilateral method for mammogram enhancement with three specific tissue targeted outputs
 - b) Nonrigid bilateral comparison method
 - c) Texture model based bilateral comparison method
 - d) Pseudocolour enhancement method
4. Development of image enhancement criteria and their verification
 - a) Contrast criteria comparison using our benchmark
 - b) Region contrast criterion SRC which passes all our benchmarking conditions

Keywords:

mammography, Markov random fields, texture analysis, texture synthesis, computer aided diagnosis, image enhancement, image classification, contrast criteria.

Acknowledgements

First of all, I would like to express my gratitude to my dissertation thesis supervisor, Prof. Michal Haindl. He has been a constant source of encouragement and insight during my research and helped me with numerous problems and professional advancements.

I would like to thank MUDr. Alena Bílková, PhD., MUDr. Jana Frýbová, MUDr. Hana Kacerovská, CSc., MUDr. Petra Steyerová and MUDr. Jana Žížalová for the consultations they gave me on mammography and their willingness to discuss the results of our methods.

Special thanks go to my colleagues from the Department of Pattern Recognition of the Institute of Information Theory and Automation, who maintained a pleasant and flexible environment for my research. I would like to express special thanks to the department management for providing most of the funding for my research.

My research has also been partially supported by the Czech Science Foundation as project No. 14-10911S, and by the Czech Science Foundation as project No. 102/08/0593.

Finally, my greatest thanks go to my family members, for their infinite patience and love.

Dedication

To my family.

Without your love and support, this wouldn't have been possible.

Contents

Abbreviations	xvii
1 Introduction	1
1.1 Motivation	1
1.1.1 Texture modeling	1
1.1.2 Mammography	1
1.1.3 Contrast	2
1.2 Problem Statement	2
1.3 Goals of the Dissertation Thesis	3
1.4 Structure of the Dissertation Thesis	3
2 Background and State-of-the-Art	5
2.1 Theoretical Background	5
2.1.1 Texture Representation	5
2.1.2 Gaussian Mixtures	11
2.1.3 Extremal Regions	13
2.1.4 Mammography	14
2.2 Previous Results and Related Work	18
2.2.1 Breast Segmentation	18
2.2.2 Microcalcification Segmentation	18
2.2.3 Breast Texture Analysis	19
2.2.4 Breast Density Analysis	19
2.2.5 Texture Enhancement	19
2.2.6 CC - MLO Pseudoregistration	21
2.2.7 Bilateral and Temporal Registration	21
2.2.8 Contrast Measures	22
2.2.9 Texture Synthesis	25
3 Experimental Data	27

3.1	Public Mammogram Databases	27
3.1.1	INbreast	28
3.1.2	MIAS	28
3.1.3	DDSM	29
3.2	UTIA Pattern Recognition Department's Texture Database	30
3.3	Dermatological Data	30
4	Texture Models	31
4.1	Potts MRF	31
4.1.1	Surrogate Potts Model Parameters	31
4.1.2	Hierarchical Potts model	32
4.2	CAR Model Generalizations	35
4.2.1	Directional CAR models	36
4.2.2	Spiral Models	36
5	Texture Synthesis	41
5.1	Hierarchical Potts Synthesis	41
5.1.1	Compound Markov Model	42
5.1.2	Region Switching Markov Model	42
5.1.3	Modified SW Synthesis	43
5.2	Mosaics	43
5.2.1	Potts Field-Based Mosaic Modeling	44
5.3	Local Markov Models	46
5.4	Results	49
5.4.1	CMRF ^{P3AR} results	49
5.4.2	CMRF ^{PV3AR} results	50
6	Breast Tissue Density Classification	53
6.1	Breast Segmentation	53
6.2	Maximal Texture Type Occurrence Based Classification	54
6.2.1	Breast Texture Description	54
6.2.2	Classifier Training	55
6.2.3	Feature Space Visualisation	55
6.2.4	Breast Density Classification	56
6.2.5	Results	56
6.2.6	Comparison with Leading Methods	57
6.3	2DCAR Parameter Analysis	58
6.3.1	Optimizing Neighbourhood	58
6.3.2	Exponential Forgetting Factor	61
6.4	Potts-based Classification Using Extremal Regions	62
7	Mammogram Texture Enhancement	65
7.1	Unilateral Enhancement	65

7.2	Bilateral and Temporal Enhancement	66
7.2.1	Bilateral Analysis - Nonrigid Approach	68
7.2.2	Texture Model Based Bilateral Comparison	70
7.2.3	Discussion	75
7.3	Pseudo Color Enhancement	76
7.3.1	Comparison with alternative methods	79
7.3.2	Contrast measures	79
7.3.3	Numerical contrast results	79
7.3.4	Numerical Evaluation	79
7.3.5	Visual Evaluation	83
7.3.6	Radiologists' Verification	86
8	Local Contrast Criteria	89
8.1	Contrast Measure Categories	89
8.1.1	Modifying Contrast Measures for Regions of Interest	90
8.2	Our Proposed Contrast Criterion	91
8.3	Contrast Measures Benchmarking	91
8.4	Experimental Validation	91
9	Developed Software	97
9.1	Potts Applications	97
9.1.1	Hierarchical Potts Texture Mimicking	97
9.1.2	Potts Mosaics	98
9.2	Mammograms	98
9.2.1	Graphical User Interface	98
9.2.2	Unified Interface for Mammogram Databases	99
9.3	Supervised Texture Model Based Segmentation	99
9.4	Storing and Analyzing Results	101
9.5	Parametrizing Runnables	102
9.6	External Libraries Used	105
10	Conclusions	107
10.1	Contributions	108
10.2	Future Work	109
10.2.1	Mammography Analysis	109
10.2.2	Multidimensional Random Fields	110
	Bibliography	111
	Reviewed Publications of the Author Relevant to the Thesis	123
	Remaining Publications of the Author Relevant to the Thesis	125
A	Unsupervised segmentation results	127

List of Figures

2.1	Example of a sampled Potts model with 10 colours.	10
2.2	Swendsen-Wang algorithm step.	11
2.3	Explanation of the BTF space measurements.	12
2.4	Example of a cranio-caudal view (left) and a medio-lateral oblique view (right) of a mammogram.	15
2.5	Example of clustered microcalcifications scattered inside a tiny cancer in the center of the image (left) and several lymphatic nodes inside the pectoral muscle (right).	15
2.6	Example of an asymmetry between the left and right breasts (left and middle). Image shown on the right displays an example of a mass.	16
2.7	Example mammograms with different density values - left to right consequently contain BI-RADS densities 1, 2, 3 and 4.	18
3.1	Example of images from different mammogram databases.	28
3.2	Example of textures from our database.	30
3.3	Example of dermatological images.	30
4.1	Two seemingly equal realizations of Potts model. Left $\beta = 2$, right $\beta = 3.15$	32
4.2	Plot of the β parameter and surrogate parameters for the Potts model. Top: development during synthesis starting at noise, bottom: development for progressive noise reduction.	33
4.3	Synthesized Potts random field successively smoothed by a max-occurrence filter.	34
4.4	Typical problem of the CAR model – causality inertia.	35
4.5	The paths of the two “spirals” in an image.	37
4.6	Rectangular spiral, left to right: original, α_1 , α_2 , α_3	38
4.7	Octagonal spiral, left to right: original, α_1 , α_2 , α_3	39
5.1	Control field synthesis algorithm flowchart.	45

5.2	The original images of a floor (upper row left) and nacre stone (upper row right). Corresponding synthetic control fields - Voronoi Potts model (middle row), and the resulting synthetic CMRF ^{PV3AR} model texture (bottom row).	47
5.3	The nacre stone texture mapped to a 3D model created with Blender (left) and with synthetic texture (right).	48
5.4	Texture synthesis of a stained glass window.	48
5.5	An example of the floor mosaic (top-left), the control field (top-right), CMRF ^{PV3AR} synthesis, and the comparison with the CMRF ^{P3AR} model result.	49
5.6	An example of a the St. Vitus cathedral in Prague Castle stained glass window with some original panels replaced with our synthetic images.	50
5.7	Potts CMRF synthesis.	51
5.8	An example of a wooden floor BTF.	52
6.1	Example of breast segmentation. Left to right: original image, segmentation, extracted breast area.	54
6.2	Classifier training flowchart.	55
6.3	Visualisation of features from INbreast sample data. Features displayed for class combinations (rightwards, top to bottom) 1x4, 1x2, 1x3, 2x3, 2x4, 3x4 . .	56
6.4	Classification flowchart.	57
6.5	Example of pixel classification into different density classes.	58
6.6	Neighborhood of the 2DCAR model.	59
6.7	The overall best results found by the genetic algorithm during 1000 iterations.	59
6.8	The influence of the exponential forgetting factor on the classification result.	62
6.9	Example of extremal regions computed on breast image.	63
7.1	Single-view cancerous mammogram enhancement. Left to right: ground truth, prediction error based enhancement (Y_r^{enh}), probability based enhancement ($Y_r^{enh_2}$) and absolute prediction error based enhancement ($Y_r^{enh_3}$).	66
7.2	Single-view MLO mammogram enhancement using different functional neighbourhoods consecutively rightwards - 9, 5, and 3 pixel neighbourhood distance from the enhanced pixel (blue pixels - bottom row).	67
7.3	Single-view cancerous mammogram enhancement, ground truth and single rightwards model - upper row, single downward model and omnidirectional model combination - bottom.	68
7.4	Mammogram analysis - nonrigid approach.	69
7.5	Registered mammograms with visible reference points.	71
7.6	Mammogram with cancer in the right breast - original image with ground truth, CAR prediction error, CAR cross-prediction error	72
7.7	Mammogram from Fig. 7.6 - cross difference with highlighted cancer	73
7.8	Mammogram with cancer in the right breast - original image with ground truth, CAR prediction error, CAR cross-prediction error	74
7.9	Mammogram from Fig. 7.8 - cross difference with highlighted cancer	75

LIST OF FIGURES

7.10	Multiple-view medio-lateral mammogram enhancement consecutively rightwards - ground truth, pixel difference between registered LMLO and RMLO, cross-predicted gradient, and cross-prediction probability density. The upper row contains LMLO, bottom row RMLO.	76
7.11	The enhancement method's flowchart.	77
7.12	Enhanced mammogram example with a lesion and a big calcification.	81
7.13	Examples of mammogram enhancement.	82
7.14	Enhanced mammogram example with a dimly visible cancer.	83
7.15	Enhanced mammogram example with a several microcalcifications.	84
7.16	Enhanced benign mammogram example.	85
7.17	Example of the pseudocolour method compared with the unilateral result. Left to right: original with ground truth, enhancement by the unilateral method, enhancement based on prediction probabilities, enhancement based on prediction errors, and combined enhancement.	86
7.18	Screenshots of the radiologist validation program - test B.	88
8.1	Image degradations for the validation of contrast measures.	92
8.2	Contrast criteria behaviour for the averaging image degradation.	93
8.3	Contrast criteria behaviour for the Gaussian noise image degradation.	93
8.4	Contrast criteria behaviour for the uniform noise image degradation.	94
8.5	Contrast criteria behaviour for the range reduction image degradation.	94
8.6	Contrast criteria behaviour for the salt and pepper noise image degradation.	94
9.1	Example of our application for Potts hierarchical mimicking with one selected colour.	98
9.2	Example of our application for Potts mosaics.	99
9.3	Example of our application for mammogram analysis.	100
9.4	Class diagram of the mammogram databases.	100
9.5	Segmentation application example. Left: the application with training samples, right: the segmentation result.	101
9.6	Visualization of the feature space (left) and features for each pixel (right).	101
9.7	Sample code for digitized mammogram segmentation.	102
9.8	Sample code for our results management.	102
9.9	Results viewer application example.	103
9.10	Sample code for our arguments annotations.	104
9.11	Sample configuration of a console application.	104
9.12	Arguments helper application example.	105

List of Tables

2.1	Density and assessment categories.	17
3.1	Public Mammogram Databases: where (n_{mam}) is the number of mammograms, (n_{views}) number of views, (n_{gl}) number of grey levels in bits, and \downarrow is benign without callback.	29
4.1	Correlation between the β parameter and surrogate parameters for the Potts model.	33
4.2	Colour (Rot. Inv.) benchmark results for Spiral 3DCAR, Multidirectional 3DCAR, 3DCAR.	40
6.1	INbreast database classification results for all double-class combinations and the complete four BI-RADS tissue classes (rows \sim references, columns \sim interpretation).	60
6.2	MIAS database all dichotomous and one classification result for all three (fatty, fatty-glandular, dense-glandular) tissue classes (rows \sim references, columns \sim interpretation).	61
6.3	Best result's contingency table.	61
6.4	Contingency table of the Potts field Extremal regions based classification.	63
7.1	Enhancements' contrast comparison.	80
7.2	Tests A and B (radiologists 2 and 3 did not take test A, CS – correctly selected, TS – total selected, TPC – time per case).	87
7.3	Summary (TP - true positives, FP - false positives, FN - false negatives).	88
8.1	Summary of the behaviour of the different contrast measures among different degradations. \uparrow means monotonous increasing, \downarrow means monotonous decreasing and x means non-monotonous behaviour.	95
9.1	External libraries used in our project.	106

List of Algorithms

2.1	Swendsen-Wang algorithm pseudocode.	11
2.2	EM algorithm pseudocode.	13
5.1	Modified SW synthesis pseudocode.	44
*		

Abbreviations

Mathematical Notations

\mathbb{N}	Natural numbers set
\mathbb{R}	Real numbers set
\mathbf{b}	Vector \mathbf{b}
b_i	the i^{th} element of vector \mathbf{b}
$\ \mathbf{b}\ $	Norm of vector \mathbf{b}
$\dim \mathbf{b}$	Dimension of vector \mathbf{b}
\mathbf{A}	Matrix \mathbf{A}
$a_{i,j}$	Element of matrix \mathbf{A} at the i^{th} row, and the j^{th} column
\mathbf{A}^{-1}	Inverse matrix to matrix \mathbf{A}
\mathbf{A}^T	Transposed matrix to matrix \mathbf{A}
$\text{rank } \mathbf{A}$	Rank of matrix \mathbf{A} — how many independent rows/columns it has
$\max \{a, b\}$	Maximum of a and b , a when $a \geq b$, b when $a < b$
$\min \{a, b\}$	Minimum of a and b , a when $a \leq b$, b when $a > b$
$\mathcal{O}(x)$	The big \mathcal{O} notation
τ	Threshold
$\text{tr}(A)$	Trace of the given matrix A
$\text{card}(v)$	Cardinality of the given vector V
r	Multiindex with row and column components and possibly also spectral and/or directional indices

Acronyms

2DCAR	2D Simultaneous Causal Auto-Regressive Random Field
3DCAR	2D Simultaneous Causal Auto-Regressive Random Field
ACR	American college of radiology
AR	Auto-Regressive Random Field
BI-RADS	Breast Imaging-Reporting and Data System
BTF	Bidirectional Texture Function
CAD	Computer aided diagnosis
CAR	Simultaneous Causal Auto-Regressive Random Field
CC	Cranio caudal view
CIELAB	CIE color space LAB. . .
CMRF	Compound Markov Random Field
DAG	Directed acyclic graph
DDSM	Digital Database of Screening Mammography
DICOMS	Digital Imaging and Communications in Medicine, medical images standard
DOG	Difference of Gaussians
EM	Expectation Minimization algorithm
ER	Extremal region
FFT	Fast Fourier Transform
GMM	Gaussian Mixture Model
GMRF	Gaussian Markov Random Field
KL	Kullback-Leibler divergence
LCC	Cranio caudal view of the left breast
LMLO	Medio lateral oblique view of the left breast
MAP	Maximum a posteriori
MCMC	Markov Chain Monte-Carlo methods
MIAS	Mammographic Image Analysis Society database
MLO	Medio lateral oblique view
MRF	Markov Random Field
RCC	Cranio caudal view of the right breast
RMLO	Medio lateral oblique view of the right breast
ROI	Region of interest
SRC	Surrounding Region Contrast
SVM	Support Vector Machines
SW	Swendsen-Wang MCMC sampling method

Introduction

1.1 Motivation

1.1.1 Texture modeling

Texture is the notion commonly used to mathematically represent visual appearance of real world materials. Significant improvement in material or biological tissue recognition cannot be expected without sophisticated multidimensional descriptive data models and the corresponding contextual classifiers based on these models. Standard approaches use oversimplified discriminative data models and context-free classifiers. To overcome the limits of the common approach, we need to utilize complex multidimensional descriptive models which contain significantly larger amounts of information to describe intricate correlations present in visual data.

Unfortunately, these models have lots of unsolved theoretical issues such as parameter estimation, optimal contextual neighborhood selection, stability, efficient synthesis, etc., and usually require many compromising approximative solutions. Our aim is to add some new knowledge to these difficult classes of problems.

1.1.2 Mammography

Breast cancer is the most common type of cancer among middle-aged women in most developed countries [1, 2]. Almost one woman in ten develops a breast cancer in her life. To lower the mortality rate, women in the developed countries usually regularly attend a preventive mammography screening. However, around 25% of radiologically visible cancers are missed by the radiologists at screening [3]. This means that millions of cancer cases are missed and therefore even a slightest improvement in the detection methods could have a huge impact and save many lives.

One of the means of improving the cancer detection rate is computer aided detection (CAD). However, there is about 40% rate of false negatives reported by the currently used CADs. Automatic mammogram analysis is still difficult task due to wide variation of

breast anatomy, and ambiguous definitions of both visual and mathematical features of regions of interest (ROIs).

Specialists disagree on how much the CADs can influence the screening process - some argue the CAD systems could bring great improvement in the screening efficiency [4], others state that little relevant improvement has been proved when the radiologist had the assistance of a CAD system [3, 5]. The truth is probably in the middle since the impact of CADs on diagnosis depends a lot on the radiologist's use of the CAD system. According to [6], however, there is a potential of lowering the radiologist's false negative rate by as much as 70%.

The biggest problem with current CAD systems is their large false negative rate and an even larger false positive rate. Most CAD systems point out 2-3 regions of interest (ROIs) per mammogram on average. Taking into account that there are about 8 malignant mammograms in 1000 [3], the radiologists consider the current CAD systems as misleading, which proves the need for a better new system with lower false positive and false negative rates.

1.1.3 Contrast

Image enhancement methods aim to improve human image interpretation accuracy by increasing visual distinguishability of single objects recorded in a visual scene. This requires an increase in image contrast which is the relative difference in luminance or colour between multiple objects. A typical important application for image enhancement is preventive mammography screening. In such important image enhancement applications even a slightest improvement in the detection methods could have a huge impact and save many lives. A reliable quality contrast criterion is then the prerequisite for any monitoring of an image enhancement method development progress or for ranking existing methods.

1.2 Problem Statement

This thesis aims to develop novel descriptive multidimensional Markovian textural models and improve computer aided diagnosis in the field of X-ray mammography using these nontrivial models.

These general mathematical models, applicable in wide areas of texture modeling outside X-ray mammography as well, allow ideal visual verification using synthesis of the corresponding measured data spaces, contrary to standard discriminative models. The integral part of the thesis is extensive benchmarking of achieved results.

Computer aided detection of mammographic regions of interest (ROIs - microcalcifications, developing cancers, abnormalities) is a nontrivial task of pattern recognition with hard to define indistinct definition of what a ROI might be. We also have to bear in mind that the final goal is not the replacement of diagnosticians, but rather a help for them to make their work easier. Therefore we do not focus in this work on ROI segmentation, but

instead on accentuation of regions which do not fit into the particular part of the breast according to our models and bilateral mammogram comparison.

The focus of our study is mammogram texture and the following search for its optimal mathematical representation.

1.3 Goals of the Dissertation Thesis

1. Descriptive multidimensional texture models development for texture analysis and synthesis applications
2. X-ray mammograms tissue analysis based on the descriptive multidimensional texture models
3. Development of methods for mammogram parenchymal patterns enhancement
4. Development and verification of image enhancement criteria

1.4 Structure of the Dissertation Thesis

The thesis is organized into ten chapters as follows:

1. *Introduction*: Describes the motivation behind our efforts together with our goals. There is also a list of contributions of this dissertation thesis.
2. *Background and State-of-the-Art*: Introduces the reader to the necessary theoretical background and surveys the current state-of-the-art.
3. *Experimental Data*: Covers the data we used for experiments to verify our approach.
4. *Texture Models*: Presents our work in the field of texture models.
5. *Texture Synthesis*: Shows our developed methods in the field of homogeneous texture synthesis.
6. *Breast Tissue Density Classification*: Provides the description and results of our approach to the problem of mammogram tissue density classification.
7. *Mammogram Texture Enhancement*: Demonstrates our usage of descriptive textural models for the enhancement of abnormalities in X-ray mammograms.
8. *Local Contrast Criteria*: Presents the comparison of methods for computing image contrast along with our proposed surrounding region contrast method.
9. *Developed Software*: Contains a short overview of the software we developed and used for the experiments during our research.

1. INTRODUCTION

10. *Conclusions*: Summarizes the results of our research, suggests possible topics for further research, and concludes the dissertation thesis.

Background and State-of-the-Art

In this chapter we first present the theoretical background in Sec. 2.1. We focus mostly on the description of texture representation (Sec. 2.1.1) we based our work on. Then follow the sections on Gaussian mixtures (Sec. 2.1.2) and Extremal regions (Sec. 2.1.3). The last section of the theoretical background covers some basic information on mammography (Sec. 2.1.4).

The second section (Sec. 2.2) then covers the work which has been previously done by other researchers in the area of breast segmentation (Sec. 2.2.1), texture analysis (Sec. 2.2.3), breast density classification (Sec. 2.2.4), texture enhancement (Sec. 2.2.5), breast registration (Secs. 2.2.6 and 2.2.7), contrast measures (Sec. 2.2.8) and texture synthesis (Sec. 2.2.9).

2.1 Theoretical Background

2.1.1 Texture Representation

There is no rigorous mathematical definition [7] of texture but this notion is commonly used to represent the visual appearance of real world materials. We are interested in mathematical descriptive texture representations which can be beneficial for both analytical representation as well as physically correct texture visualization. Currently, the best mathematical textural models are based on multidimensional Markov random fields which can built upon from several simpler lower dimensional random field models.

2.1.1.1 2DCAR Texture Model

Definition The 2DCAR [8] random field is a Markovian family (wide-sense Markov) of random variables with a joint probability density on the set of all possible realizations Y

of the $M \times N$ lattice I , subject to the following condition:

$$p(Y | \gamma, \sigma^{-2}) = (2\pi\sigma^2)^{-\frac{(MN-1)}{2}} \exp \left\{ \frac{-1}{2} \text{tr} \left\{ \sigma^{-2} \begin{pmatrix} -\alpha \\ \gamma^T \end{pmatrix}^T \tilde{V}_{MN-1} \begin{pmatrix} -\alpha \\ \gamma^T \end{pmatrix} \right\} \right\}, \quad (2.1)$$

where α is a unit vector, $\text{tr}()$ is a trace of the corresponding matrix, and the following notation is used

$$\tilde{V}_{r-1} = \sum_{k=1}^{r-1} \begin{pmatrix} Y_k Y_k^T & Y_k X_k^T \\ X_k Y_k^T & X_k X_k^T \end{pmatrix} = \begin{pmatrix} \tilde{V}_{y(r-1)} & \tilde{V}_{xy(r-1)}^T \\ \tilde{V}_{xy(r-1)} & \tilde{V}_{x(r-1)} \end{pmatrix}.$$

Here, $r = [r_1, r_2]$ is spatial index denoting history of movements on the lattice I .

The 2DCAR model can be expressed as a stationary causal uncorrelated noise-driven 2D autoregressive process:

$$Y_r = \gamma X_r + e_r, \quad (2.2)$$

where $\gamma = [a_1, \dots, a_\eta]$ is the parameter vector, $\eta = \text{cardinality}(I_r^c)$, I_r^c denotes a causal (or alternatively unilateral) contextual neighbourhood (i.e., all support pixels were previously visited and they are known). Furthermore, e_r denotes white Gaussian noise with zero mean and a constant but unknown variance σ^2 , and X_r is a support vector of Y_{r-s} where $s \in I_r^c$.

Our implementations use a locally adaptive version of this 2DCAR model [9], where its recursive statistics are modified by an exponential forgetting factor, i.e., a constant smaller than 1 which is used to weight the older data.

The posterior probability density [9] of the model is:

$$p(Y_r | Y^{(r-1)}, \hat{\gamma}_{r-1}) = \frac{\Gamma(\frac{\beta(r)-\eta+3}{2})}{\Gamma(\frac{\beta(r)-\eta+2}{2}) \pi^{\frac{1}{2}} (1 + X_r^T V_{x(r-1)}^{-1} X_r)^{\frac{1}{2}} |\lambda_{(r-1)}|^{\frac{1}{2}}} \left(1 + \frac{(Y_r - \hat{\gamma}_{r-1} X_r)^T \lambda_{(r-1)}^{-1} (Y_r - \hat{\gamma}_{r-1} X_r)}{1 + X_r^T V_{x(r-1)}^{-1} X_r} \right)^{-\frac{\beta(r)-\eta+3}{2}} \quad (2.3)$$

And the conditional mean value predictor of the one-step-ahead predictive posterior density (2.3) for the normal-gamma parameter prior is

$$E \{Y_r | Y^{(r-1)}\} = \hat{\gamma}_{r-1} X_r. \quad (2.4)$$

Parameter Estimation Parameter estimation of a 2DCAR model using either the maximum likelihood, or the least square or Bayesian methods can be found analytically.

The Bayesian parameter estimates of the 2DCAR model using the normal-gamma parameter prior are:

$$\hat{\gamma}_{r-1}^T = V_{x(r-1)}^{-1} V_{xy(r-1)} \quad (2.5)$$

$$\hat{\sigma}_{r-1}^2 = \frac{\lambda_{(r-1)}}{\beta(r)} \quad (2.6)$$

where

$$\begin{aligned} \lambda_{(r-1)} &= V_{y(r-1)} - V_{xy(r-1)}^T V_{x(r-1)}^{-1} V_{xy(r-1)} , \\ V_{(r-1)} &= \tilde{V}_{(r-1)} + V_{(0)} , \\ \beta(r) &= \beta(0) + r - 1 , \end{aligned}$$

and $\beta(0)$ is an initialization constant and submatrices in $V_{(0)}$ are from the parameter prior. The estimates (2.5), (2.9) can also be evaluated recursively ([9]).

2.1.1.2 3DCAR Texture Model

Definition The causal autoregressive random field (3D CAR) model [10] is a family of random variables with a joint probability density on the set of all possible realizations Y of the $M \times N \times d$ lattice I , subject to the following condition:

$$p(Y | \gamma, \Sigma^{-1}) = \frac{|\Sigma^{-1}|^{\frac{(MN-1)}{2}}}{(2\pi)^{\frac{d(MN-1)}{2}}} \exp \left\{ -\frac{1}{2} \text{tr} \left\{ \Sigma^{-1} \begin{pmatrix} -I \\ \gamma^T \end{pmatrix}^T \tilde{V}_{MN-1} \begin{pmatrix} -I \\ \gamma^T \end{pmatrix} \right\} \right\} ,$$

where the following notation is used

$$\begin{aligned} \tilde{V}_{r-1} &= \begin{pmatrix} \tilde{V}_{yy(r-1)} & \tilde{V}_{xy(r-1)}^T \\ \tilde{V}_{xy(r-1)} & \tilde{V}_{xx(r-1)} \end{pmatrix} , \\ \tilde{V}_{yy(r-1)} &= \sum_{k=1}^{r-1} Y_k Y_k^T , \\ \tilde{V}_{xy(r-1)} &= \sum_{k=1}^{r-1} X_k Y_k^T , \\ \tilde{V}_{xx(r-1)} &= \sum_{k=1}^{r-1} X_k X_k^T . \end{aligned}$$

The 3D CAR model can be expressed as a stationary causal uncorrelated noise driven 3D autoregressive process:

$$Y_r = \gamma X_r + e_r , \quad (2.7)$$

2. BACKGROUND AND STATE-OF-THE-ART

where γ is the $d \times d\eta$ parameter matrix $\gamma = [A_1, \dots, A_\eta]$, $\eta = \text{card}(I_r^c)$, I_r^c is a causal neighbourhood, e_r is a Gaussian white noise vector with zero mean and a constant but unknown covariance matrix Σ (estimated by (2.10)) and X_r is a corresponding vector of Y_{r-s} (design vector).

Parameter Estimation The selection of an appropriate CAR model support is important to obtain good results in modeling of a given random field. If the contextual neighbourhood is too small it cannot capture all details of the random field. Inclusion of the unnecessary neighbours on the other hand add to the computational burden and can potentially degrade the performance of the model as an additional source of noise. The optimal Bayesian decision rule for minimizing the average probability of decision error chooses the maximum posterior probability model, i.e., a model M_i corresponding to $\max_j \{p(M_j | Y^{(r-1)})\}$ where $Y^{(r-1)}$ denotes the known process history $Y^{(r-1)} = \{Y_{r-1}, Y_{r-2}, \dots, Y_1\}$. The most probable CAR model given past data $Y^{(r-1)}$, the normal-Wishart parameter prior and the uniform model prior is the model M_i for which $i = \arg \max_j \{D_{j(r-1)}\}$

$$D_{j(r-1)} = \frac{d^2\eta}{2} \ln \pi \sum_{i=1}^d \left[\ln \Gamma\left(\frac{\beta(r) - d\eta + d + 2 - i}{2}\right) - \ln \Gamma\left(\frac{\beta(0) - d\eta + d + 2 - i}{2}\right) \right] - \frac{d}{2} \ln |V_{xx(r-1)}| - \frac{\beta(r) - d\eta + d + 1}{2} \ln |\lambda_{(r-1)}|$$

where $\beta(r) = \beta(0) + r - 1$, $\beta(0) > 1$, and

$$\lambda_{(r)} = V_{yy(r)} - V_{xy(r)}^T V_{xx(r)}^{-1} V_{xy(r)} \quad (2.8)$$

Parameter estimation of a CAR model using the maximum likelihood, the least square or Bayesian methods can be found analytically. The Bayesian parameter estimations of the causal AR model with the normal-Wishart parameter prior which maximize the posterior density are:

$$\hat{\gamma}_{r-1}^T = V_{xx(r-1)}^{-1} V_{xy(r-1)} \quad (2.9)$$

and

$$\hat{\Sigma}_{r-1} = \frac{\lambda_{(r-1)}}{\beta(r)}, \quad (2.10)$$

where $V_{uz(r-1)} = \tilde{V}_{uz(r-1)} + V_{uz(0)}$ and matrices $V_{uz(0)}$ are the corresponding matrices from the normal-Wishart parameter prior. The estimates (2.8), (2.9) and (2.10) can be also evaluated recursively if necessary.

2.1.1.3 Potts MRF

Definition The Potts model [11, 12] is a generalization of the 2-state Ising model [13, 14] to n -states, where $n \in \mathbb{N}$. It is one of the simplest MRFs which was first designed for physical simulations of grain growth in metals or coarsening of foams. But it also has a variety of possible uses in image processing and its main advantage is that it is analytically solvable. In image processing, it can be used for texture synthesis, segmentation, noise reduction, etc.

The Potts model is a model of interacting spins on a lattice (same as the Ising model), but whereas the Ising model allowed only two possible states for a node on the lattice, the Potts model allows it to be in one of general n possible states - $s_i \in \{1..n\}$.

The general Potts model is defined by the following equation:

$$\beta H = -\beta \sum_{(i,j)} J_{ij} \delta(s_i, s_j) - \sum_i h_i s_i \quad ,$$

where δ is the Kronecker delta, J_{ij} is 1 iff i and j are neighbors, otherwise 0 and H (the Hamiltonian of the system) is the energy of the system as in the Gibbs distribution:

$$P(X|\beta) = \frac{1}{Z(\beta)} e^{-\beta(\sum_{(i,j)} J_{ij} \delta(s_i, s_j) - \sum_i h_i s_i)} \quad . \quad (2.11)$$

For our purpose of texture synthesis, we can omit the external magnetic field part:

$$H = \sum_{(i,j)} J_{ij} \delta(s_i, s_j)$$

This way the parameter β can be effectively estimated by the pseudo-likelihood method, as described in [15, 16]. We will cover this further in this section.

Parameter Estimation Potts model has the advantage that only one parameter needs to be estimated - β . The estimation using maximum pseudo-likelihood method was described in [15] and is done as follows.

The local density function for each point in the image lattice can be computed as

$$p(s_i = q | s_{\eta_i}, \beta) = \frac{e^{\beta U_{s_i}(q)}}{\sum_{l=1}^M e^{\beta U_{s_i}(l)}} \quad ,$$

where $U_{s_i}(q)$ denotes the number of neighbours of node s_i that are in state q .

Assuming conditional independence of the points in the lattice, we get the pseudo-likelihood function:

$$PL(\beta) = \prod_{s_i \in S} p(s_i = q | s_{\eta_i}, \beta) \quad .$$

When we make a logarithm of the pseudo-likelihood function, differentiate it by β and require the result to equal zero, we get the following equation whose solution is the desired

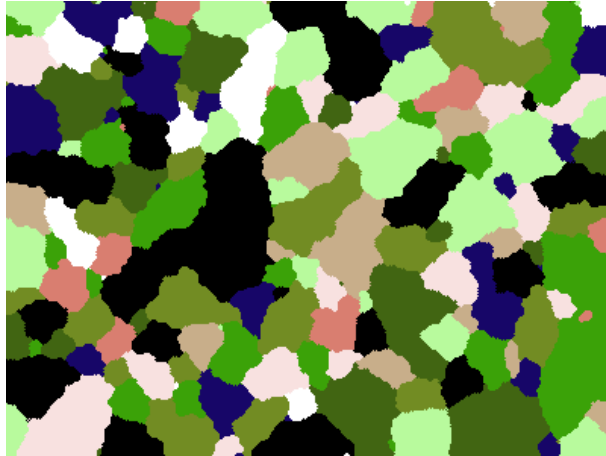


Figure 2.1: Example of a sampled Potts model with 10 colours.

β with maximal pseudo-likelihood. The solution is easy to compute numerically for most given lattices.

$$\Psi(\beta) = \sum_{s_i \in S} U_{s_i}(q) - \sum_{s_i \in S} \frac{\sum_{l=1}^M U_{s_i}(l) e^{\beta U_{s_i}(l)}}{\sum_{l=1}^M e^{\beta U_{s_i}(l)}} = 0 .$$

Sampling The Potts model can be sampled using standard MCMC approaches for realizing MRF such as the Gibbs sampler or Metropolis algorithm [17]. For the Potts model also exist specialized fast samplers: the Wolf’s algorithm [18] and the Swendsen-Wang algorithm [19] that we have chosen.

The advantage of the Swendsen-Wang (SW) algorithm is that it converges very fast. Furthermore, the changes made to the sampled system are substantial - in each step, the system can change into any other state of the state-space, which is suitable for our further use.

The SW algorithm is based on the idea of extending the Potts field with a graph whose vertices correspond with the nodes of the Potts field and edges represent a bond between the nodes. It is a MCMC method without a specified ending. Fig. 2.2 shows a sample step of the SW algorithm, which is described in Alg. 2.1.

2.1.1.4 BTF

The Bidirectional Texture Function (BTF) [20] is currently the most precise approximation of the physically correct texture representation, e.g. with applications is 3D graphics texture rendering, that we are able to measure. Multispectral BTF is a seven-dimensional function which considers measurement dependency on color spectrum, planar material position and its dependence on illumination and viewing angles:

$$BTF(r, \theta_i, \phi_i, \theta_v, \phi_v) ,$$

Algorithm 2.1 Swendsen-Wang algorithm pseudocode.

Input: β , lattice I , neighborhood I_N

```

loop
  for all  $v \in I$  do
    for all  $u \in I_N(v)$  do
      Form an edge between  $u$  and  $v$  with probability  $p = 1 - e^{-\beta}$ 
    end for
  end for
  for all connected component  $C \subset I$  do
     $col = randomColor$ 
    for all  $v \in C$  do
       $v \leftarrow col$ 
    end for
  end for
end loop

```

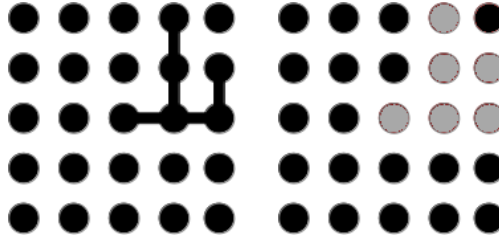


Figure 2.2: Swendsen-Wang algorithm step.

where the multiindex $r = [r_1, r_2, r_3]$ denotes the planar horizontal and vertical position (r_1 and r_2 respectively), r_3 is the spectral index, θ, ϕ are respectively the elevation and azimuthal angles of the illumination (θ_i, ϕ_i) and view direction vector (θ_v, ϕ_v) . Fig. 2.3 shows an illustration of the BTF's variables.

2.1.2 Gaussian Mixtures

Gaussian mixture model (GMM) is a probability distribution (2.13) consisting of a weighed sum of N Gaussian distribution components (2.12), such that the sum of the weights equals 1 (2.14). We use this model to represent feature space distribution in our developed classification methods.

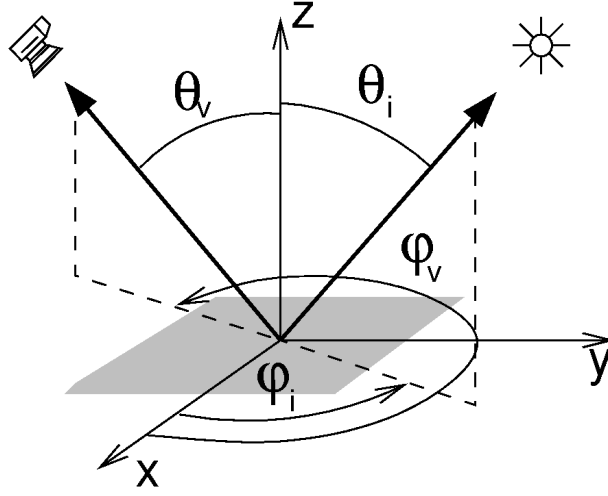


Figure 2.3: Explanation of the BTF space measurements.

$$\mathcal{N}(\theta|\mu, \Sigma) = \frac{1}{\sqrt{(2\pi)^N |\Sigma|}} e^{(-\frac{1}{2}(\theta-\mu)^T \Sigma^{-1} (\theta-\mu))} \quad (2.12)$$

$$f(\theta|\mu_k, \Sigma_k, w_k, k \in \{1 \dots N\}) = \sum_{k=1}^N w_k \mathcal{N}(\theta|\mu_k, \Sigma_k) , \quad (2.13)$$

$$\sum_{k=1}^N w_k = 1 \quad (2.14)$$

2.1.2.1 EM Algorithm

The EM algorithm [21, 22] is an iterative algorithm that can be used to estimate the parameters of a GMM from the given random samples. Let Θ be the set of observations θ , τ be the threshold of relative improvement between steps, T be the maximum number of steps. Then, iteratively, the estimated parameters w_k, μ_k, Σ_k can be found as:

2.1.2.2 Kullback-Leibler Divergence

Kullback-Leibler divergence (KL divergence) [23] is a measure of how much one probability distribution diverges from another (it is not symmetrical). It is defined as:

$$D(f(x)||g(x)) \stackrel{def}{=} \int f(x) \log \frac{f(x)}{g(x)} dx .$$

For the Gaussian distribution, the KL divergence can be solved analytically:

$$D(f(x)||g(x)) = \frac{1}{2} \left(\log \frac{|\Sigma_g|}{|\Sigma_f|} + tr(\Sigma_g^{-1} \Sigma_f) - d + (\mu_f - \mu_g)^T \Sigma_g^{-1} (\mu_f - \mu_g) \right) .$$

Algorithm 2.2 EM algorithm pseudocode.

Input: Set of random samples Θ **repeat**

$$\begin{aligned}
 q^t(k|\theta) &\leftarrow \frac{w_k^t \mathcal{N}(\theta|\mu_k^t, \Sigma_k^t)}{\sum_i^N w_i^t \mathcal{N}(\theta|\mu_i^t, \Sigma_i^t)} \\
 w_k^{t+1} &\leftarrow \frac{1}{|\Theta|} \sum_{\theta \in \Theta} q^t(k|\theta) \\
 \mu_k^{t+1} &\leftarrow \frac{1}{\sum_{\theta \in \Theta} q^t(k|\theta)} \sum_{\theta \in \Theta} \theta q^t(k|\theta) \\
 \Sigma_k^{t+1} &\leftarrow \frac{1}{\sum_{\theta \in \Theta} q^t(k|\theta)} \sum_{\theta \in \Theta} q^t(k|\theta) (\theta - \mu_k^{t+1})(\theta - \mu_k^{t+1})^T \\
 L^{t+1}(\Theta) &\leftarrow \sum_{\theta \in \Theta} \log f(\theta|\mu_k^{t+1}, \Sigma_k^{t+1}, w_k^{t+1}, k \in \{1 \dots N\}) \\
 t &\leftarrow t + 1
 \end{aligned}$$

until $\frac{L^{t+1}-L^t}{L^{t+1}} < \tau \vee t \geq T$ **for all** $k \in \{1 \dots N\}$ **do**

$$\begin{aligned}
 \mu_k &\leftarrow \mu_k^t \\
 \Sigma_k &\leftarrow \Sigma_k^t \\
 w_k &\leftarrow w_k^t
 \end{aligned}$$

end for**Output:** Estimated sets of μ_k , Σ_k and w_k

However, for the GMM, the KL divergence is not analytically solvable. Therefore, we use the following approximation [24]:

$$D_v(f(x)||g(x)) \simeq \sum_{i=1}^M w_{f,i} \log \frac{\sum_{i'} w_{f,i'} e^{-D(f_i||f_{i'})}}{\sum_j w_{g,j} e^{-D(f_i||g_j)}} ,$$

where $D(f_i||f_{i'})$ and $D(f_i||g_j)$ denote the KL divergences of the components of the GMM and $w_{f,i}$ and $w_{g,j}$ are their corresponding weights.

2.1.3 Extremal Regions

The Extremal Regions (ER) [25, 26] are a fast ($\mathcal{O}(n \log \log n)$) method of getting all thresholds (or rather a threshold tree) of an image with respect to one colour channel.

Let I be a rectangular lattice, $r = [r_1, r_2] \in I$ be a pixel location and $Y_r \in S$ be the value of pixel r in image channel Y , where S is the set of all possible values of Y_r ,

typically $S = \{0, \dots, 255\}$, but any totally ordered set can be used. Let $\mathcal{A} \subset I \times I$ be the neighbourhood adjacency relation.

Region \mathcal{R} of an image Y is a continuous subset of I , i.e. $\forall r, s \in \mathcal{R}, \exists t_1, \dots, t_n : r \mathcal{A} t_1 \mathcal{A} \dots \mathcal{A} t_n \mathcal{A} s$.

Outer region boundary $\delta\mathcal{R}$ is the set of pixels which are adjacent to region \mathcal{R} but do not belong to it: $\delta\mathcal{R} = \{s \in I \setminus \mathcal{R} : \exists r \in \mathcal{R} : r \mathcal{A} s\}$.

Extremal region is a region whose pixels' values are strictly lower than those of its outer boundary: $\forall r \in \mathcal{R}, s \in \delta\mathcal{R} : Y_r < Y_s$. An ER at threshold τ (\mathcal{R}_τ) is a union of a set of ERs at threshold $\tau' < \tau$ and pixels of value τ which are on their boundaries or connect them: $\mathcal{R}_\tau = (\bigcup R_{\tau'}, \forall \tau' < \tau) \cup (\bigcup s \in I : Y_s = \tau)$. This induces an inclusion relation on the Extremal Regions where each region can have any number of predecessors and exactly one successor. The only exception is the ultimate successor $\mathcal{R}_{\tau_{max}}$, where $\tau_{max} = \max_r Y_r$, which has no successor and, transitively through its predecessors, contains all pixels in the image.

2.1.4 Mammography

In this section we briefly describe the mammographical terminology we are going to use in the rest of this work.

Cranio-caudal view (CC) is the top-down view of the breast. The CC views of the left and right breasts are denoted LCC and RCC respectively. An example is shown in Fig. 2.4 on the left.

Medio-lateral oblique view (MLO) is the side oblique view of the breast. The MLO views of the left and right breasts are denoted LMLO and RMLO respectively. An example is shown in Fig. 2.4 on the right.

Microcalcifications are tiny grains of calcium deposits, that can be scattered throughout the mammary gland. They are perfectly normal, but under certain circumstances can also be the sign of a developing cancer. In the mammograms they look like tiny little white dots. A sample image displaying microcalcifications is in Fig. 2.5 on the left.

Lymphatic nodes Lymphatic nodes, like the microcalcifications are a normal benign parts of breast, but their increased presence can be the sign of malignant changes in the breast. In the mammograms they look like small circular lighter shades. An example of lymphatic nodes can be seen in Fig. 2.5 on the right.

Asymmetries Asymmetries between the left and right breast are a always warning element. Quite often they are the sign of a developing cancer which is the reason that radiologists compare the images of the left and right breast together and look for differences between them. An example can be seen in Fig. 2.6 on the left and in the middle.

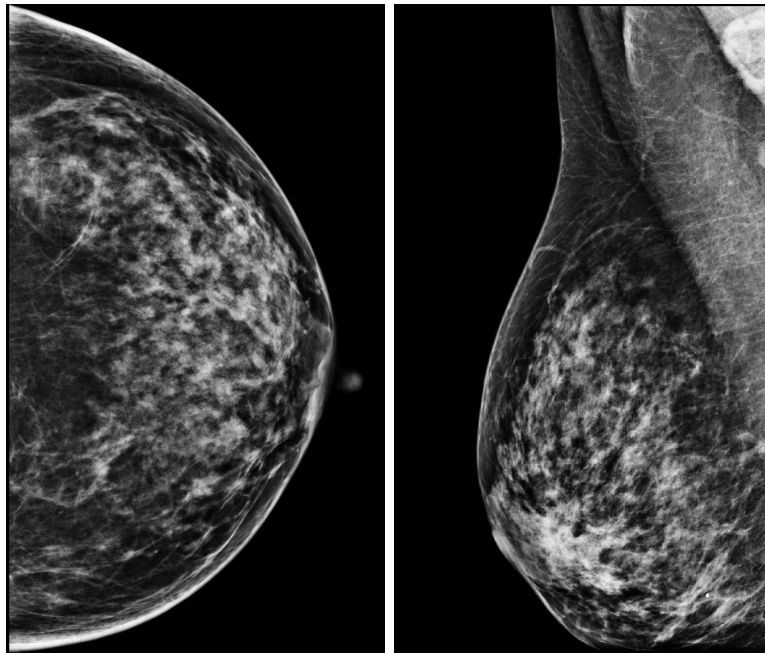


Figure 2.4: Example of a cranio-caudal view (left) and a medio-lateral oblique view (right) of a mammogram.

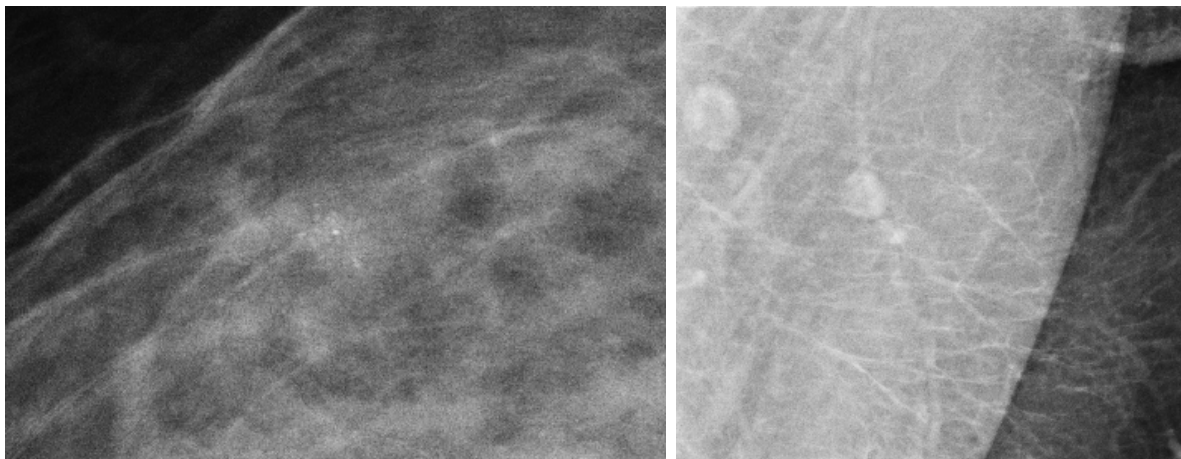


Figure 2.5: Example of clustered microcalcifications scattered inside a tiny cancer in the center of the image (left) and several lymphatic nodes inside the pectoral muscle (right).



Figure 2.6: Example of an asymmetry between the left and right breasts (left and middle). Image shown on the right displays an example of a mass.

Masses Masses are what radiologists are usually looking for in the mammograms. They are brighter areas in the mammogram which could be both benign and malignant. They can be caused by several different things - cysts (non-cancerous, fluid filled sacs), non-cancerous solid tumours (such as fibroadenomas) or they can be cancerous regions. Fig. 2.6 on the right shows an example of a CC mammogram with a mass.

2.1.4.1 ACR BI-RADS Standard

American College of Radiology (ACR) Breast Imaging Reporting and Data System (BI-RADS) [27] specifies a guidance system for mammogram reporting. From this system, we are interested in the classification of breast composition and the assessment of the risk of cancer (a short overview can be found in Tab. 2.1).

Breast composition is classified into the following 4 groups (example images can be seen in Fig. 2.7):

BI-RADS a The breast is almost entirely fat, fibrous and glandular tissue makes up less than 25% of the breast.

BI-RADS b There are scattered areas of fibroglandular density. Fibrous and glandular tissue makes up from 25 to 50% of the breast.

BI-RADS c The breast tissue is heterogeneously dense and the breast has more areas of fibrous and glandular tissue (from 51 to 75%) that are found throughout the breast. This can make it hard to see small masses (cysts or tumours).

BI-RADS d The breast tissue is extremely dense. The breast is made up of more than 75% fibrous and glandular tissue. This can lead to missing some cancers.

Composition	Tissue density description	Assessment	Assessment description
-	unspecified	BI-RADS 0	incomplete
BI-RADS a	entirely fatty	BI-RADS 1	normal
BI-RADS b	scattered fibroglandular d.	BI-RADS 2	benign
BI-RADS c	heterogeneously d.	BI-RADS 3	probably benign
BI-RADS d	extremely d.	BI-RADS 4	suspicious
		BI-RADS 5	highly suggestive of malignancy
		BI-RADS 6	biopsy-proven malignancy

Table 2.1: Density and assessment categories.

There are 6 assessment categories according to the ACR BI-RADS system:

BI-RADS 0 Incomplete, needs additional imaging evaluation and/or prior mammograms for comparison

BI-RADS 1 Negative. Describes a normal examination with nothing to comment on.

BI-RADS 2 Benign. There is a benign finding in the mammogram, be it calcified fibroadenomas, skin calcifications, fat-containing lesions, etc.

BI-RADS 3 Probably benign. Should have a $\leq 2\%$ probability of malignancy and is not expected to change over the suggested period of imaging surveillance.

BI-RADS 4 Suspicious. The finding does not have a classic appearance of malignancy but is suspicious enough to justify a recommendation for biopsy. This category is split into three subcategories, 4a, 4b, 4c - low suspicion, moderate suspicion and high suspicion respectively.

BI-RADS 5 Highly suggestive of malignancy. The probability of malignancy should be $\geq 95\%$.

BI-RADS 6 Biopsy-proven malignancy.

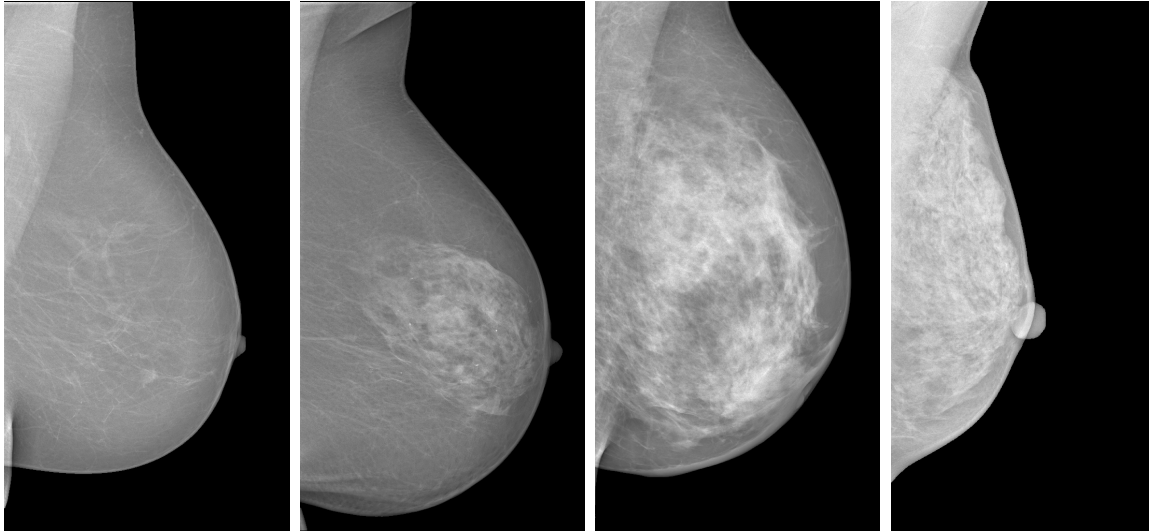


Figure 2.7: Example mammograms with different density values - left to right consequently contain BI-RADS densities 1, 2, 3 and 4.

2.2 Previous Results and Related Work

Automatic analysis of mammograms is a wide field of study with several sub-problems to be solved. Single view analysis methods focus on segmenting the breast area, finding clustered microcalcifications, segmentation of lesions, etc. Multiple view analysis then focuses on registration of both bilateral and temporal mammograms and their comparison, fusion of data acquired from CC and MLO views and fusing multi-modal mammography information such as sonography or magnetic resonance.

2.2.1 Breast Segmentation

The complexity of breast area segmentation differs greatly based on whether the segmentation is performed on scans of analogue mammograms or on digitally acquired mammograms.

The basic approach would be simple thresholding and its variations such as e.g. in [28] where the authors compute an adaptive threshold for each row separately.

In [29], the described method classifies pixels into homogeneous, edge, raster and aquarelle classes and based on the found classes then finds the breast region.

2.2.2 Microcalcification Segmentation

Microcalcifications play an important role in mammography analysis because they can indicate a developing cancer in the otherwise undetectable very early stages.

In [30] a gradient based method is proposed which uses contrast enhancement and thresholding to 30% brightest pixels in the image.

In [31] the difference of the input image and an image created by blurring it using Gaussian blur is used for locating microcalcifications.

2.2.3 Breast Texture Analysis

While unsupervised methods are used for breast area and microcalcification segmentation, in segmentation focused on identifying lesions we encounter both the supervised and unsupervised approach.

In [32, 33] unsupervised methods for texture segmentation are applied to detecting mammographical ROIs. The methods are based on using 3D CAR models, segmentation is done in parameter space based on Gaussian mixture model solved by the EM algorithm.

The method described in [34] uses a Gaussian mixture based approach to construct a likelihood image which shows the measure of abnormality of the particular parts of the image.

There is an interesting approach shown in [35] for segmenting the breast into texture types called Tabár building blocks, inspired by [36] - nodular, linear, homogeneous, radiolucent, creating probability maps for further processing.

In [37] we can see a method which finds a lesion around a given seed. It uses the assumption that most lesions are of a circular character and works in polar coordinate system. It then uses dynamic programming to find the least energetically demanding path from the $-\pi$ to $+\pi$ angles.

The paper [38] describes another seed based method which is based on region growing according to the gradient information.

2.2.4 Breast Density Analysis

Muhimmah and Zwiggelaar [39] use multiresolution histogram features-based method computed on Gaussian pyramid with the Directed Acyclic Graph - Support Vector Machine (DAG-SVM) classifier.

Mustra et al. [40] extract multiple features using gray level co-occurrence matrices and histogram based approaches and classify the density using the kNN classifier.

2.2.5 Texture Enhancement

The mammogram enhancement methods can be roughly categorized into frequency and spatial based methods. The frequency based methods [41, 42, 43, 44] use mostly some wavelet multiscale decomposition with modified wavelet coefficients to enhance mammogram contrast. The spatial methods [45, 46] use some nonlinear or adaptive linear filters.

We have implemented four representative mammogram enhancement methods from several published alternatives [42, 43, 46, 47, 48, 49, 50, 51] to compare with our adaptive probabilistic mammogram enhancement methods.

2.2.5.1 Histogram Equalization

The well known grayscale image enhancement technique is histogram equalization [52], which is based on the idea of forcing the enhanced image histogram to be uniform. This is a popular technique for contrast enhancement because of its simplicity and time efficiency. However, it may overenhance the noise and sharp regions in the original images.

2.2.5.2 Matting-Based Enhancement

The enhancement method based on the idea of image matting was published in [53]. The method sees the mammographic images (Y) as a superposition of adipose tissue (B), which forms most in the background of the image, and the mammary glands and other breast structures that the radiologists need to focus on, denoted by (G):

$$Y = Gc + B(1 - c) \quad (2.15)$$

The enhancement method then selectively subtracts the background tissues from the superposition, thus creating the enhanced image.

To enable this, the authors had to estimate the background (B) and the opacity alpha value for each pixel by which it is blended with the rest of the image (c). In this method the background is set as a constant value for the whole image represented by the 85% percentile of grey values of the breast part of the image.

2.2.5.3 Nonlinear Unsharp Masking

A nonlinear unsharp masking (NLUM) combined with nonlinear filtering for mammogram enhancement was introduced in [54]. The method embeds different types of filters into the nonlinear filtering operator within the 3×3 window which fuses the enhanced and original mammogram data.

High-frequencies of the signal are emphasized by either subtracting a low-pass filtered signal from its original or adding a scaled high-frequency factor to the measured original. The method's eight parameters are optimized with relation to a proposed second-derivative-like measure of enhancement (SDME) [54].

2.2.5.4 Direct Contrast Enhancement

Tang et al. [41] developed an enhancement method based on wavelet transformation. It transforms the mammogram image into a multi-level 2D wavelet space. Directional contrast at each level of the wavelet transformation is estimated; namely, the three high-pass components are divided, each by its low-pass component. The contrast estimate is then multiplied by a constant contrast enhancement factor λ . The enhanced image is acquired by running the inverse wavelet transform one level at a time. To make up for the contrast enhancement changes, the high-pass components are re-multiplied by the newly computed low-pass component in each iteration until the whole inverse is achieved.

This also allows the method to enhance the image's contrast without introducing excessive additional noise.

2.2.5.5 Non-linear Polynomial Filters

Bhateja et al. [55] have published an enhancement method based on the Non-linear polynomial filtering framework based on quadratic Volterra filters for contrast and edge enhancement of mammographic images. The method performs both low-pass and high-pass filtering of the image and combines the output in one contrast and edge enhanced result.

2.2.6 CC - MLO Pseudoregistration

To decrease false positive rate in detecting mammogram abnormalities or to enhance the belief in the finding, radiologists try to find corresponding areas in CC and MLO views of the same breast. As bright areas in the mammogram can be also formed by superposition of normal tissue along the line of the X-ray, this approach can help distinguish between the superposition and a possible abnormality.

Cranio-caudal to medio-lateral oblique view data fusion usually uses the nipple as a reference point [56] and creates a coordinate system based on the distance of a point to the chest and the coordinate in the axes of the CC and MLO views almost precisely copy the new 3D coordinates introduced.

In [57] a complex approach is proposed which detects stellated patterns, finds nodular areas using radial gradient vectors and tries to find a corresponding structure in the other view as well. The scan is done in equidistance to the nipple with search width extent given as an empirically obtained parameter. This method is supervised, based on neural networks.

The method described in [58] tries to reconstruct a 3D model of the breast and display microcalcifications segmented and registered from both CC and MLO views. Coordinate system is based on the distance to the nipple and direction parallel and perpendicular to the vector from the nipple to the chest.

2.2.7 Bilateral and Temporal Registration

Most research in mammogram registration has been done in the area of bilateral and temporal mammogram comparison. However, the authors usually create a sophisticated registration method, but then compare the mammograms only using simple pixel-wise difference. This is a large drawback since the breasts similarity does not go to such an extent that they could be compared pixelwise. The methods also frequently rely on mammographic features which may not always be present in the mammograms.

In [59, 60] is a registration technique for temporal analysis only based on thin-plate spline transformation [61]. They first analyze the boundary curve to find reference points - the nipple, rib and axilla. Wavelet based feature detection is then used to find internal landmarks. The [60] uses SMF [62, 63] normalization before proceeding to registration.

The drawback of this otherwise very interesting method is that neither the rib nor the axilla are always visible in the mammogram. Thin-plate spline based approach is also used in [64].

[65] is also a temporal method only. It simply translates the breast to align the centers of the breast areas. This is used as an initial estimate of the position of a lesion in the prior image. Masses are then segmented using features to detect stellated lesions and focal mass lesions. Corresponding masses are then searched in the reference image based on Pearson's correlation measure. The size of the masses is compared assuming that malignant masses grow in time.

The method described in [66] deals also only with the comparison of temporal mammograms, with further conclusions being made. It is based on a general method for registering images with the presence of abnormalities. However, it needs the apriori knowledge about the distribution of abnormalities which is a major drawback. The registration and transformation are based on Bayesian MAP approach with minimization of the registration and deformation energy.

An interesting approach is proposed in [67]. The coordinate system is based on the distance of the equidistance line to the breast contour and the position on the line itself. The mammograms are then transformed into this new coordinate system and the comparison is then made using correlation. This approach is rather vulnerable to the fact that the bilateral mammograms do not have to display the same breast area.

In [68] the registration is done by aligning breast contours which serves as a guideline for affine transformation.

2.2.8 Contrast Measures

The contrast criterion is not uniquely defined [69] and many criteria, which are usually categorized into local, global and region based measures, are available. Another possible categorization is whether they use only monospectral information, e.g. WC, MC, EME, EMEE, AME, AMEE, SDME, C1, C2, C3 (2.16)-(2.27), RCC (2.32), or they use all three colour bands, e.g. Wlf_{Rsc} (2.30), BCC (2.33). Typical measures used are the Weber or Michelson contrast criteria. The Weber contrast [70] is

$$\uparrow WC = \frac{Y_{obj} - Y_{back}}{Y_{back}} \geq 0, \quad (2.16)$$

where \uparrow is the required criterion movement, Y_{obj}, Y_{back} are the object and background luminance, respectively. The Michelson contrast [71] is defined as

$$\uparrow MC = \frac{Y_{max} - Y_{min}}{Y_{max} + Y_{min}} \geq 0, \quad (2.17)$$

where Y_{max}, Y_{min} are the highest and lowest luminances. Several modifications [72, 73, 74] of this criterion which replace either Y_{max} or Y_{min} with Y_{mean} were also published.

2.2.8.1 Global Contrast Measures

The measure of enhancement (EME) based on a Weber-law-based contrast measure was proposed by Aghaian [75] and analogically the measure of enhancement by entropy (EMEE). The Michelson law measure of enhancement (AME) and its entropy modification, Michelson law measure of enhancement by entropy (AMEE), were later proposed by the same authors [76]. Panetta et al. [54] used these global monospectral contrast measures for mammogram enhancement assessment and introduced a second-derivative-like enhancement measure (SDME). The SDME results were found to be consistent with the mean opinion score (MOS) from seven human observers, while the AME, AMEE, EME, EMEE criteria were found to be inconsistent [54]. All these contrast measures assume an evaluated image divided into $k_1 \times k_2$ blocks.

$$\uparrow EME_{k_1, k_2} = \frac{1}{k_1 k_2} \sum_{l=1}^{k_1} \sum_{k=1}^{k_2} 20 \ln \left(\frac{Y_{max, k, l}}{Y_{min, k, l}} \right) \quad \langle 0; \infty \rangle, \quad (2.18)$$

$$\uparrow EMEE_{k_1, k_2} = \frac{1}{k_1 k_2} \sum_{l=1}^{k_1} \sum_{k=1}^{k_2} \left[\alpha \left(\frac{Y_{max, k, l}}{Y_{min, k, l}} \right)^\alpha \ln \left(\frac{Y_{max, k, l}}{Y_{min, k, l}} \right) \right] \quad \langle 0; \infty \rangle, \quad (2.19)$$

$$\downarrow AME_{k_1, k_2} = -\frac{1}{k_1 k_2} \sum_{l=1}^{k_1} \sum_{k=1}^{k_2} 20 \ln \left(\frac{Y_{max, k, l} - Y_{min, k, l}}{Y_{max, k, l} + Y_{min, k, l}} \right) \quad \langle 0; \infty \rangle, \quad (2.20)$$

$$\downarrow AMEE_{k_1, k_2} = \frac{-\alpha}{k_1 k_2} \sum_{l=1}^{k_1} \sum_{k=1}^{k_2} \left(\frac{Y_{max, k, l} - Y_{min, k, l}}{Y_{max, k, l} + Y_{min, k, l}} \right)^\alpha \ln \left(\frac{Y_{max, k, l} - Y_{min, k, l}}{Y_{max, k, l} + Y_{min, k, l}} \right) \quad \langle 0; \infty \rangle, \quad (2.21)$$

$$\downarrow SDME_{k_1, k_2} = -\frac{1}{k_1 k_2} \sum_{l=1}^{k_1} \sum_{k=1}^{k_2} 20 \ln \left(\frac{Y_{max, k, l} - 2Y_{center, k, l} + Y_{min, k, l}}{Y_{max, k, l} + 2Y_{center, k, l} + Y_{min, k, l}} \right) \quad \langle 0; \infty \rangle, \quad (2.22)$$

where α is a constant, $Y_{max, k, l}$, $Y_{min, k, l}$, $Y_{center, k, l}$ are the corresponding maximum, minimum, and center values, respectively.

The main disadvantage of these global measures is their insufficient robustness. They exhibit strong dependence on two single extreme brightness or darkness points (possibly outliers), while the overall contrast perception might be completely different.

2.2.8.2 Local Pixelwise Contrast Measures

Difference-of-Gaussians based contrast measures Three different local contrast measures ($C1, C2, C3$) based on the difference of Gaussians were introduced by Tadmor and Tolhurst [77]. These contrast measures (especially $C3$) should model the response of

the eye to the variations in contrast.

$$\begin{aligned}
 Cen(i, j) &= \exp \left[- \left(\frac{i}{\rho_c} \right)^2 - \left(\frac{j}{\rho_c} \right)^2 \right] , \\
 Sur(i, j) &= 0.85 \left(\frac{\rho_c}{\rho_s} \right)^2 \exp \left[- \left(\frac{i}{\rho_s} \right)^2 - \left(\frac{j}{\rho_s} \right)^2 \right] ,
 \end{aligned}$$

$$R_c(x, y) = \sum_{i=x-3\rho_c}^{x+3\rho_c} \sum_{j=y-3\rho_c}^{y+3\rho_c} Cen(i-x, j-y) Y_{i,j} , \quad (2.23)$$

$$R_s(x, y) = \sum_{i=x-3\rho_s}^{x+3\rho_s} \sum_{j=y-3\rho_s}^{y+3\rho_s} Sur(i-x, j-y) Y_{i,j} , \quad (2.24)$$

$$\uparrow C1(x, y) = \frac{R_c(x, y) - R_s(x, y)}{R_c(x, y)} \quad \langle 0; \infty \rangle , \quad (2.25)$$

$$\uparrow C2(x, y) = \frac{R_c(x, y) - R_s(x, y)}{R_s(x, y)} \quad \langle 0; \infty \rangle , \quad (2.26)$$

$$\uparrow C3(x, y) = \frac{R_c(x, y) - R_s(x, y)}{R_c(x, y) + R_s(x, y)} \quad \langle 0; \infty \rangle , \quad (2.27)$$

where ρ_c and ρ_s denote the radius for the centered and surrounding Gaussian respectively, $\rho_c < \rho_s$, and x, y are spatial indices.

Weighted-level framework The Weighted-Level Framework with Retinal-like sub-sampling contrast, Wlf_{Rsc} method [78], works in the CIELAB (or RGB) color space averaging the values of the actual bands. It computes the difference of Gaussians (2.23), (2.24)

$$DOG(x, y) = R_c(x, y) - R_s(x, y) > 0 , \quad (2.28)$$

contrast for the lightness and also for the two chromatic channels. The three independent measures of each channel are then merged by a weighted linear combination.

This method is based on the idea of the difference of Gaussians (DOG) combined with the Gaussian pyramid

$$Wlf_{Rsc,i} = \frac{1}{N_l} \sum_{l=1}^{N_l} \lambda_l E_l \{ C3_i \} , \quad (2.29)$$

$$\uparrow Wlf_{Rsc} = \sum_{k=1}^d c_k Wlf_{Rsc,i} > 0 , \quad (2.30)$$

where N_l is the number of levels in the Gaussian pyramid, $E_l \{ \dots \}$ is the mean value of the given contrast measure at the sub-sampled level l , d is the number of spectral bands, λ_l is

the weight of level l and $C3_i$ is from (2.27) computed on the i -th spectral channel, and c_i are the weights of each color channel. For the RGB color space Simone et al.[78] suggest c_i to be the variance of pixel values for the corresponding channel, while in the Lab color space they propose to use $c_i = 0.33 \forall i$.

2.2.8.3 Region of Interest Based Contrast Measures

Region contrast The contrast between two regions is computed on the basis of the average values of features of adjacent regions [79]:

$$\begin{aligned} c_{i,j} &= \frac{|\mu_i - \mu_j|}{\mu_i + \mu_j} \\ k_{i,j} &= \frac{|border(i) \cap border(j)|}{|border(i)|} \\ c_i &= \sum_{\forall R_j \text{ adj } R_i} k_{i,j} c_{i,j} \end{aligned} \quad (2.31)$$

$$\uparrow RCC = \frac{\sum_{\forall R_j} |R_j| c_j}{\sum_{\forall R_j} |R_j|} > 0 \quad (2.32)$$

where μ_i denotes the mean value of region i , $border(i)$ are the pixels on the border of region i , and $adj R_i$ are regions which are adjacent to region i . Equation (2.31) computes the contrast of i th region and equation (2.32) sums the global contrast.

Border contrast The contrast measure [80] computes the mean difference of pixel values along the border of a region of interest. For each region of interest R_i and all border pixels $b(R_i)$ it computes the mean pixel values μ_{in_j} and μ_{out_j} of small windows next to the border inside and outside of the desired region of interest, normalized by the image's maximum pixel value Y_{max} . The value of n_s is a normalization factor denoting the number of spectral bands of the image so that gray-scale images can be compared with multispectral ones.

$$\uparrow BCC = \frac{100}{Y_{max} \sqrt{n_s}} \sum_i |b(R_i)| \sum_i \sum_{j \in b(R_i)} \|\mu_{in_j} - \mu_{out_j}\| > 0 . \quad (2.33)$$

2.2.9 Texture Synthesis

Physically correct and convincing virtual models require not only detailed 3D shapes accorded with the captured scene, but also object surfaces covered with realistic nature-like surface material textures to enhance realism in virtual scenes. The primary purpose of any synthetic texture approach is to reproduce and enlarge a given measured texture image so that ideally both natural and synthetic texture will be visually indiscernible.

Texture synthesis can be primarily divided into sampling and model based methods [81]. Sampling approaches rely on sophisticated sampling from real texture measurements while

the model-based techniques describe texture data using multidimensional mathematical models and their synthesis is based on the estimated model parameters only. For details on these corresponding approaches, see survey articles [7, 81].

As we want to apply the textural models also for visual information analytical applications, we are interested in this work only in the mathematical textural models.

Experimental Data

All methods need experimental verification. In this chapter we present the databases we used in our experiments. Sec. 3.1 covers the mammogram databases, Sec. 3.2 covers the images we used during our work on texture synthesis and Sec. 3.3 covers the dermatological data.

3.1 Public Mammogram Databases

There are not many publicly available mammogram databases [82, 83, 84, 85, 86, 87], older databases like DDSM [84], MIAS [82] are digitized from the X-ray films, while newer databases like INbreast [86] are already digitally acquired. The databases that we use for our experiments are the INbreast database (covered in more detail in Sec. 3.1.1), the MIAS database (covered in more detail in Sec. 3.1.2) and the DDSM (see Sec. 3.1.3).

The LLNL/UCSF database [83] (<ftp://gdo-biomed.uc11nl.org/pub/mammo-db/>) contains 198 digitized films from 50 patients with 4 views per patient but only with 2 views from one mastectomy case.

The recent OPTIMAM database [87] shows good promise and we plan to use it for our experiments in the future. According to their homepage, it should currently contain over 170000 images which makes it to our knowledge the largest mammogram database (<https://medphys.royalsurrey.nhs.uk/imagedb/>).

The BancoWeb LAPIMO Database [88] was acquired at two hospitals using Senographe 500t and Senographe 600t mammographs and digitized by using two laser scanners Lumiscan 50 and Lumiscan 75 (<http://lapimo.sel.eesc.usp.br/bancoweb/>).

As far as we know, only the MIAS, DDSM and LLNL/UCSF databases are completely free to download. Other databases, such as the INbreast and OPTIMAM require anyone who wants to use it to sign an agreement whereas the LAPIMO database has a restricted server approach which needs to be validated by its administrators.

The survey of database features for the MIAS, DDSM, INbreast, LLNL and LAPIMO databases is listed in Tab. 3.1. An example of images from the three databases we used can be seen in Fig. 3.1.

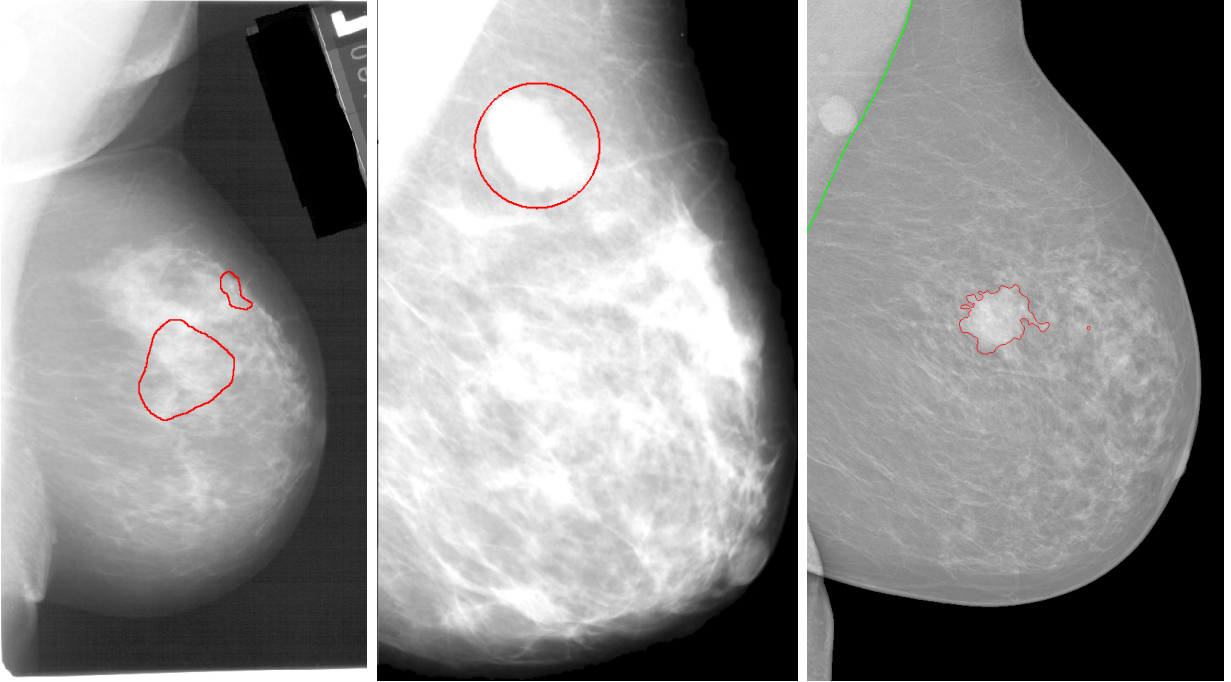


Figure 3.1: Example of images from different mammogram databases with ground truth. Left to right: DDSM, MIAS, INbreast.

3.1.1 INbreast

The INbreast database [86] is a mammographic database, with images acquired at a Breast Centre, located in a University Hospital (Hospital de São João, Breast Centre, Porto, Portugal). INbreast has a total of 115 cases (410 images) of which 90 cases are from women with both breasts (4 images per case) and 25 cases are from mastectomy patients (2 images per case). Several types of lesions (masses, calcifications, asymmetries, and distortions) are included. Accurate contours made by specialists are also provided in XML format.

Fig. 3.1 on the right shows an example of a mammogram from the INbreast database. The pectoral muscle is marked in green (the ground truth is supplied by the database) and regions of interest in red. We can see that this database provides high quality images with the most accurate outlines of regions of interest. The only drawback of the database is the relatively low number of images (410).

3.1.2 MIAS

The Mammographic Image Analysis Society Digital Mammogram Database (MIAS) [82] is a database with 322 medio-lateral oblique (MLO) 1024×1024 images digitized to 50 microns per pixel from the original X-ray filmscreen mammograms by the scanning micro-

	DDSM ([84])	INbreast ([86])	LAPIMO ([88])	LLNL ([83])	miniMIAS ([82])
n_{mam}	10480	410	1473	198	322
n_{views}	4	4	4	4	2
n_{gl}	16/12	14	12	12	8
x resolution	1411 – 5641	2560 – 3328			1024
y resolution	3256 – 7111	3328 – 4084			1024
normal	695	70	294	38	204
↓ benign	141	116	994	128	
benign	870	44			66
malignant	914	180	112	32	52
density	<i>ACR</i>	<i>ACR</i>	<i>no</i>	<i>no</i>	<i>own scale</i>
BI-RADS	<i>yes</i>	<i>yes</i>	<i>yes</i>	<i>no</i>	<i>no</i>

Table 3.1: Public Mammogram Databases: where (n_{mam}) is the number of mammograms, (n_{views}) number of views, (n_{gl}) number of grey levels in bits, and ↓ is benign without callback.

densitometer SCANDIG3. uses its own density description - fatty (\sim ACR BI-RADS a), fatty-glandular (\sim ACR BI-RADS b-c), dense-glandular (\sim ACR BI-RADS c-d).

MIAS mammographic images are available via the Pilot European Image Processing Archive (PEIPA) at the University of Essex <http://peipa.essex.ac.uk/ipa/info/mias.html>.

Fig. 3.1 in the middle shows an example of an image from the MIAS database. We can see the main drawback of this database at first glance - the regions of interest are provided only in the form of circles (the centre point coordinates and radius). Apart from that, the images have a quite good quality for digitized mammograms. The second drawback, same as for the INbreast database, is the low number of images.

3.1.3 DDSM

The Digital Database for Screening Mammography (DDSM) [84] is a database of mammograms digitized from original X-ray filmscreens in different resolutions and with associated ground truth and other information <http://marathon.csee.usf.edu/Mammography/Database.html>. This database was completed in 1999 and contains mammograms from four different sources using four different digitizers (DBA M2100 ImageClear, Howtek 960, Lumisys 200 Laser, Howtek MultiRad850) and 12 or 16 bits quantization. The database contains normal, benign, and histologically proven cancerous mammograms in four different views (left and right cranio-caudal (CC) and medio-lateral oblique (MLO)).

It is fully annotated according to the breast imaging reporting and data system (BI-RADS) assessment and breast density categories. The DDSM database is the largest free

3. EXPERIMENTAL DATA



Figure 3.2: Example of textures from our database. Left to right: rusty plate, bark, meadow, lichen.



Figure 3.3: Example of dermatological images.

database available. The database contains images obtained from three different digitizers. Although the quality is mostly acceptable, it contains very noisy images as well (e.g. Fig. 3.1 on the left). The outlines are specified pointwise but tend to be a bit larger than the actual region of interest, as seen in Fig. 3.1.

3.2 UTIA Pattern Recognition Department's Texture database

At the Institute of Information Theory and Automation's (UTIA) Pattern Recognition department we have collected over 2000 different images of homogeneous textures. The images are split into 34 classes ranging from natural textures of various scales such as flowers, lichen, meadows etc. to man made textures such as concrete, floor tiles, mosaic windows etc. The dimensions are 1536×1024 px.

We used a subset of these images for our work on texture synthesis. An example of images from our database can be seen in Fig. 3.2.

3.3 Dermatological Data

At the courtesy of Dr. Harald Kittler, Medical University of Vienna, in Vienna/Austria, we have at our disposal a set of 548 dermatological cases with images both benign and containing skin cancer. Fig. 3.3 shows an example of three images from the dermatological set we used.

Texture Models

There is no general texture model which is capable to model a vast variety of possible material textures. It is only possible to develop textural models optimal for certain subclasses of possible textures.

We have developed several multidimensional textural models which can be applied to physically correct material modeling as well as robust texture recognition. For all these models we have derived robust parameter estimation methods. Except for the spiral models (Sec. 4.2.2), fast efficient synthesis has been derived as well.

In Sec. 4.1 we describe our work on the Potts MRF - the surrogate Potts model parameters (Sec. 4.1.1) and the Hierarchical Potts random field (Sec. 4.1.2). Sec. 4.2 covers our generalizations of the CAR models (Secs. 4.2.1 and 4.2.2).

4.1 Potts MRF

4.1.1 Surrogate Potts Model Parameters

When working with the model, we can encounter two issues concerning its parameter β . The first one is that since it is numerically estimated using an iterative algorithm, it takes quite a long time to compute. The second one is that it is highly sensitive to small perturbations of region boundaries as well as noise. Fig. 4.1 shows two realizations of the Potts MRF that are visually indistinguishable. When computing their β parameter using the pseudo-likelihood method, however, the results are diametrically different. In texture synthesis, or rather texture mimicking, this fact leads to bad results when using just the β parameter.

To make up for this problem we have to find a measure that strongly correlates with the β parameter without the sensitivity to noise. Such a measure could be used in β 's stead for comparison of the manner of the texture and to give a hint as to whether a texture has greater or lesser β parameter than another texture. Fortunately, finding such a measure is not very hard. Here are several examples that we used in our experiments which are fast and easy to implement:

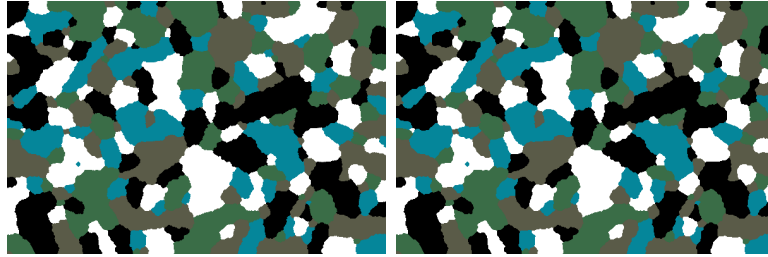


Figure 4.1: Two seemingly equal realizations of Potts model. Left $\beta = 2$, right $\beta = 3.15$.

- Sum of squares of region sizes ($area^2$)
- Sum of squares of continuous line segments of the same colour ($lines^2$)
- Sum of region perimeters ($perimeter$)

The top plot in Fig. 4.2 shows the development of the estimates of the β parameter as well as the proposed surrogate parameters during the first 30 iterations of Gibbs sampling of a 3 colour Potts field from random noise with a set $\beta = 1.5$. The values have been normalized to range $< 0, 1 >$ for better comparison. We used Gibbs sampling for this measurement because it takes more iterations to converge so that we could draw the plot. We can see that all the three proposed measures correlate with the β parameter (the precise correlations can be seen in Tab. 4.1).

The bottom plot in Fig. 4.2 shows the relative differences in each iteration in the variables when the synthesized Potts random field is iteratively smoothed by a 3×3 max-occurrence filter. The synthesized Potts field and the first two smoothed versions can be seen in Fig. 4.3 (since the following smoothed versions look almost the same, we left them out). We can see that whereas the β parameter changes by more than 50% in the first step and almost 30% in the second, the $area^2$, $lines^2$ and $perimeter$ surrogate parameters change only by 4%, 13% and 24% respectively in the first iteration and almost negligibly thereafter.

Another thing that we can notice is that when synthesized from random noise, the measures as well as β behave at first almost monotonously until reaching the equilibrium when the β starts to oscillate. We take advantage of this property for our modified SW synthesis algorithm, which is described in Sec. 5.1.3.

4.1.2 Hierarchical Potts model

The Potts model can be effectively used in texture synthesis as a control field to decide which texture type to use in which part of the resulting image. For the texture synthesis based on the Potts model we use a CMRF model with posterior probability defined as

$$P(X, Y | \tilde{Y}) = P(Y | X, \tilde{Y})P(X | \tilde{Y})$$

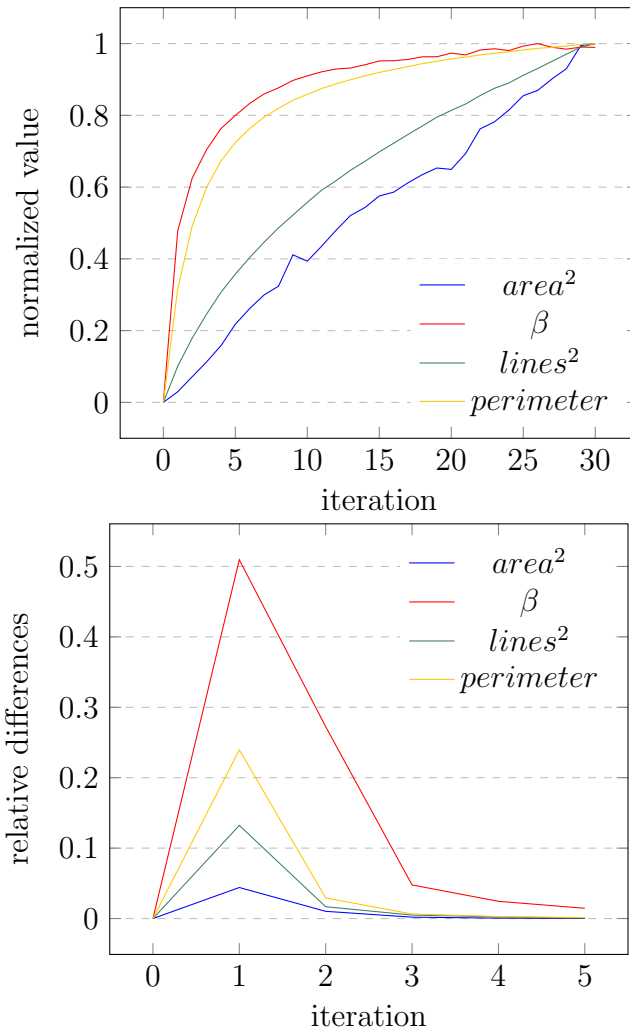


Figure 4.2: Plot of the β parameter and surrogate parameters for the Potts model. Top: development during synthesis starting at noise, bottom: development for progressive noise reduction.

Correlation	$area^2$	β	$lines^2$	$perimeter$
$area^2$	1,00	0,75	0,99	0,83
β	0,75	1,00	0,83	0,99
$lines^2$	0,99	0,83	1,00	0,90
$perimeter$	0,83	0,99	0,90	1,00

Table 4.1: Correlation between the β parameter and surrogate parameters for the Potts model.

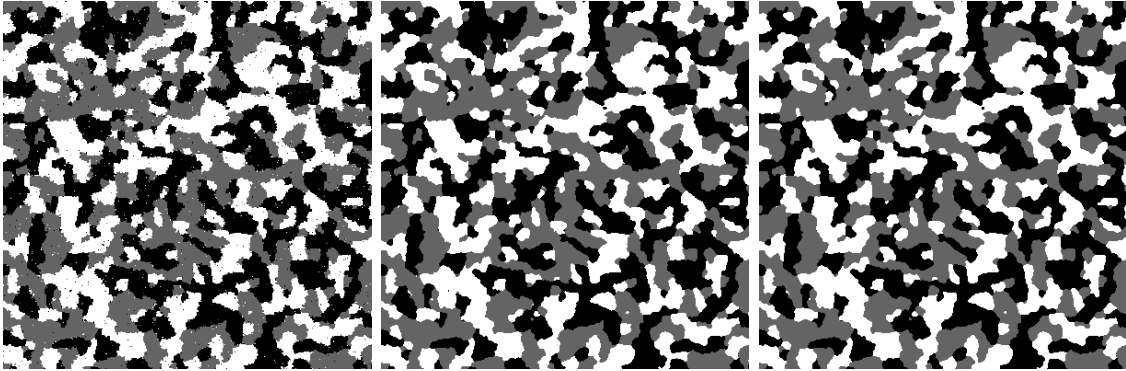


Figure 4.3: Left to right are the original image and its first two successively smoothed versions.

where X is the principal field modeled by the Potts MRF that controls regional switching to local texture models

$$Y = \bigcup_{i=1}^K {}^iY$$

where K denotes the number of texture types. Y are modeled using the 3D causal autoregressive random (3DCAR) field model [8, 89]. The \tilde{Y} is the original texture which is used to train the X and Y models.

The training itself is done using a two step approximation

$$\check{X} = \arg \max_{X \in \Omega_X} P(X|\tilde{Y})$$

$$\check{Y} = \arg \max_{Y \in \Omega_Y} P(Y|\check{X}, \tilde{Y})$$

This approximation imposes a significant simplification to the training process, because we can apply simple analytical estimation of the local MRF models.

The resulting thematic control map \check{X} is represented by the hierarchical two-scale Potts model

$$\check{X}^{(a)} = \frac{1}{Z^{(a)}} \exp \left\{ -\beta^{(a)} \sum_{s \in I_r} \delta_{X_r^{(a)} X_s^{(a)}} \right\} \quad (4.1)$$

where Z is the appropriate normalizing constant and $\delta(\cdot)$ is the Kronecker delta function.

The rough scale upper level Potts model ($a = 1$) regions are further elaborated with the detailed fine scale level ($a = 2$) Potts model which models the corresponding sub-regions in each upper level region.

The parameter $\beta^{(a)}$ for both level models is estimated using an iterative estimator which starts from the upper β limit (β_{\max}) and adjusts (decreases or increases) its value until the Potts model regions have similar parameters (average inscribed squared region

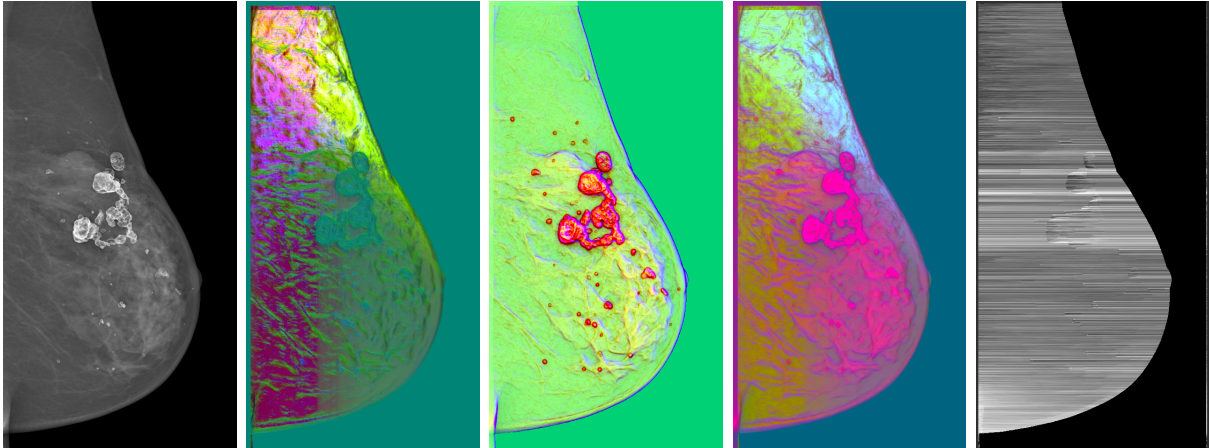


Figure 4.4: Typical problem of the CAR model – causality inertia. Left to right: original image, enhancements by prediction probability, prediction errors, combined enhancement and the γ parameters of the 2DCAR model.

size and/or the region’s perimeter) with the target texture switching field. The estimator is presented in more detail in Sec. 5.1.3.

This iterative estimator is faster and gives more resembling results with the target texture than the alternative maximum pseudo-likelihood method [90].

4.2 CAR Model Generalizations

The adaptive CAR models [9] that we are using in our work (both 2D and 3D) are defined in such a way that the spatial multiindex $r = [r_1, r_2]$ denoting history of movements on the lattice I does not have a clearly specified movement direction. Traditionally, it is presumed that the direction is row-wise left to right, top to bottom. This is indeed convenient in case of using the model for texture synthesis but in case of texture analysis, thanks to the artificial causality of the model, for each pixel the model neglects at least one half of the context of the data space dependencies. In Sec. 4.2.1 we propose an approach to broaden the context of the CAR model for texture analysis.

Another issue of the CAR models is the inertia of its parameters when there are too big differences in texture. An example can be seen in the analysis of mammogram in Fig. 4.4 (analysis done by method described in Sec. 7.3), where the large necrotic calcification influences the parameters so much that they never return to normal after encountering it. This manifests in the pictures as the half-planes in the prediction probability based and combined enhancement (for details on these enhancements, refer to Sec. 7.3) divided by the calcification cluster. The best way to see the inertia are the lingering lines in the γ parameters in the last image of Fig. 4.4. To make up for it, we propose the spiral CAR models in Sec. 4.2.2.

4.2.1 Directional CAR models

We propose a directional generalization to the CAR model. This generalization was successfully applied in methods for breast density classification (published in [A.6], described in Chapter 6) and mammogram texture enhancement (under review in [A.8], described in Chapter 7).

Let $r = [r_1, r_2, \phi]$ be the spatial multiindex denoting the history of movements on the rectangular lattice I , where r_1, r_2 are row and column indices, and ϕ are the possible model development directions:

$$\phi \in \{0^\circ, 45^\circ, 90^\circ, 135^\circ, 180^\circ, 225^\circ, 270^\circ, 315^\circ\} .$$

Note that although the model can use any directional angle, only the selected 8 directions allow us to avoid inevitable interpolation on the rectangular lattice.

The directional CAR model (both 2D and 3D variants) can be expressed as a stationary causal uncorrelated noise-driven autoregressive process:

$$Y_r = \gamma_\phi X_r + e_r , \quad (4.2)$$

where γ_ϕ are the parameter vectors for each direction ϕ , X_r is a support vector of $[Y_{r-s_1}, \dots, Y_{r-s_n}]^T$ where $s \in I_r^c$.

The parameters are estimated in the same way as for classical CAR models. The sole change that needs to be done is the transformation of the contextual neighborhood to take into account the direction of movement on the lattice. Presuming that I_r^c are the coordinates for the causal neighborhood with $\phi = 0^\circ$, the coordinates of the transformed neighborhood $I_r'^c$ are as follows:

$$\phi = \begin{cases} 45^\circ : & I_{r_1}'^c = I_{r_1}^c & I_{r_2}'^c = I_{r_1}^c + I_{r_2}^c \\ 90^\circ : & I_{r_1}'^c = I_{r_2}^c & I_{r_2}'^c = I_{r_1}^c \\ 135^\circ : & I_{r_1}'^c = -I_{r_1}^c & I_{r_2}'^c = I_{r_1}^c + I_{r_2}^c \\ 180^\circ : & I_{r_1}'^c = -I_{r_1}^c & I_{r_2}'^c = I_{r_2}^c \\ 225^\circ : & I_{r_1}'^c = -I_{r_1}^c & I_{r_2}'^c = I_{r_2}^c - I_{r_1}^c \\ 270^\circ : & I_{r_1}'^c = I_{r_2}^c & I_{r_2}'^c = -I_{r_1}^c \\ 315^\circ : & I_{r_1}'^c = I_{r_1}^c & I_{r_2}'^c = I_{r_2}^c - I_{r_1}^c \end{cases} \quad (4.3)$$

For reverse secondary movement in the same directions (that is, e.g., left to right, bottom to top instead of top to bottom), the transformations are computed analogously.

4.2.2 Spiral Models

As was already discussed at the beginning of Sec. 4.2 and shown in Fig. 4.4, the CAR model suffers from inertia which makes it keep the values of parameters over too large context in case of rapid changes in texture and thus lose the locality of the texture description. This

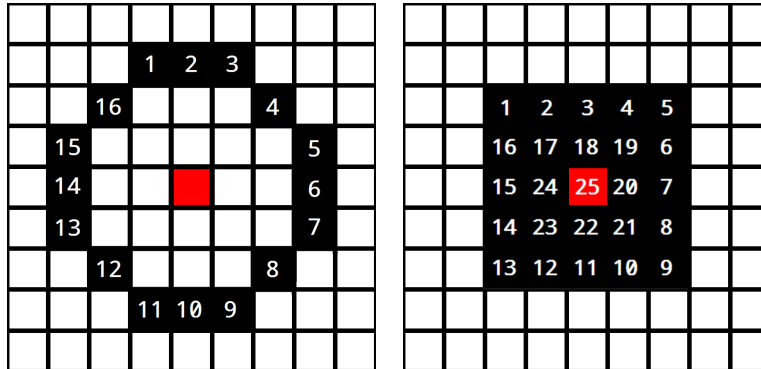


Figure 4.5: The paths of the two “spirals” in an image. Left: octagonal, right: rectangular. The numbers designate the order in which the pixels are traversed and the red square means the center pixel.

can be made up for by not running the model through the whole image but instead on a limited area following a circular or “spiral” like path.

The spiral CAR model is the same as the directional CAR model (4.2) with the exception that the movement r on lattice I takes the form of circular or spiral like paths as seen in Fig. 4.5. The causal neighborhood I_r^c has to be transformed (4.3) for each direction in the traversed path. The paths used can be arbitrary as long as they keep transforming the causal neighborhood I_r^c in such a way that all neighbors of a pixel have been visited by the model in previous steps. We shall call all these paths spirals further on. We have developed and implemented two types of spiral paths - octagonal (Fig. 4.5 on the left) and a rectangular spiral (Fig. 4.5 on the right). During our experiments they exhibited comparable results with the octagonal path being faster thanks to its consisting of fewer pixels for the same radius.

After the whole path is traversed, the parameters for the center pixel (shown as red square in Fig. 4.5) of the spiral are estimated. This can be done either for every pixel in the image or only for a subset of pixels, interpolating the values inbetween. Multiple parameter sets can be computed for every pixel based on the size and shape of the spiral used with the model.

Contrary to the standard CAR model, since this model’s equations do not need the whole history of movement through the image but only the given one spiral, the spiral CAR models can be easily parallelized. If the spiral paths used have circular shape, the spiral CAR models exhibit rotational invariant properties thanks to the CAR model’s memory of all the visited pixels.

This model is promising but its applications are still preliminary and we intend to develop them further in our future work.

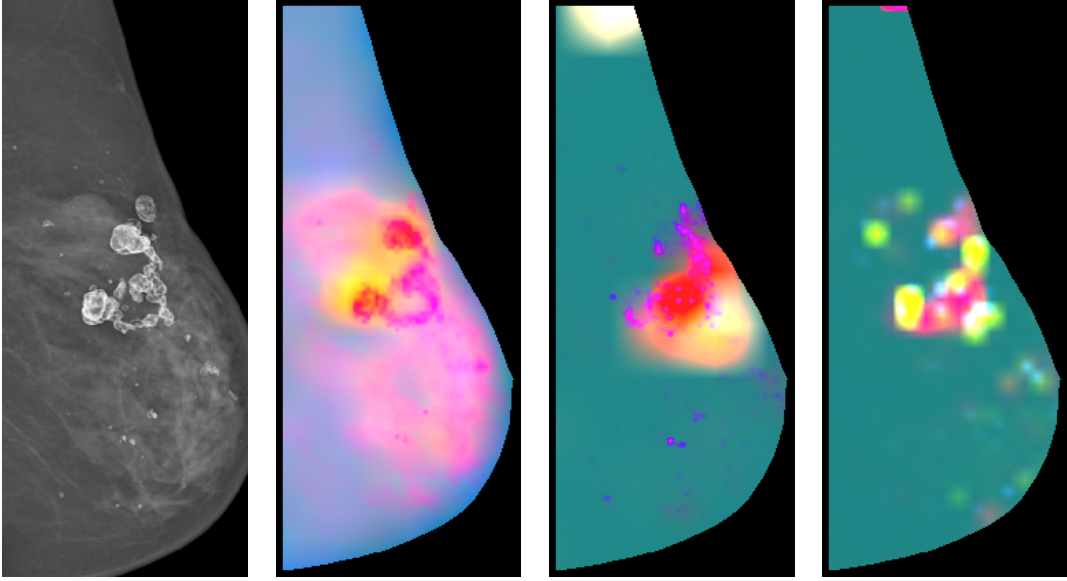


Figure 4.6: Rectangular spiral, left to right: original, α_1 , α_2 , α_3 .

4.2.2.1 Preliminary experiments

During our tests, we used the following illumination invariant features of the 3DCAR model [9]:

$$\begin{aligned}\alpha_1 &= 1 + Z_r^T V_{zz}^{-1} Z_r \\ \alpha_2 &= \sqrt{\sum_r (Y_r - \hat{\gamma} Z_r)^T \lambda^{-1} (Y_r - \hat{\gamma} Z_r)} \\ \alpha_3 &= \sqrt{\sum_r (Y_r - \mu)^T \lambda^{-1} (Y_r - \mu)}\end{aligned}$$

Figs. 4.6 and 4.7 show examples of spiral 2DCAR model features computed on a mammogram with which the classical 2DCAR would have inertia based problems (Fig. 4.4). The images were created by computing the spiral models for radii 1 – 10px, applying the Karhunen-Loeve transform and taking the most significant 3 planes as r, g and b channels.

We have also tried to use the spiral CAR features for unsupervised segmentation of the rotational invariant set from the Prague Texture Segmentation Benchmark (<http://mosaic.utia.cas.cz>). The unsupervised segmentation method used was published in [91]. Although these results have been extensively tested on the benchmark, we intend to apply this promising model on medical applications in our future work. Tab.4.2 shows the comparison of the spiral 3DCAR model with Multidirectional 3DCAR model and plain 3DCAR. All of them used the same neighborhood, forgetting constant and the illumination

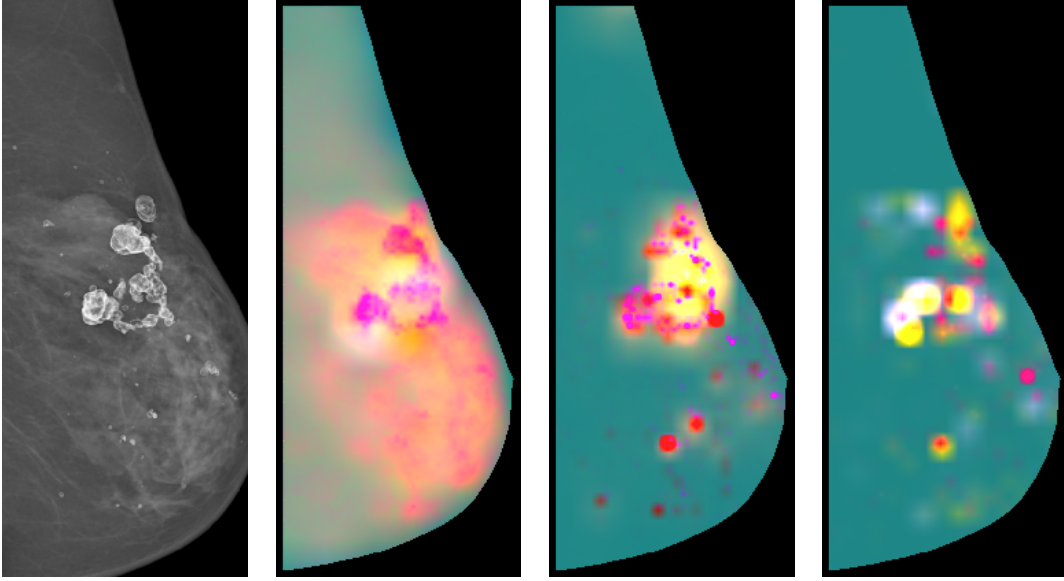


Figure 4.7: Octagonal spiral, left to right: original, α_1 , α_2 , α_3 .

invariant features α_1 , α_2 and α_3 . The segmentation results can be seen in App. A. We can see that the spiral 3DCAR model exhibited better results than the Multidirectional 3DCAR model, which in turn showed better results than the plain 3DCAR. For more detailed information on the benchmark criteria and results, please refer to [92].

	Benchmark – Colour (Rot. Inv.)		
	Spiral 3DCAR	Multidirectional 3DCAR	3DCAR
↑ <i>CS</i>	47.10 ¹	38.57 ²	36.68 ³
↓ <i>OS</i>	61.32 ³	47.08 ¹	47.70 ²
↓ <i>US</i>	9.70 ¹	14.50 ²	25.18 ³
↓ <i>ME</i>	16.35 ²	22.86 ³	15.09 ¹
↓ <i>NE</i>	16.30 ²	23.67 ³	14.87 ¹
↓ <i>O</i>	26.19 ¹	30.61 ²	33.97 ³
↓ <i>C</i>	98.52 ³	92.96 ¹	94.69 ²
↑ <i>CA</i>	65.92 ¹	60.87 ²	57.09 ³
↑ <i>CO</i>	71.71 ¹	67.20 ²	66.22 ³
↑ <i>CC</i>	86.25 ¹	81.76 ²	75.49 ³
↓ <i>I.</i>	28.29 ¹	32.80 ²	33.78 ³
↓ <i>II.</i>	4.47 ¹	5.65 ²	6.19 ³
↑ <i>EA</i>	74.58 ¹	70.01 ²	65.36 ³
↑ <i>MS</i>	65.39 ¹	58.32 ²	54.60 ³
↓ <i>RM</i>	4.19 ¹	4.97 ²	7.17 ³
↑ <i>CI</i>	76.42 ¹	71.92 ²	67.43 ³
↓ <i>GCE</i>	12.55 ¹	13.08 ²	13.17 ³
↓ <i>LCE</i>	6.96 ¹	7.91 ³	7.81 ²
↓ <i>dD</i>	16.56 ¹	19.30 ²	20.06 ³
↓ <i>dM</i>	14.47 ¹	16.89 ²	21.05 ³
↓ <i>dVI</i>	16.01 ³	15.72 ²	14.64 ¹

Table 4.2: Colour (Rot. Inv.) benchmark results for Spiral 3DCAR, Multidirectional 3DCAR, 3DCAR; (Benchmark criteria: CS = correct segmentation; OS = over-segmentation; US = under-segmentation; ME = missed error; NE = noise error; O = omission error; C = commission error; CA = class accuracy; CO = recall - correct assignment; CC = precision - object accuracy; I. = type I error; II. = type II error; EA = mean class accuracy estimate; MS = mapping score; RM = root mean square proportion estimation error; CI = comparison index; GCE = Global Consistency Error; LCE = Local Consistency Error; dD = Van Dongen metric; dM = Mirkin metric; dVI = variation of information).

Texture Synthesis

During our work on texture synthesis, we focused mainly on the Potts random field and its applications as a control field for the Compound Markov random field models, which are currently our best texture synthesis models. More specifically, we use it to switch between several local models for the synthesis of local textures.

This chapter is organized as follows: Sec. 5.1 presents the hierarchical Potts MRF synthesis and describes our method for alternate Potts MRF parameter estimation applied to our modification of the Swendsen-Wang algorithm for texture synthesis (Sec. 5.1.3). Then we examine the possibilities of using the Potts model for the synthesis of mosaic-like textures (Sec. 5.2). We conclude the chapter with example texture synthesis results (Sec. 5.4).

Physically correct realistic modeling of material surfaces respecting illumination and viewing changes require sophisticated nontrivial mathematical models. The purpose of texture synthesis is to represent and enlarge a given measured textural data space so that ideally both natural and synthetic texture will be visually indiscernible and simultaneously contain all necessary information for accurate material recognition.

Current state-of-the-art compound Markov random field models (CMRF) consist of several sub-models each having different characteristics along with an underlying structure model which controls transitions between these sub models [93]. CMRF models were successfully applied to image restoration [93, 94, 95, 96], segmentation [97], or modeling [A.1, 98, 99]. However, these models always require demanding numerical solutions with all their well known drawbacks. The exceptional CMRF [98] model allows analytical synthesis at the cost of a slightly compromised compression rate.

5.1 Hierarchical Potts Synthesis

In [A.1] we proposed a hierarchical Potts model based texture synthesis. This method can be easily applied to synthesizing numerous natural textures such as lichen, thawing snow, rust on metal plates, clouds, etc. It is covered in detail in the following sections:

5.1.1 Compound Markov Model

Let us denote a multiindex $r = (r_1, r_2)$, $r \in I$, where I is a discrete 2-dimensional rectangular lattice and r_1 is the row and r_2 the column index, respectively. $X_r \in \{1, 2, \dots, K\}$ is a random variable with natural number value (a positive integer), Y_r is multispectral pixel at location r and $Y_{r,j} \in \mathcal{R}$ is its j -th spectral plane component. Both random fields (X, Y) are indexed on the same lattice I . Let us assume that each multispectral observed texture \tilde{Y} (composed of d spectral planes e.g. $d = 3$ for colour textures) can be modeled by a compound Markov random field model, where the principal Markov random field (MRF) X controls switching to a regional local MRF model $Y = \bigcup_{i=1}^K {}^iY$. Single K regional submodels iY are defined on their corresponding lattice subsets iI , ${}^iI \cap {}^jI = \emptyset \quad \forall i \neq j$ and they are of the same MRF type. They differ only in their contextual support sets iI_r and corresponding parameters sets ${}^i\theta$. The CMRF^{P3AR} model has posterior probability

$$P(X, Y | \tilde{Y}) = P(Y | X, \tilde{Y})P(X | \tilde{Y}) \quad (5.1)$$

and the corresponding optimal MAP solution is:

$$(\hat{X}, \hat{Y}) = \arg \max_{X \in \Omega_X, Y \in \Omega_Y} P(Y | X, \tilde{Y}) P(X | \tilde{Y}) ,$$

where Ω_X, Ω_Y are corresponding configuration spaces for random fields (X, Y) .

To avoid iterative MCMC MAP solution, we propose the following two step approximation:

$$(\check{X}) = \arg \max_{X \in \Omega_X} P(X | \tilde{Y}) , \quad (5.2)$$

$$(\check{Y}) = \arg \max_{Y \in \Omega_Y} P(Y | \check{X}, \tilde{Y}) . \quad (5.3)$$

This approximation significantly simplifies the CMRF^{P3AR} estimation because it allows to take advantage of simple analytical estimation of regional MRF models in (5.3).

5.1.2 Region Switching Markov Model

The principal MRF ($P(X | \tilde{Y})$) is represented by a flexible K -state hierarchical Potts random field (described in Sec. 4.1.2).

The learning control random field \check{X} is estimated from the target texture using simple K-means clustering of \tilde{Y} in the RGB colour space into predefined number of K classes, where cluster indices are $\check{X}_r \quad \forall r \in I$ estimates. The number of classes K can be estimated using the Kullback-Leibler divergence and considering sufficient amount of data necessary to reliably estimate all local Markovian models.

The corresponding Potts models are synthesized by a modification of the fast Swendsen-Wang sampling method [100]. The regions sampled by the hierarchical Potts model are then filled by textures synthesized by the local Markov models (Sec. 5.3).

5.1.3 Modified SW Synthesis

In Sec. 4.1.1 we have described the issues with using only the estimated parameter β for mimicking a texture and proposed several texture measures which strongly correlate with the β parameter. Label such a measure as m . This measure helps us also with the problem of ending the SW algorithm - we can simply iterate and adjust the β parameter until m meets the desired conditions - e.g. until it is close enough to m of the texture we are trying to mimic.

The last issue to solve for texture synthesis using the SW algorithm is the distribution of colours. There are few textures which have the same ratio of all colours. To be able to sample textures with different ratios of different colours, we utilize a simple heuristic. We create virtual colours which symbolize the same colour in such a manner that the ratios between colours are kept the same as in the original (mimicked) picture and join them after the synthesis terminates.

The whole proposed algorithm is described in Alg. 5.1, where $SW(\check{X}, \beta)$ means “apply one step of the SW algorithm on \check{X} with the parameter β ”. The bounds β_{min} and β_{max} should be set to such values that β_{min} leads to complete noise and β_{max} leads to one continuous colour. Usually, $\beta_{min} = 0$ and $\beta_{max} = 20$ suffice.

5.2 Mosaics

This section introduces a method for modeling mosaic-like textures using a multispectral parametric Bidirectional Texture Function (BTF) compound Markov random field model (CMRF) which we published in [A.4]. It can be used to model the irregular texture with linear region borders of many man made materials such as stonework, floor tiles, stained glass mosaics or natural textures such as cracks in nacre.

The compound Markov random field model consists of several sub-models each having different characteristics along with an underlying structure model which controls transitions between these sub models. The proposed model uses the Potts random field for distributing local texture models in the form of analytically solvable wide-sense BTF Markovian representation for single regions among the fields of a mosaic. The control field of the BTF-CMRF is generated by the Potts random field model build on top of the adjacency graph of a measured mosaic. The Potts MRF parameter is estimated from the adjacency graph of the mosaic approximated by the Voronoi diagram. The Voronoi diagram was chosen due to its suitable representation of the intended class of the modeled man made textures and simultaneously due to the simplicity of its estimation and synthesis. The compound random field synthesis combines the modified fast Swendsen-Wang Markov Chain Monte Carlo sampling of the hierarchical Potts MRF part with the fast and analytical synthesis of single regional MRFs. The local texture regions (not necessarily continuous) are represented by an analytical BTF model which consists of single factors modeled by the adaptive 3D causal auto-regressive (3DCAR) random field model. The 3DCAR model can be analytically estimated as well as synthesized thus avoiding a time consuming Monte

Algorithm 5.1 Modified SW synthesis pseudocode.

Input: input texture \tilde{Y} , texture measure m , threshold τ and bounds β_{min} and β_{max} **Initialize:**

$$m_{in} \leftarrow m(\tilde{Y})$$

$$\check{X}^0 \leftarrow noise$$

Run:**repeat****repeat**

$$t \leftarrow t + 1$$

$$\check{X}^{t+1} \leftarrow SW(\check{X}^t, \beta_{max})$$

$$m_x \leftarrow m(\check{X}^{t+1})$$

until $m_x > m_{in}$ ▷ If $m_x < m_{in}$ after a number of steps, raise β_{max} by a small factor.*Update bounds:*

$$\beta' \leftarrow \frac{\beta_{max} + \beta_{min}}{2}$$

$$m_l \leftarrow m(\check{X}^t)$$

$$\check{X} \leftarrow SW(\check{X}^t, \beta')$$

$$m_x \leftarrow m(\check{X})$$

if $m_l > m_x$ **then**

$$\beta_{max} \leftarrow \beta'$$

else

$$\beta_{min} \leftarrow \beta'$$

end if**until** $\frac{|m_x - m_{in}|}{m_{in}} < \tau$ **Output:** Synthesized field \check{X} , estimated parameter β'

Carlo sampling.

We propose a hierarchical Voronoi CMRF^{PV3AR} model which combines two types of parametric Markov random field (MRF) models with a parametric mosaic model [101]. One MRF model can be analytically solved, while the other can use the exceptionally fast iterative Swendsen-Wang Markov Chain Monte Carlo (MCMC) sampling [100] for its synthesis.

5.2.1 Potts Field-Based Mosaic Modeling

The control field (X) of the CMRF^{PV3AR} is a mosaic represented as a Voronoi diagram [102] and the distribution of the particular colors (texture classes) of the mosaic is modeled as a Potts random field which is built on top of the adjacency graph (G) of the mosaic. The Voronoi diagram was chosen due to its suitable representation of the intended class of

the modeled man made textures and simultaneously due to the simplicity of its estimation and synthesis.

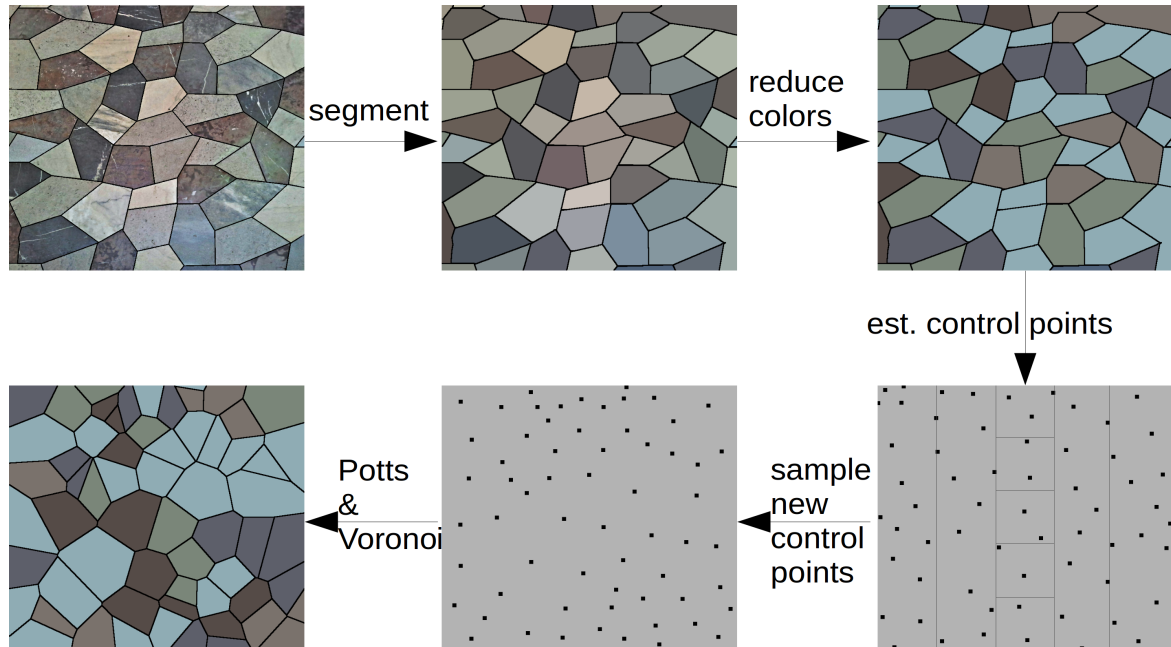


Figure 5.1: Control field synthesis algorithm flowchart.

The control field synthesis is performed as illustrated in Fig. 5.1. The algorithm requires an input in the form of a segmented mosaic with distinguishable regions of the same texture type.

Since the Potts field needs a reasonably small number of classes (in our experience, in the case of mosaics it works best with about 5-15 classes), the number of classes is reduced using simple K-means clustering of \tilde{Y} in the RGB colour space into a predefined number of K classes, where the cluster indices are $\check{X}_u \quad \forall u \in V$ estimates. The number of classes K can be estimated using the Kullback-Leibler divergence, considering sufficient amount of data necessary to reliably estimate all local Markovian models.

After that follows the identification of the mosaic field centers and the estimation of the parameters of the 2D discrete point process which samples the control points of the newly synthesized Voronoi mosaic. This is done using a 2D histogram, which has shown to be sufficient for the good quality estimate. The only other parameter is the number of points to be sampled, which grows linearly with the required area of the synthetic image in the case of texture enlargement applications.

With the control points for the Voronoi mosaic cells having been sampled, we compute the Voronoi diagram and optionally mark the delimiting edges between adjacent cells. The assignment of a regional texture model to each mosaic cell (the principal MRF $(P(X | \tilde{Y}))$) is then mapped by the flexible K -state Potts random field [103, 104].

Let us denote $G = (V, E)$ the adjacency graph of the mosaic areas and

$$N_u = \{\forall v \in V : (u, v) \in E\}, \quad u \in V$$

the 1st order neighborhood, where V, E are the vertex and edge sets. Vertices correspond to the particular areas in the mosaic and there is an edge between two vertices iff their corresponding areas are directly next to each other.

The resulting thematic control map \check{X} is represented by the Potts model for a general graph

$$p(\check{X}|\beta) = \frac{1}{Z} \exp \left\{ -\beta \sum_{u \in V, v \in N_u} \delta(X_u, X_v) \right\} \quad (5.4)$$

where Z is the appropriate normalizing constant and $\delta()$ is the Kronecker delta function. The parameter β is estimated from the K-means clustered input mosaic using the maximum pseudo-likelihood method described by Levada [90] (described in Sec. 2.1.1.3).

The corresponding Potts models are synthesized using the fast Swendsen-Wang sampling method [100], although for smaller fields, which the mosaics undoubtedly are, other sampling MCMC methods, such as the Gibbs sampler [94] or the Metropolis algorithm [105], should also work with sufficient speed.

5.3 Local Markov Models

For both the the presented compound models (Sec. 5.1 and Sec. 5.2), the local i -th texture region (not necessarily continuous) is represented by the adaptive 3D causal autoregressive (3DCAR) random field model [9, 10] because this model can be analytically estimated as well as synthesized (described in more detail in Sec. 2.1.1.2). Alternatively we could use spectrally decorrelated 2DCAR or 2D or 3D Gaussian Markov random field (GMRF) models [81, 106]. All these models allow analytical synthesis (see [81] for the corresponding conditions) and they can be unified in the following matrix equation form (i -th model index is further omitted to simplify notation):

$$Y_r = \gamma X_r + \epsilon_r, \quad (5.5)$$

where

$$X_r = [Y_{r-s}^T : \forall s \in I_r]^T. \quad (5.6)$$

is the $\eta \times d \times 1$ data vector with multiindices r, s, t , $\gamma = [A_1, \dots, A_\eta]$ is the $d \times d \times \eta$ unknown parameter matrix with sub-matrices A_s .

In the case of d 2DCAR / GMRF models stacked into the model equation (5.5), the parameter matrices A_s are diagonal. Otherwise they are full matrices for general 3DCAR models [10]. The model functional contextual neighbour index shift set is denoted I_r and $\eta = \text{cardinality}(I_r)$.

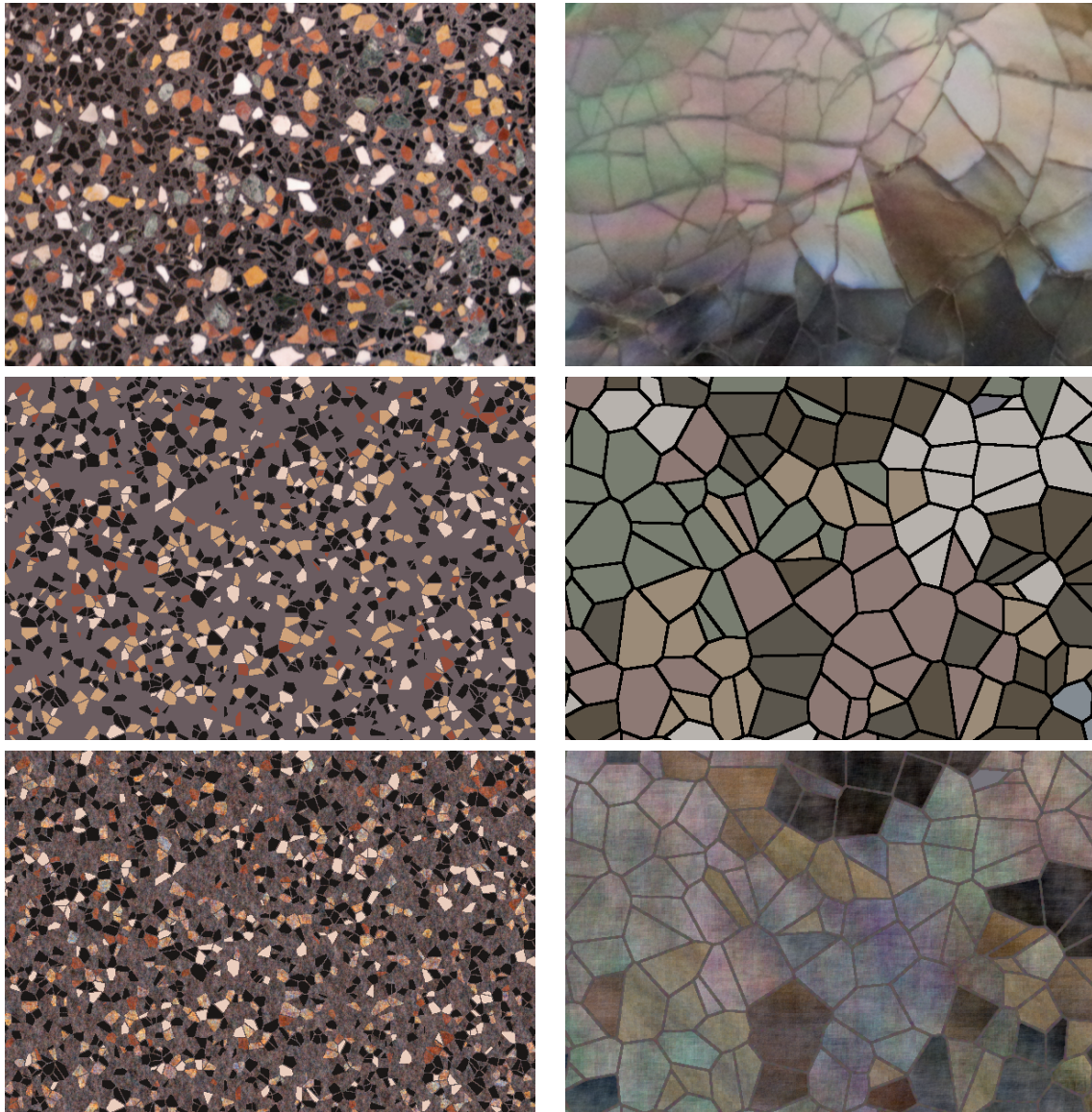


Figure 5.2: The original images of a floor (upper row left) and nacre stone (upper row right). Corresponding synthetic control fields - Voronoi Potts model (middle row), and the resulting synthetic CMRF^{PV3AR} model texture (bottom row).

GMRf and CAR models mutually differ in the correlation structure of the driving noise ϵ_r (5.5) and in the topology of the contextual neighbourhood I_r (see [81] for details). As a consequence, all CAR model statistics can be efficiently estimated analytically [9] while the GMRf statistics estimates require either numerical evaluation or some approximation ([81]).

Although an optimal causal (for (2D/3D)CAR models) functional contextual neigh-

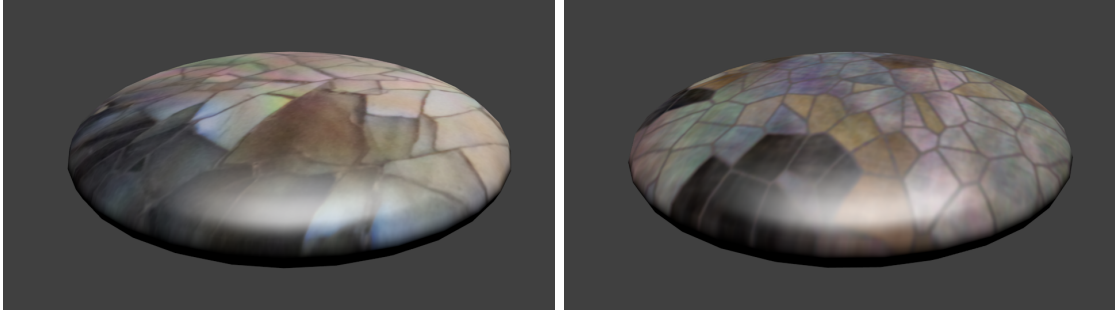


Figure 5.3: The nacre stone texture mapped to a 3D model created with Blender (left) and with synthetic texture (right).

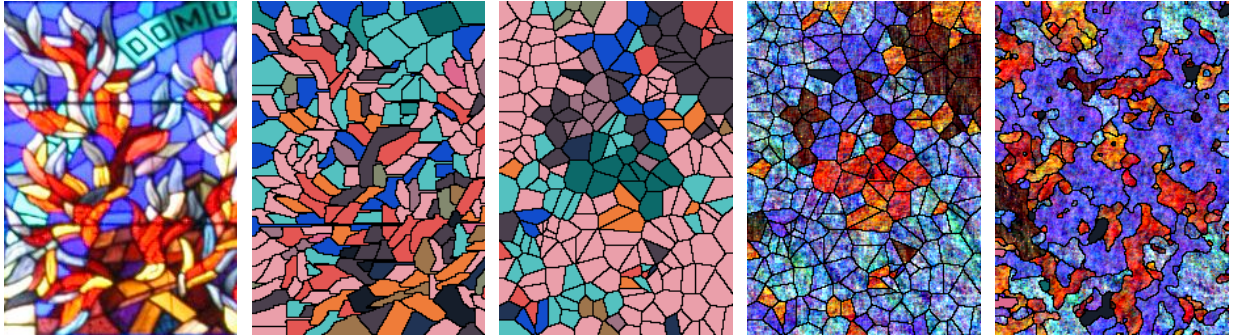


Figure 5.4: Texture synthesis of a stained glass window. From left to right: a stained glass photo, its segmentation, synthetic Voronoi Potts model control field, the final synthesis, and the comparison with the CMRF^{P3AR} model.

neighbourhood I_r can be solved analytically by a straightforward generalization of the Bayesian estimate in [9], we use faster approximation which does not need to evaluate statistics for all possible I_r configurations. This approximation is based on large spatial correlations. We start from the causal part of a hierarchical non-causal neighbourhood and neighbour locations corresponding to spatial correlations larger than a specified threshold (> 0.6) are selected. The i -th model synthesis is a simple direct application of (5.5) for both 2DCAR or 3DCAR models. GMRF model synthesis requires one FFT transformation at best [81]. 3DCAR / GMRF models provide better spectral modeling quality than the alternative spectrally decorrelated 2D models for motley textures at the cost of a small increase in the number of parameters to be stored.

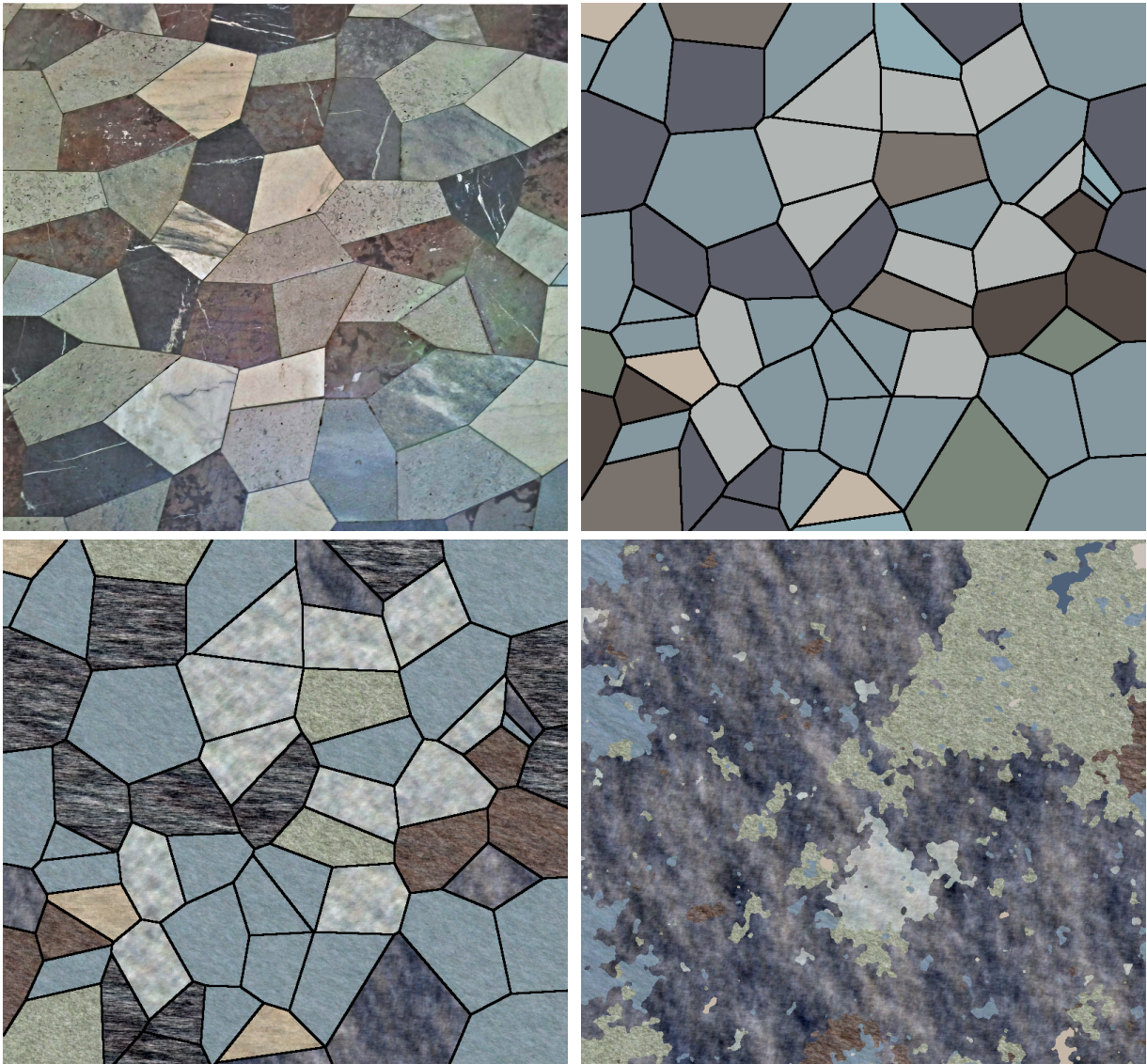


Figure 5.5: An example of the floor mosaic (top-left), the control field (top-right), CMRF^{PV3AR} synthesis, and the comparison with the CMRF^{P3AR} model result.

5.4 Results

5.4.1 CMRF^{P3AR} results

Fig. 5.7 shows our results with using the Potts model for texture synthesis. The left images show the original texture, middle ones are the Potts synthesized texture maps and the right ones are the final textures created by the compound model based on the 3DCAR random field.



Figure 5.6: An example of a the St. Vitus cathedral in Prague Castle stained glass window with some original panels replaced with our synthetic images.

The top row shows the synthesized texture of clouds, the middle one is lichen and the bottom one is a rusty plate.

5.4.2 CMRF^{PV3AR} results

We have tested the presented Voronoi CMRF^{PV3AR} model on selected colour textures from our extensive texture database (Fig. {5.2, 5.4, 5.5, 5.6}-floor, stained glass), which currently contains over 1500 colour textures. Examples on Figs.5.2 and 5.3 use 1st order neighbour for the Potts field on the Voronoi mosaic with $K = 5$ for the floor and $K = 8$ for the nacre. The examples of the stained glass in Fig. 5.4 use $K = 14$. The local texture models' causal neighbourhood is derived from the 4th order hierarchical contextual neighbourhood.

We have successfully tested the method mainly on man made surfaces such as different types of linoleum, smoothed stones, stone walls or stained glass and on selected natural materials such as chipped nacre. The visual quality of the resulting complex synthetic

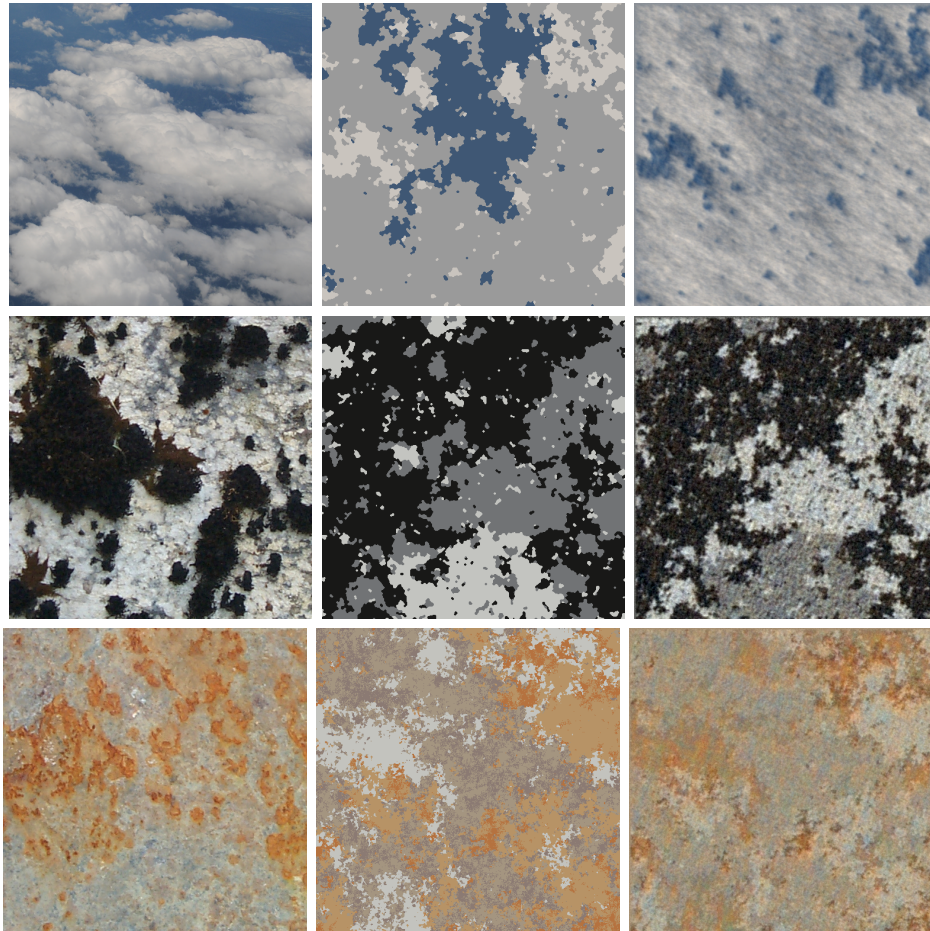


Figure 5.7: Potts CMRF synthesis. Left column shows original measurements, middle column is Potts control field, right column displays the resulting CMRF synthesis.

textures generally surpasses the outputs of the previously published simpler MRF models [10, 81, 106, 107]. Since there is no universally optimal texture modeling algorithm, neither the presented method can model every type of texture. Textures on which the algorithm will exhibit poor quality are regular textures or textures with fixed patterns such as most textile or knitted wool textures.

However, the model can be easily modified to use a different method for the creation of the control mosaic, which could better mimic the particular desired mosaic type, e.g. for brick walls, flooring materials, etc. The model can be easily generalized also for complex bidirectional texture function (BTF) models. The full BTF-CMRF^{PV3AR} variant of the presented model uses similar fundamental flowchart with the Markovian BTF model [107] (i.e., BTF space intrinsic dimensionality estimation, BTF space segmentation, BTF subspace MRF model estimation, subspace MRF model synthesis and interpolation of unmeasured BTF space parts), but allows to avoid its range map estimation, range map



Figure 5.8: An example of a wooden floor BTF measured mosaic (top row), modeled control field mosaic with measured BTF wood (middle row), and our synthetic BTF-CMRF^{PV3AR} model (bottom row), where the illumination azimuthal angle ϕ and elevation angle θ are successively for each column: $\phi = 0^\circ, \theta = 0^\circ$ for the left column, $\phi = 60^\circ, \theta = 60^\circ$ for the middle column and $\phi = 60^\circ, \theta = 240^\circ$ for the right column.

modeling and displacement filter steps, respectively. Fig. 5.8 shows an example of our BTF-CMRF^{PV3AR} applied on texture editing a BTF floor mosaic with wooden tiles.

Breast Tissue Density Classification

Mammographic breast density is very important but one of the most undervalued and underused risk factors in studies investigating breast cancer occurrence. The risk for breast cancer is four to six times higher in women with dense breasts [108]. Breast density may also decrease the sensitivity by up to 40 % [108], obscure tumours, or mimic breast cancer, and, thus, the accuracy of the mammography screening.

An increase in breast density can also be used to characterize the effects of hormone replacement therapy. Thus many papers [39, 40, 109, 110, 111, 112, 113] consider automatic breast density classification with different approaches in feature extraction, used classifiers, and tested databases.

This chapter presents the method for breast density segmentation that we published in [A.6] (Sec. 6.2) our work on developing a more accurate approach (Sec. 6.3) and a method for breast density classification based on the Potts model (Sec. 6.4).

Note that although the ACR BI-RADS standard labels breast densities with letters *a-d*, we use numerical designation in this chapter.

6.1 Breast Segmentation

When analyzing mammograms, the first thing that needs to be done is extracting the breast area from the image. In case of fully digital mammogram databases, this can usually be done using simple thresholding, as digital mammographs' output is usually already processed to have zero value background. Digitized mammograms, on the other hand, contain lots of background noise and the images frequently include labels and tags concerning the contents of the mammogram (see the left image of Fig. 6.1).

For the supervised segmentation of the breast area, we use a simple application of the Potts model (2.11) in combination with Gaussian mixtures (2.13):

$$P(X|Y, \theta_c, \beta) = \frac{1}{Z(\beta)} \exp \left\{ -\beta \sum_{r,s} J_{r,s} \delta(X_r, X_s) - \sum_r \log f(Y_r | \theta_c) \right\} ,$$



Figure 6.1: Example of breast segmentation. Left to right: original image, segmentation, extracted breast area.

where Y are the texture features for each pixel position r , $f(\bullet|\theta_c)$ are the trained Gaussian mixtures of the features of the breast/nonbreast areas (θ_c) and X is the final segmentation. The features used are the grayscale values of the first three levels of the Gaussian pyramid. The segmentation is done by synthesizing the Potts field using the iterated conditional modes [114] approach until there is no improvement in the energy of the field. The breast is then selected as the biggest non-background area.

6.2 Maximal Texture Type Occurrence Based Classification

6.2.1 Breast Texture Description

We presume that even though the ACR BI-RADS density description [27] specifies the different classes based on the ratio of fatty and dense areas in the breast, our texture model is able to distinguish between fatty, heterogeneous, mostly dense and dense textures. Thus we can train the texture models as if the heterogeneity is a kind of texture within the breast.

For texture description we use the directional 2DCAR model's (4.2) γ_ϕ parameters extracted for each direction ϕ at each pixel location:

$$Y_r = \gamma_\phi X_r + e_r .$$

For performance efficiency we also downscale the images to 400 px height keeping the width/height ratio.

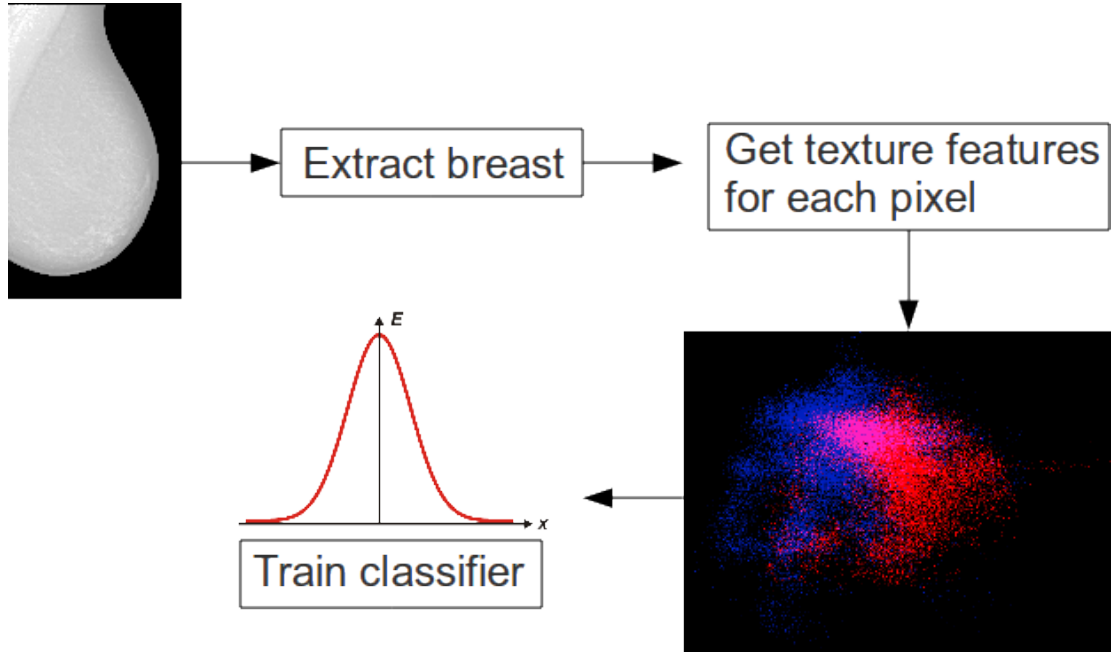


Figure 6.2: Classifier training flowchart.

6.2.2 Classifier Training

The classifier is trained as indicated in Fig. 6.2. After the breast area has been segmented from the image, we extract the feature vectors θ for each pixel $\theta = \{\gamma_{\phi_1}, \gamma_{\phi_2}, \dots\}$. The model directions used are $\phi_i \in \{90^\circ, 135^\circ, 180^\circ, 315^\circ\}$, for which we observed the best results.

We use the maximum-likelihood classifier based on the multivariate Gaussian distribution:

$$f(X|C) = \frac{1}{\sqrt{(2\pi)^k |\Sigma_C|}} e^{(-\frac{1}{2}(\theta - \mu_C)^T \Sigma_C^{-1} (\theta - \mu_C))} \quad (6.1)$$

where C is the BI-RADS density value of the particular mammogram. μ_C is the mean value of class C and Σ_C is the corresponding covariance matrix.

This way we estimate the feature distribution of each BI-RADS density class.

6.2.3 Feature Space Visualisation

To confirm the correctness of our chosen texture model for the application of breast texture modeling, we visualised the feature space, distinguishing the different density types with the colour of the pixels. We extracted the feature values for all the pixels of different breasts and applied the Karhunen-Loeve transform, taking values of the 2 most significant components as the x and y coordinates of the features to be displayed.

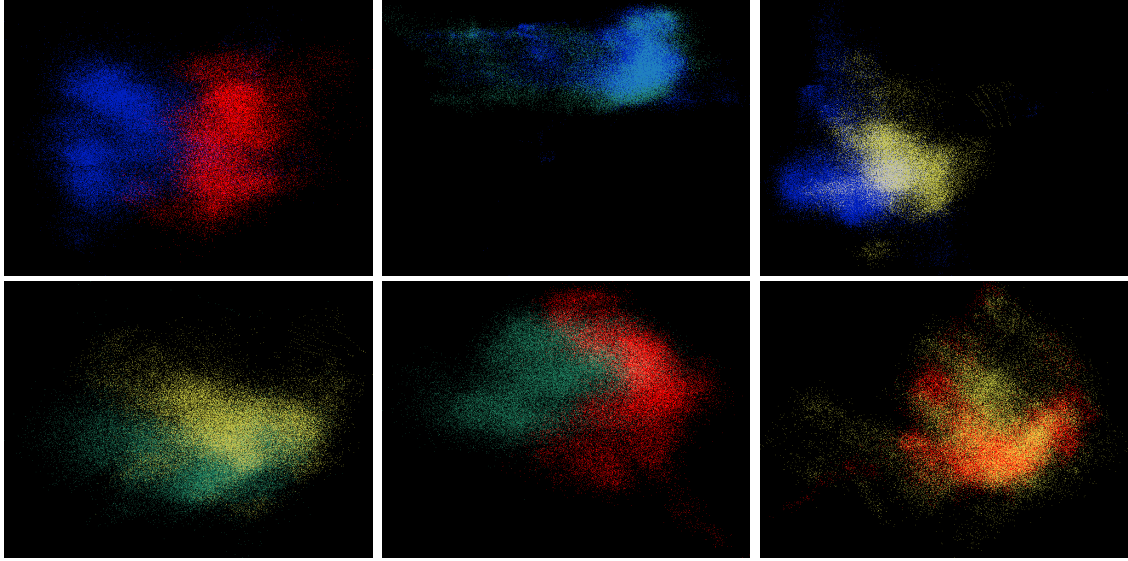


Figure 6.3: Visualisation of features from INbreast sample data. Features displayed for class combinations (rightwards, top to bottom) 1x4, 1x2, 1x3, 2x3, 2x4, 3x4

We can see in Fig. 6.3 that our model distinguishes the different density textures fairly well with the best results being between the most distant classes. This is indeed logical since closer classes have more similar textures.

6.2.4 Breast Density Classification

We classify the mammograms into the different density categories as shown in Fig. 6.4. We first extract the feature vectors for each pixel as described in Sec. 6.2.2 and then for each pixel compute the likelihood for each density class (6.1). The pixel is then assigned the class with highest likelihood. We can see in the example in Fig. 6.5 that the different texture types are reasonably assigned with the dense area clearly marked in red colour.

The whole breast is then classified according to the pixel majority class.

6.2.5 Results

The comparative experimental results were tested on the MIAS database [82] and on the state-of-the-art public digital mammogram INbreast database [86]. We tested the classification of all the possible pairs of classes to see the limits of our method. We also tested the classification of all the classes together. For each tested case we selected 5 random mammograms for each class as training data and classified the rest of the database (excluding training images). The results can be seen in Tabs. 6.1, 6.2. Value at i -th row and j -th column means the number of times a mammogram of class i was classified as class j . The top-left cell of each table section shows which classes have been classified

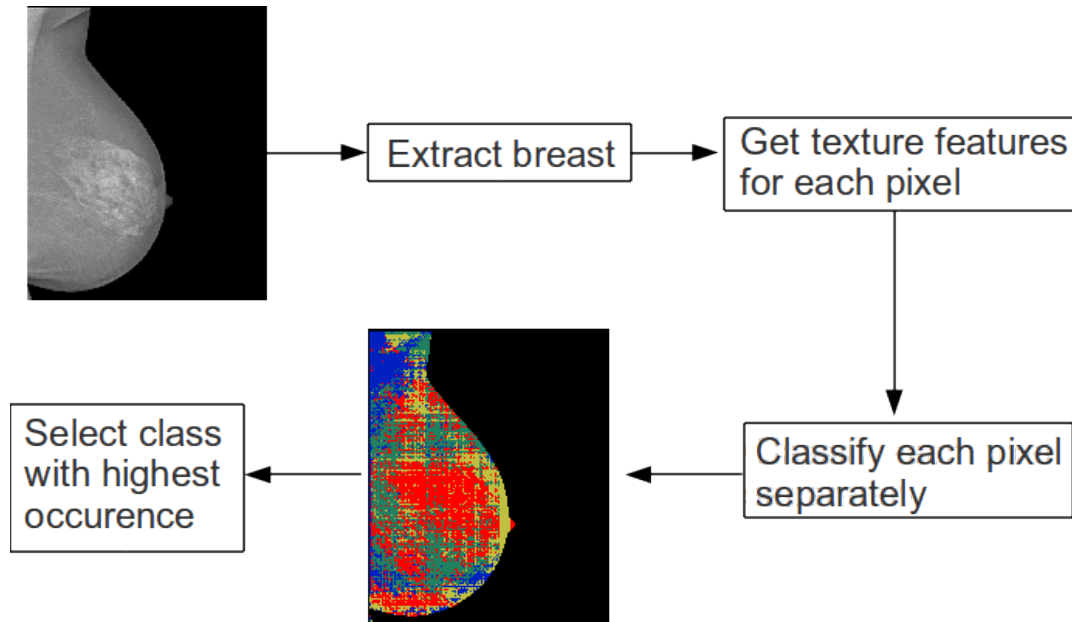


Figure 6.4: Classification flowchart.

against each other. We present the classifications of non-trained classes for illustration of the behaviour of the algorithm on non-trained classes.

The results for the MIAS database seem a little more precise than for the INbreast database. This can be caused by the fact that the MIAS database does not provide the density information according to the ACR BI-RADS standard but rather provides its own method with 3 classes instead of 4.

6.2.6 Comparison with Leading Methods

There are no alternative tissue classification results for the INbreast database, so we compare our results with the state-of-the-art methods applied to the obsolete MIAS data.

Muhimmah and Zwiggelaar [39] obtained slightly better results ($\langle 63; 91 \rangle\%$) sensitivity and precision ($\langle 74; 80 \rangle\%$) for their best multiresolution histogram features-based published method and ($\langle 57; 83 \rangle\%$) sensitivity and precision ($\langle 54; 75 \rangle\%$) for the single resolution variant on the MIAS database. Both methods use the Directed Acyclic Graph - Support Vector Machine (DAG-SVM) classifier. However, the multiresolution method uses fifty times more features than our method and the single resolution method is worse than our presented single resolution method. Mustra et al. [40] has the best published results - ($\langle 75; 87 \rangle\%$) sensitivity and precision ($\langle 74; 91 \rangle\%$) on MIAS to our knowledge. They need fifteen times more features than we do, use a slow kNN classifier, and while we train the classifier on just five images per class, they use the whole database of 321 images (leave-one-out).

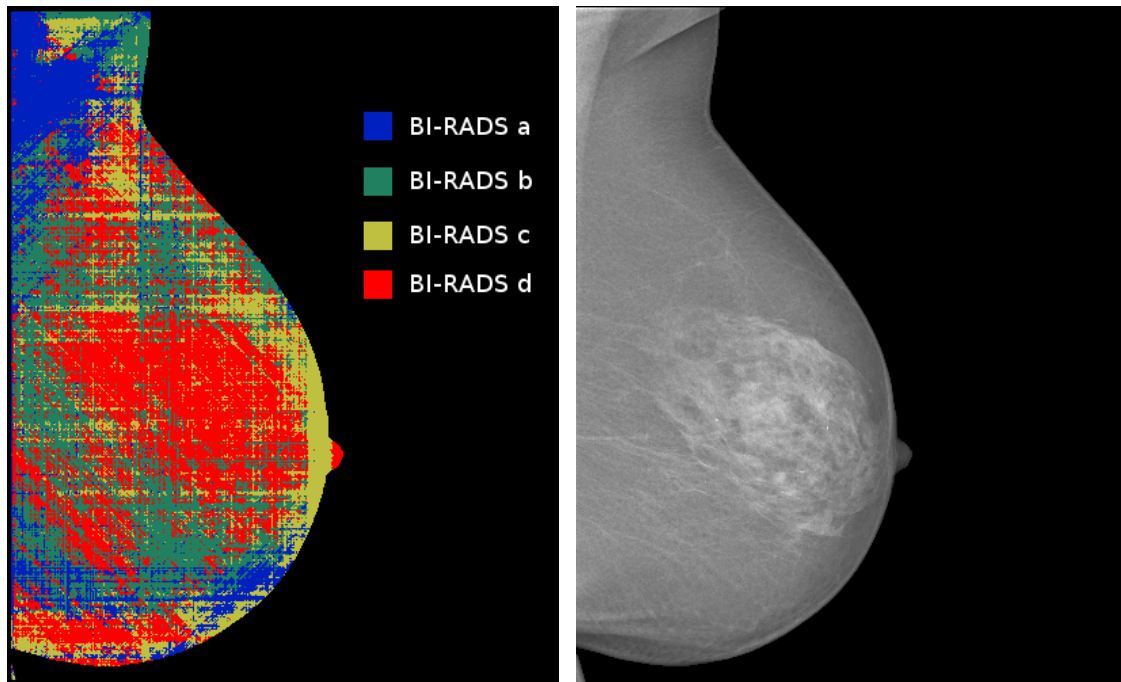


Figure 6.5: Example of pixel classification into different density classes.

6.3 2DCAR Parameter Analysis

6.3.1 Optimizing Neighbourhood

After publishing our classification method in [A.6], we further focused on the analysis of the behaviour of the algorithm based on the various parameters of the 2DCAR model. We did all the testing on the MIAS database from which we randomly selected half the pictures for training and left the rest for testing.

First we tried to find the ideal neighbourhood for the 2DCAR model. We did this using the genetic algorithms in the following way. The genetic code was the set of possible neighbours with genes attaining true/false value based on whether the given neighbour was used or not. Fig. 6.6 shows what the best and worst found neighbourhoods looked like. The red cell means the pixel for which the neighbourhood is computed, black cell means that the neighbour was used while white cell means that the neighbour was not used. The numbers inside the cells are the coordinates of the given neighbours. It was quite surprising that the best and worst neighbourhoods did not differ that much from each other. This is currently ongoing research and will be covered by our future work.

The genetic algorithm had 100 specimen in each generation, keeping 20 best specimen between iterations. Each kept specimen had a 5% chance of dying between generations. The criterion function of the genetic algorithm was the precision with which the given configuration was able to classify the training set. Crossover was performed uniformly

-9 -9	-8 -9	-7 -9	-6 -9	-5 -9	-4 -9	-3 -9	-2 -9	-1 -9	0 -9	-9 -9	-8 -9	-7 -9	-6 -9	-5 -9	-4 -9	-3 -9	-2 -9	-1 -9	0 -9
-9 -8	-8 -8	-7 -8	-6 -8	-5 -8	-4 -8	-3 -8	-2 -8	-1 -8	0 -8	-9 -8	-8 -8	-7 -8	-6 -8	-5 -8	-4 -8	-3 -8	-2 -8	-1 -8	0 -8
-9 -7	-8 -7	-7 -7	-6 -7	-5 -7	-4 -7	-3 -7	-2 -7	-1 -7	0 -7	-9 -7	-8 -7	-7 -7	-6 -7	-5 -7	-4 -7	-3 -7	-2 -7	-1 -7	0 -7
-9 -6	-8 -6	-7 -6	-6 -6	-5 -6	-4 -6	-3 -6	-2 -6	-1 -6	0 -6	-9 -6	-8 -6	-7 -6	-6 -6	-5 -6	-4 -6	-3 -6	-2 -6	-1 -6	0 -6
-9 -5	-8 -5	-7 -5	-6 -5	-5 -5	-4 -5	-3 -5	-2 -5	-1 -5	0 -5	-9 -5	-8 -5	-7 -5	-6 -5	-5 -5	-4 -5	-3 -5	-2 -5	-1 -5	0 -5
-9 -4	-8 -4	-7 -4	-6 -4	-5 -4	-4 -4	-3 -4	-2 -4	-1 -4	0 -4	-9 -4	-8 -4	-7 -4	-6 -4	-5 -4	-4 -4	-3 -4	-2 -4	-1 -4	0 -4
-9 -3	-8 -3	-7 -3	-6 -3	-5 -3	-4 -3	-3 -3	-2 -3	-1 -3	0 -3	-9 -3	-8 -3	-7 -3	-6 -3	-5 -3	-4 -3	-3 -3	-2 -3	-1 -3	0 -3
-9 -2	-8 -2	-7 -2	-6 -2	-5 -2	-4 -2	-3 -2	-2 -2	-1 -2	0 -2	-9 -2	-8 -2	-7 -2	-6 -2	-5 -2	-4 -2	-3 -2	-2 -2	-1 -2	0 -2
-9 -1	-8 -1	-7 -1	-6 -1	-5 -1	-4 -1	-3 -1	-2 -1	-1 -1	0 -1	-9 -1	-8 -1	-7 -1	-6 -1	-5 -1	-4 -1	-3 -1	-2 -1	-1 -1	0 -1
-9 0	-8 0	-7 0	-6 0	-5 0	-4 0	-3 0	-2 0	-1 0	0 0	-9 0	-8 0	-7 0	-6 0	-5 0	-4 0	-3 0	-2 0	-1 0	0 0

Figure 6.6: Best found neighbourhood for the 2DCAR model (left) and worst found neighbourhood (right).

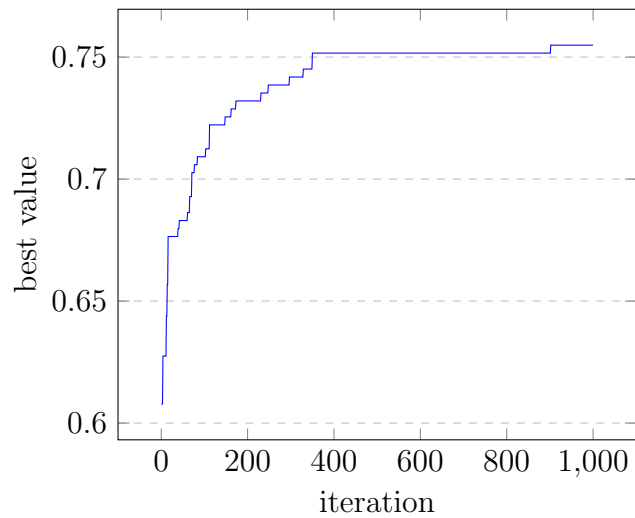


Figure 6.7: The overall best results found by the genetic algorithm during 1000 iterations.

6. BREAST TISSUE DENSITY CLASSIFICATION

1x4	1	2	3	4	Sensitivity
1	132	0	0	4	97%
2	88	0	0	59	0.0%
3	23	0	0	76	0.0%
4	2	0	0	26	92.8%
Precision	98.5%			86.7%	
1x3, 1	128	0	8	0	94.1%
2	81	0	66	0	0.0%
3	15	0	84	0	84.8%
4	4	0	24	0	0.0%
Precision	88.3%		91.3%		
1x2, 1	80	56	0	0	58.8%
2	20	127	0	0	86.4%
3	7	92	0	0	0.0%
4	0	28	0	0	0.0%
Precision	80%	69.4%			
2x4, 1	0	133	0	3	0.0%
2	0	137	0	10	93.2%
3	0	60	0	39	0.0%
4	0	4	0	24	85.7%
Precision		97.2%		70.6%	
2x3, 1	0	132	4	0	0.0%
2	0	122	25	0	83.0 %
3	0	33	66	0	66.7%
4	0	6	22	0	0.0%
Precision		78.7%	72.5%		
3x4, 1	0	0	96	40	0.0%
2	0	0	118	29	0.0 %
3	0	0	89	10	89.9%
4	0	0	14	14	50.0%
Precision			86.4%	58.3%	
1x2x3x4, 1	95	23	18	0	69.9%
2	33	60	49	5	40.8%
3	6	19	58	16	58.6%
4	0	7	3	18	64.3%
Precision	70.9%	55%	45.3%	46.2%	

Table 6.1: INbreast database classification results for all double-class combinations and the complete four BI-RADS tissue classes (rows \sim references, columns \sim interpretation).

1x3	1	2	3	Sensitivity
1	92	0	12	88.5%
2	33	0	70	0.0%
3	5	0	106	95.5%
Precision	94.8%		89.8%	
1x2, 1	72	32	0	69.2%
2	10	93	0	90.3%
3	2	109	0	0.0%
Precision	87.8%	74.4%		
2x3, 1	0	104	0	0.0%
2	0	95	8	92.2%
3	0	57	54	48.6%
Precision		62.5%	87.1%	
1x2x3, 1	89	8	7	85.6%
2	20	57	26	55.3%
3	8	34	69	62.2%
Precision	76.1%	57.6%	67.6%	

Table 6.2: MIAS database all dichotomous and one classification result for all three (fatty, fatty-glandular, dense-glandular) tissue classes (rows \sim references, columns \sim interpretation).

	1	2	3	Sensitivity
1	88	5	7	88.0%
2	13	53	33	53.5%
3	6	11	90	84.1%
Precision	82.2%	76.8%	69.2%	

Table 6.3: Best result's contingency table.

for each possible neighbour, with 50% chance of getting the value of either parent. Fig. 6.7 shows the overall best classification precision during 1000 iterations of the genetic algorithm. We achieved the precision of 75.49% (pessimistic hold-out estimate) which is 8% better than our published result. The contingency table of the best result is shown in Tab. 6.3.

6.3.2 Exponential Forgetting Factor

When we analyzed the results of the genetic algorithm based neighbourhood optimization, we noticed that the results are heavily dependent on the configuration of the 2DCAR model.

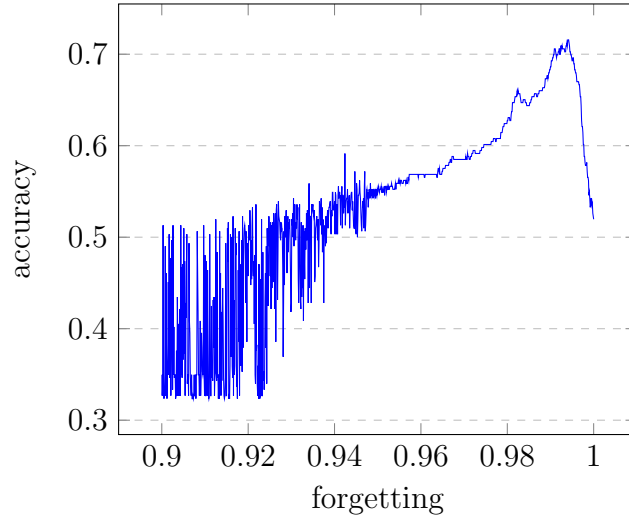


Figure 6.8: The influence of the exponential forgetting factor on the classification result.

The remaining free parameter to be examined was the exponential forgetting factor [9]. We fixed all parameters except for the exponential forgetting factor which we tried for values in range $< 0.9, 1 >$ with step 0.0001. The result is shown Fig. 6.8. We can see that the exponential forgetting factor should have values close to 1 for the model to exhibit stable results with optimum at values 0.994. However, after 0.999 the results fall rapidly. We tried this approach with lots of different random generated neighbourhoods and observed always the same dependency.

6.4 Potts-based Classification Using Extremal Regions

In this section we present our preliminary results in combining the Potts random field with Extremal regions to classify breast density. We first compute the Extremal regions of a mammogram image on its positive image, negative image and gradient image. The Extremal region thresholds increase by 5%, giving us 20 region images for each image type, 60 in total. On the region images, we estimate the β parameter of the Potts random field (for example, see Fig. 6.9). The resulting 60 estimated parameters are then used as feature vector.

We classified the MIAS database using the kNN classifier with $k = 42$. The testing method was leave-one-out. The result (see Tab. 6.4) was comparable with our previously published result [A.6]. We intend to combine both the methods in the future, hopefully resulting in better classification results.

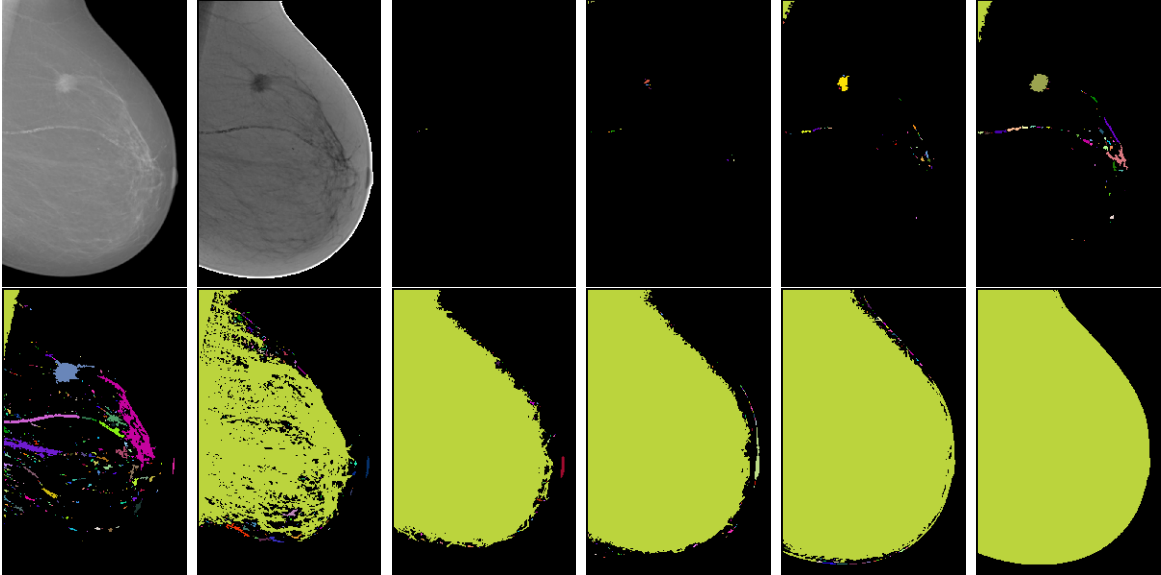


Figure 6.9: Example of extremal regions computed on breast image. Left to right, top to bottom: Original mammogram, its negative and Extremal regions with thresholds increasing by 10%. Estimated Potts field β s of the Extremal regions, successively: 2.672, 2.679, 2.722, 2.727, 3.03, 2.628, 2.523, 2.631, 2.665, 2.479

	1	2	3	Sensitivity
1	68	27	9	65.4%
2	14	57	32	55.3%
3	6	23	82	73.9%
Precision	77.3%	53.3%	66.7%	

Table 6.4: Contingency table of the Potts field Extremal regions based classification.

Mammogram Texture Enhancement

We make the presumption that mammograms can be thought of as textures and therefore modeled using texture models. Indeed, in [35, 36] the authors state that the breast is made of only by 4 types of texture - nodular, linear, homogeneous and radiolucent. When we look at mammograms, we can see that they really do separate into several texture types that look more or less the same on different places of the mammogram. The ROIs can then be thought of as abnormalities in these texture types.

To model the texture that the mammogram comprises of, we have selected the 2DCAR model and its multidirectional generalization we proposed in Sec 4.2.1. This model has analytical solutions to parameter estimation and can be easily used for local texture prediction - that gives us a great way of finding abnormalities using the local predictor error.

We have published several articles on mammogram enhancement [A.2, A.3, A.5] and one journal paper is currently under review [A.8]. In the following sections, we first introduce our unilateral approach (Sec. 7.1), continued by the bilateral comparison method (Sec. 7.2) and concluded by our pseudocolour enhancement method (Sec. 7.3).

7.1 Unilateral Enhancement

The mammographic tissue textures in the form of mono-spectral images are locally modeled by their dedicated independent Gaussian noise-driven autoregressive random field two-dimensional model (2DCAR), because this model has good modeling performance, is very fast and allows analytical treatment (2.2).

The method uses a locally adaptive version of this 2DCAR model, where its recursive statistics are modified by an exponential forgetting factor, i.e., a constant smaller than 1 which is used to weight the older data.

The single-view enhancement method uses fused information from up to eight directional models (Sec. 4.2.1). The enhancement algorithm exploits model statistics (7.1)-(7.3).

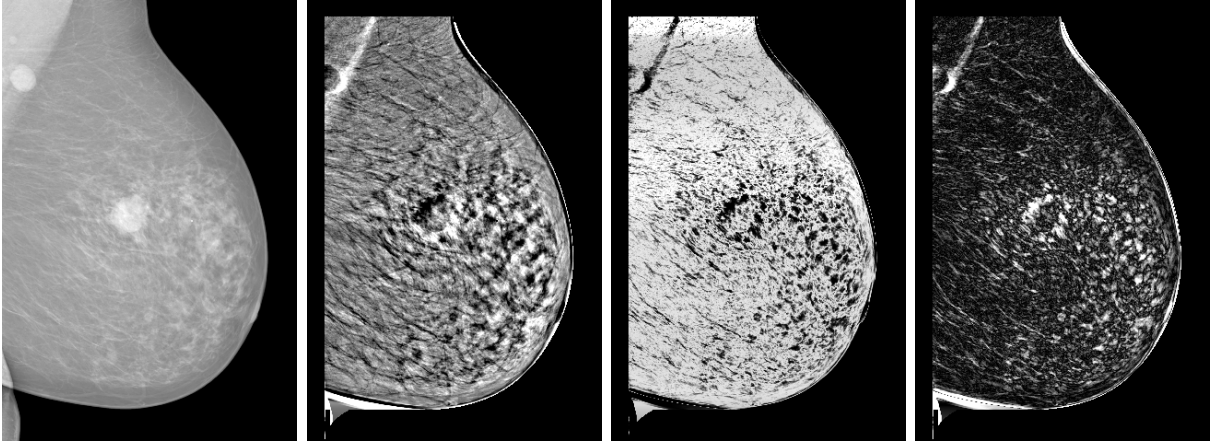


Figure 7.1: Single-view cancerous mammogram enhancement. Left to right: ground truth, prediction error based enhancement (Y_r^{enh}), probability based enhancement (Y_r^{enh2}) and absolute prediction error based enhancement (Y_r^{enh3}).

$$Y_r^{enh} = \sum_{\forall \phi \in \bar{\Phi}} (Y_{r+1} - \hat{\gamma}_{r-1} X_r) , \quad (7.1)$$

$$Y_r^{enh2} = \sum_{\forall \phi \in \bar{\Phi}} p(Y_r | Y^{(r-1)}, \hat{\gamma}_{r-1}) , \quad (7.2)$$

$$Y_r^{enh3} = \sum_{\forall \phi \in \bar{\Phi}} |Y_{r+1} - \hat{\gamma}_{r-1} X_r| , \quad (7.3)$$

where $\bar{\Phi}$ is the set of used directions. This method provides three different enhancement outputs (7.1)-(7.3) targeting different types of mammographic tissue. All the enhanced values are normalized into the 0 – 255 range. An example of the results of this method can be found in Fig. 7.1. We can see how the various movement directions ϕ influence the result in Fig. 7.3. The dependency of the results on the exponential forgetting factor can be seen in Fig. 7.2.

7.2 Bilateral and Temporal Enhancement

Bilateral mammograms exhibit a large degree of similarity. Indeed even the radiologists visually compare two images of the same view type (either CC or MLO) to find irregularities. We present two methods of bilateral comparison. Note that bilateral mammogram comparison can be used usually without any changes also to analyze temporal mammogram sequences.

First we introduce the nonrigid approach which is spatially independent, working only by searching for best fitting local window in the corresponding view to show that even such

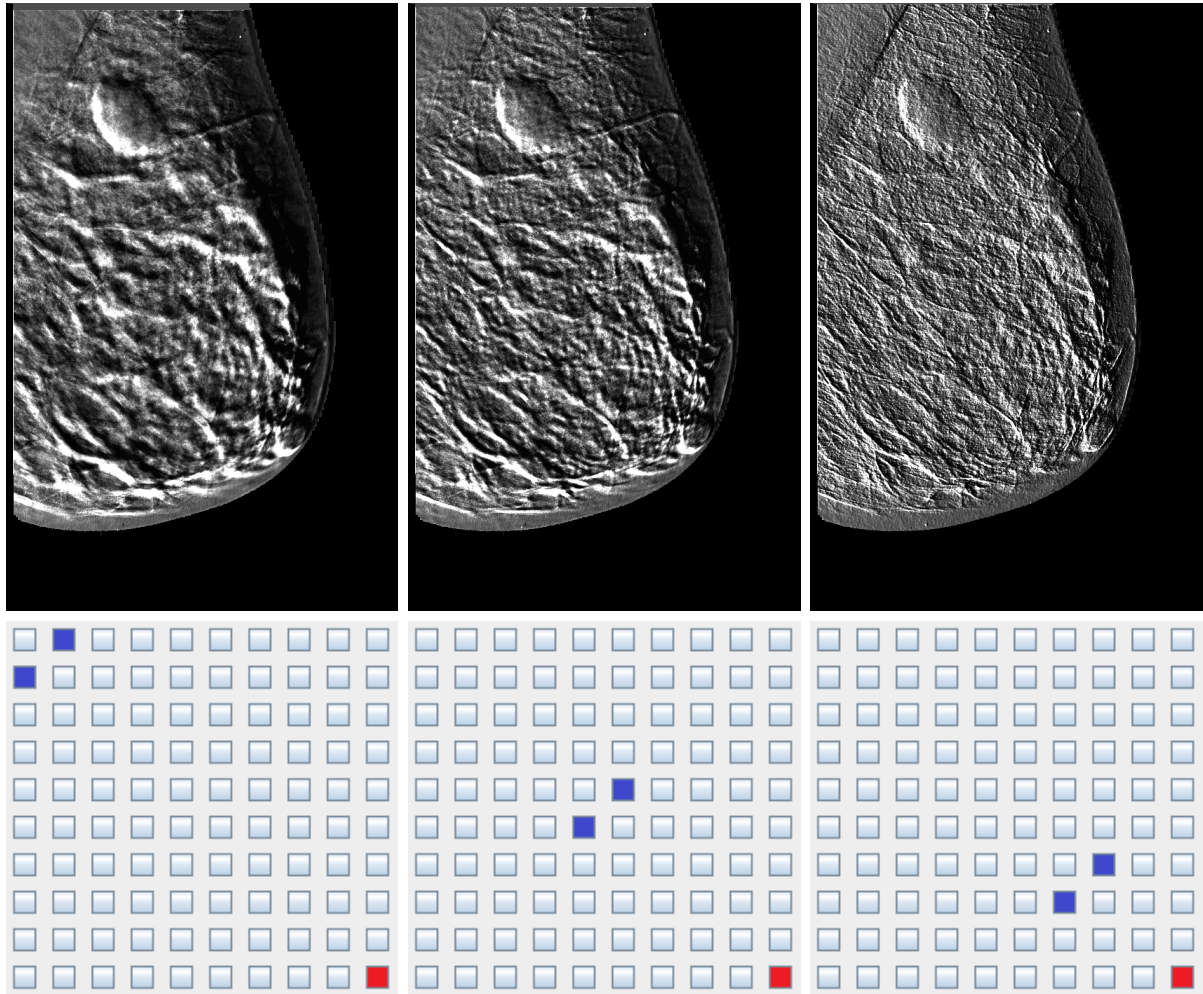


Figure 7.2: Single-view MLO mammogram enhancement using different functional neighbourhoods consecutively rightwards - 9, 5, and 3 pixel neighbourhood distance from the enhanced pixel (blue pixels - bottom row).

a trivial method can have some significance and thus indicate that more intricate methods should work.

The second method starts by registering the bilateral views and assumes that local textural features of the two images should be corresponding with each other. This way we estimate the parameters of a 2DCAR MRF model and apply them to the registered reference image.

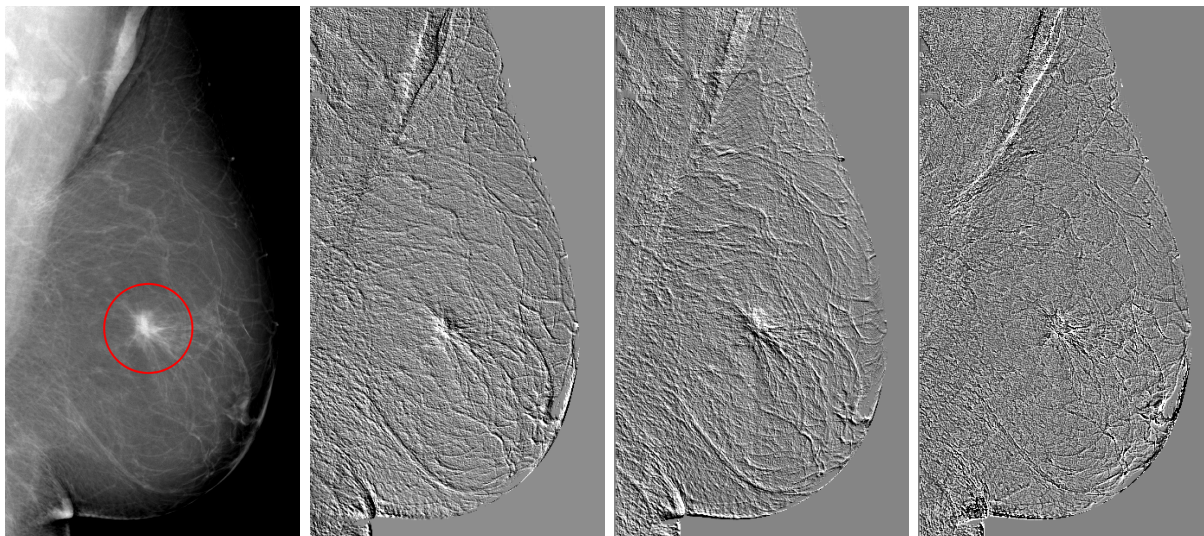


Figure 7.3: Single-view cancerous mammogram enhancement, ground truth and single rightwards model - upper row, single downward model and omnidirectional model combination - bottom.

7.2.1 Bilateral Analysis - Nonrigid Approach

This approach utilizes the idea that since carcinomas appear in the mammograms as parts which do not suit into the image of the breast, using an image of a healthy breast to build up an image of a breast with a carcinoma should result in the later differing from the original image noticeably in the parts where the carcinoma is. This would be caused by the fact that a healthy breast does not contain tissue similar to a carcinoma.

The method works as follows: Pick a window size (for usual mammogram resolution of our used experimental databases, 8-40 pixels usually work best) and trace the source mammogram with it. For each window find a most similar window in the corresponding mammogram. Our experiments show that in order to not use all possible search windows in the reference mammogram, about 1000 randomly picked windows suffice. The similarity measure can be e.g. euclidean distance, correlation, etc. After reconstructing the given mammogram from the reference, we make a difference image based on the selected distance measure and threshold the result to not take into account too similar parts. Higher values therefore represent abnormalities.

This way we can iterate over different window sizes and sum up the results (or rather consider each run with a different window size as a separate classifier). A sample result is shown in Fig. 7.4. The breast contains a cancer in the upper part of the image and a benign lymphatic node (marked with a blue circle).

In the first row, the left image shows the original mammogram with marked ground truth, the middle one shows an example of reconstruction with window size 8px, the right image shows an example of reconstruction with window size 28px.

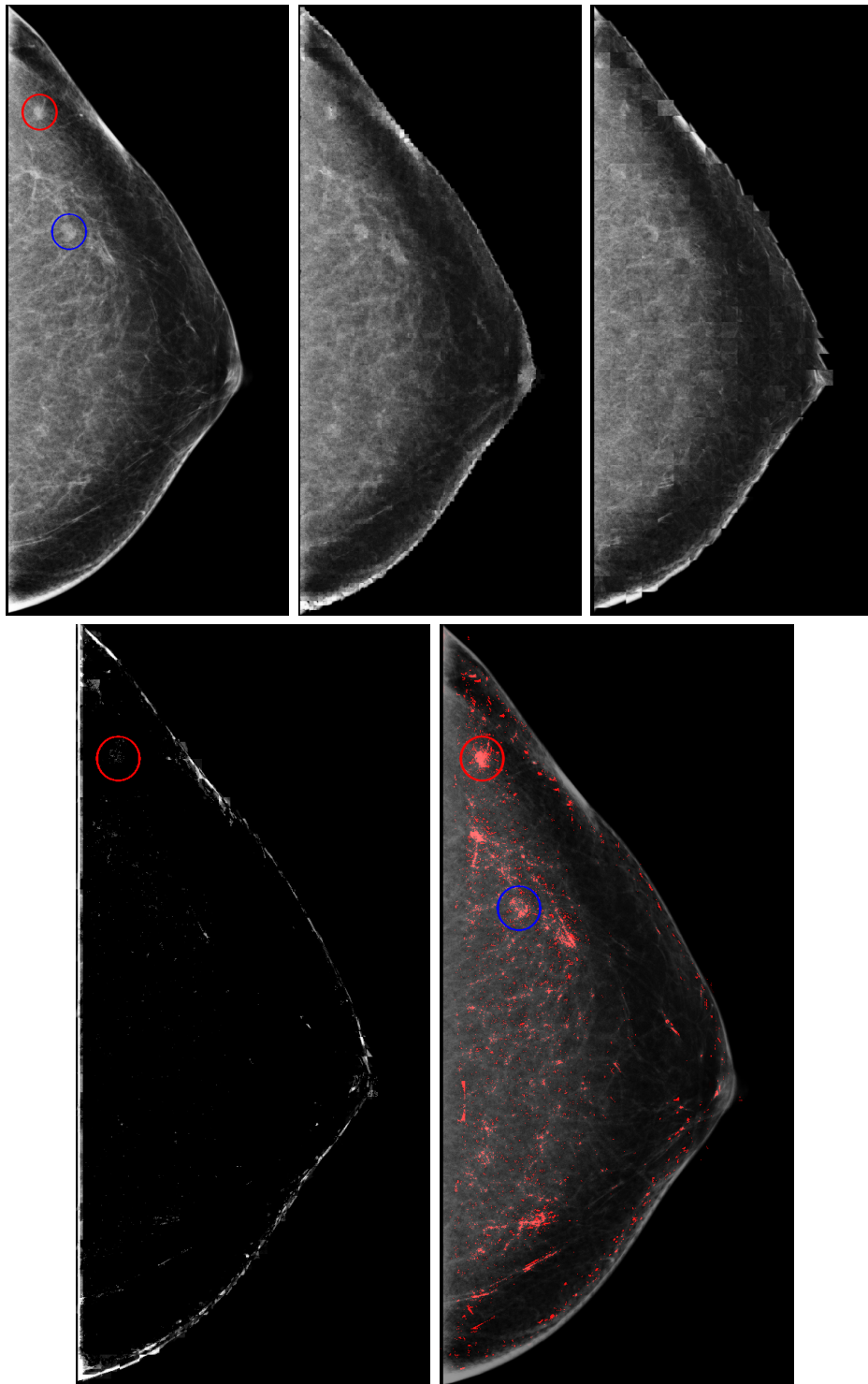


Figure 7.4: Mammogram analysis - nonrigid approach.

In the second row the left image shows an example of the difference image for window size 28px, the right image is the final result of the method with summed differences from window sizes 4,8,12,...40.

We can see that the nonrigid method could find all these ROIs and mark them with red dots. There are many false positives. The greatest false positive regions visible in the upper part of the mammogram are caused by the complexity of the structures which attract the focus of this method.

In this method we presume the mammogram to be built by a limited number of different texture types (about 5-8 at most) which have little spatial variances among the same texture type. Therefore in this method we do not have to perform any registration at all - the best fitting windows are selected from the whole image.

A problem of this method is, that the images differ a lot at the breast boundaries. Therefore, for the result to not contain too many false positives, the differences near the breast contour are masked away. This can result in not noticing a cancer near the breast boundary.

7.2.2 Texture Model Based Bilateral Comparison

The following method extends the idea presented in the previous section. We presume that left and right breasts are architecturally symmetrical. This presumption is indeed reasonable, since radiologists frequently compare bilateral mammograms to find asymmetrical parts, which could indicate a developing cancer. The architectural symmetry, however, does not denote pixel-wise similarity of the two images.

The novelty of the presented method is that whereas other alternative methods usually use simple pixel difference or trivial statistics like cross-correlation to compare the bilateral images, we use the mammograms of one breast as a learning sample for the 2DCAR breast texture model [8, 89] and then try to analyze the other mammogram based on this acquired information. Using the 2DCAR model for bilateral comparison, we achieve a result which is robust to inaccurate registration, very fast, and which gives improved enhancement results than just a single-view analysis even using similar local texture modeling.

The texture based symmetry detection neither needs to assume the pixel-wise correspondence of the both breast images, nor their ideal sub-pixel registration inside the breast area.

The method can be divided into three separate steps: mammogram registration, model parameters estimation, cross-prediction and cross-difference statistics evaluation.

7.2.2.1 Mammogram Registration

The registration process is described for mammographic MLO views (medio-lateral oblique), but it can be easily adapted also for CC views (cranio-caudal). Since we compare the images based on textural features rather than pixel-wise, we do not require as precise registration as other methods, and can use simple affine transformation based registration.

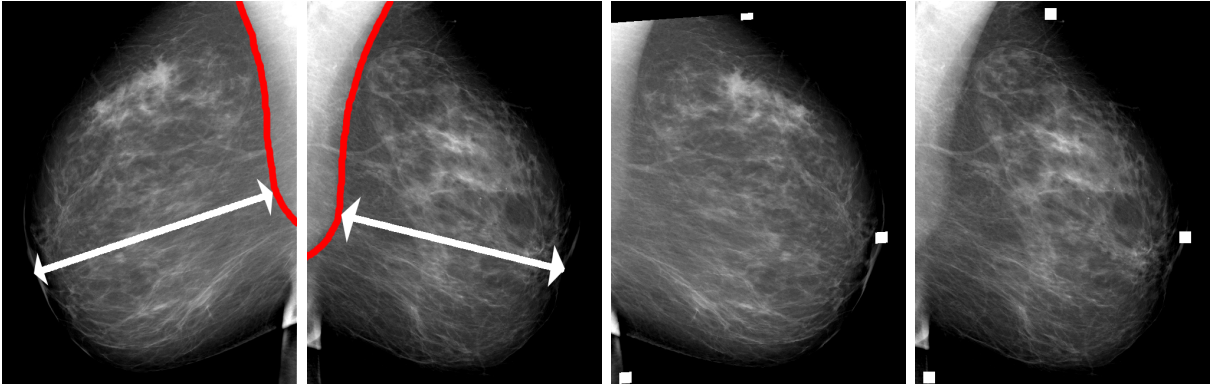


Figure 7.5: Registered mammograms with visible reference points.

Three reference points are needed for the affine transformation. We chose the nipple and one point above and one below it which are closest to the pectoral muscle.

The nipple is located using the heuristic method described in [56]. It works on the idea of the nipple being a point on the skin-line of the breast which is the most distant to the line of the pectoral muscle. After the candidates for nipple reference points have been found in both the mammograms, the position of the reference point can still slightly differ in both images. Therefore, we adjust their position by searching the neighborhood on the skin line of the breast for the most correlated window.

The remaining reference point candidates have to be further adjusted as well. Since the bilateral mammograms usually do not cover the same area of the breast, some anatomical parts of the breast can be seen only in one of the images and therefore the reference points would not match. To make up for this problem, we measure the distance of the points to the nipple, weighted by the nipples distance to the pectoral muscle. The weighting compensates for differences of positioning the breast in the mammogram which could result in one image displaying the breast bigger than the other. We then adjust the corresponding reference points, so that they are on the skin line with the most similar weighted distance to the nipple possible.

Having the reference points, the affine transformation is performed. Fig. 7.5 left to right shows the images of right and left breast with marked line of the pectoral muscle (coloured in red) and the distance from the pectoral muscle to the nipple, the registered breasts with the reference points painted as white squares with the right breast (last but one on the right) transformed to match the left breast.

7.2.2.2 Data Fusion

When the bilateral mammograms are registered, their mutual comparison is possible. As we have stated in Chapter 2, most methods simply make a pixel-wise difference. Using texture models for difference instead of just the gray-level pixel values brings a bigger robustness to inaccuracies during the registration.

7. MAMMOGRAM TEXTURE ENHANCEMENT

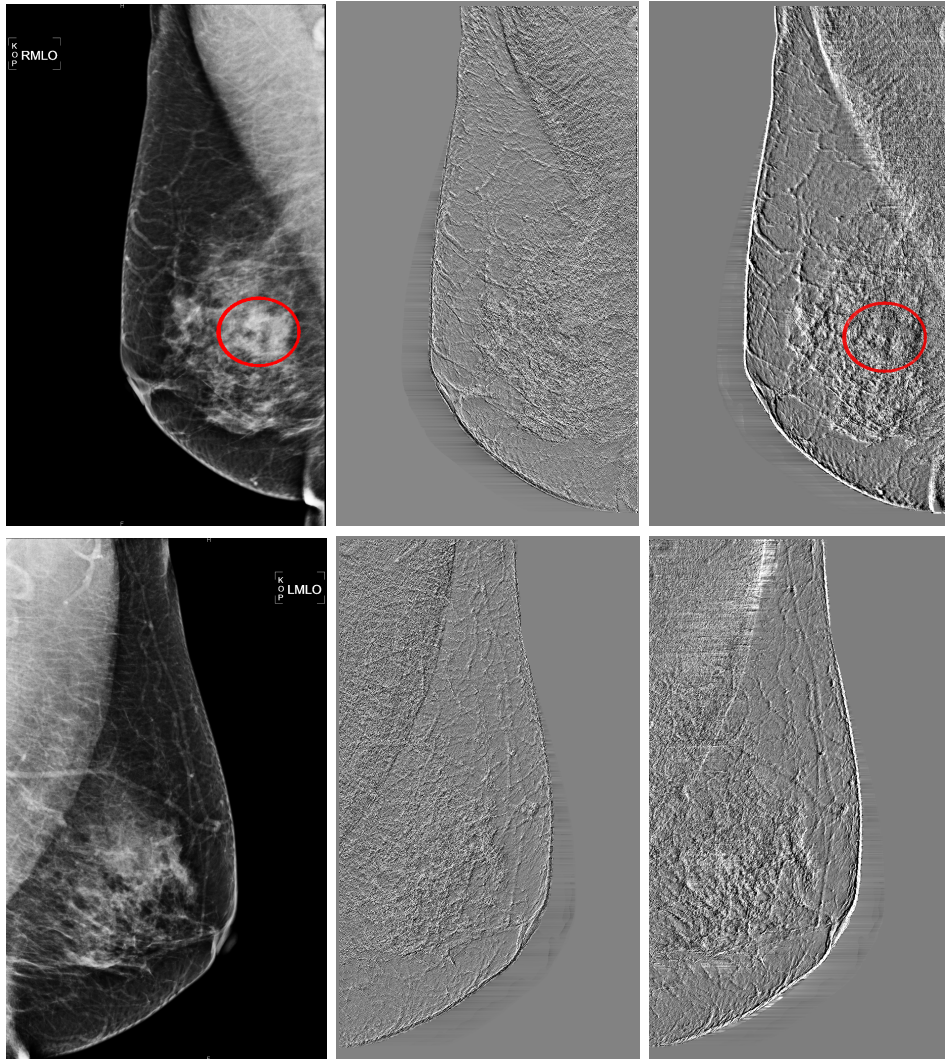


Figure 7.6: Mammogram with cancer in the right breast - original image with ground truth, CAR prediction error, CAR cross-prediction error



Figure 7.7: Mammogram from Fig. 7.6 - cross difference with highlighted cancer

For this purpose we devised the 2D Cross-CAR model. It is derived from the standard 2DCAR model (2.2). It is based on estimating the 2DCAR parameters for one breast image while applying them to the other one. Mathematically speaking we could write the 2D Cross-CAR model as follows:

$$Y_{R/L,r} = \gamma_{L/R} X_{R/L,r} + e_r$$

where R/L means the random field belonging to the mammogram of the right/left breast respectively. Notice that the $\gamma_{L/R}$ has the left/right mark swapped. The local cross-predictor can be then defined as

$$E_{cross}\{Y_{R/L,r}|Y_{R/L}^{(r-1)}\} = \gamma_{L/R,r-1} X_{R/L,r}$$

The local cross-predictor error is

$$Err_{crossR/L,r} = E_{cross}\{Y_{R/L,r}|Y_{R/L}^{(r-1)}\} - Y_{R/L,r} = \gamma_{L/R,r-1} X_{R/L,r} - Y_{R/L,r}$$

Furthermore, we add the cross-prediction difference, which works by locally predicting the left breast using right breast parameters and then subtracting it from the image of right breast locally predicted by the left breast parameters.

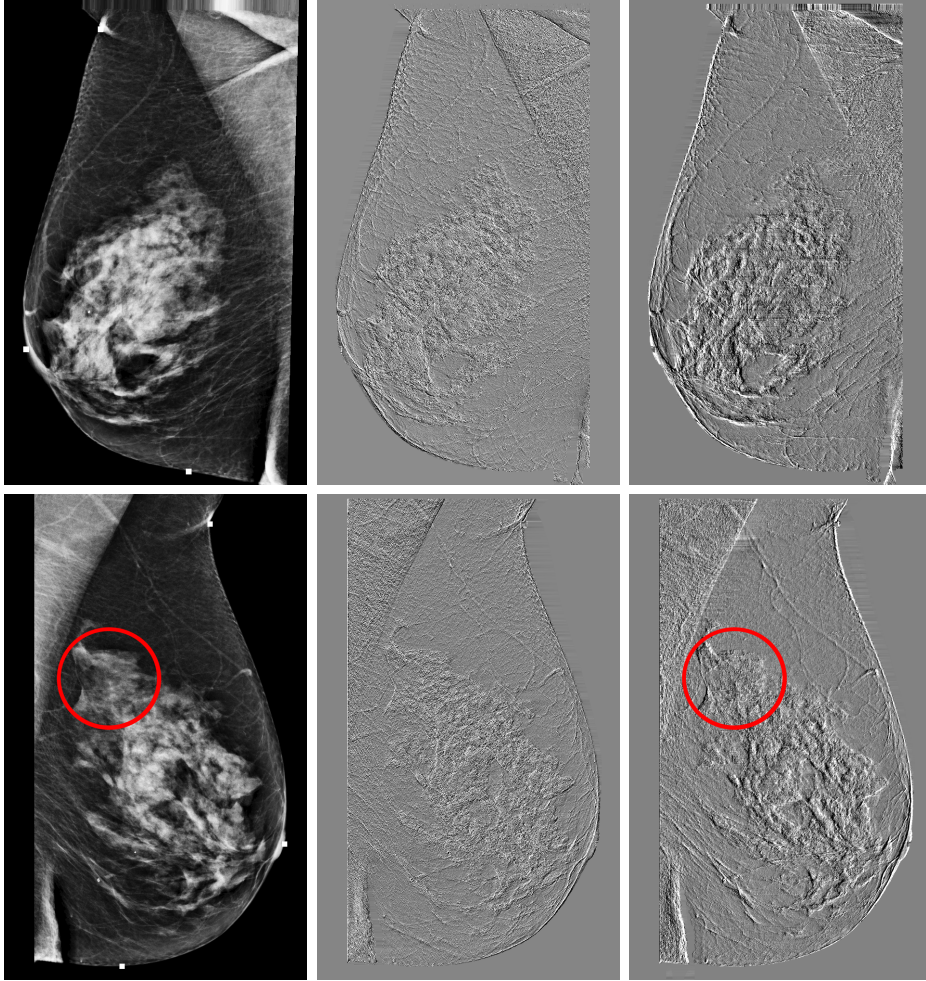


Figure 7.8: Mammogram with cancer in the right breast - original image with ground truth, CAR prediction error, CAR cross-prediction error

$$CrossDiff = E_{cross}\{Y_{R,r}|Y_R^{(r-1)}\} - E_{cross}\{Y_{L,r}|Y_L^{(r-1)}\} = \gamma_{L,r-1}X_{R,r} - \gamma_{R,r-1}X_{L,r}$$

7.2.2.3 Results

Fig. 7.6 shows the registered mammograms of left and right breast, prediction error of the 2DCAR model and the cross-prediction error obtained using the 2D Cross-CAR model. These results are then completed by the cross-prediction difference shown in Fig. 7.7. We can see that the cross-prediction error leads to much more contrasting results than using a simple prediction error of the 2DCAR. We can see a highlighted area in the middle of the left image which is the present cancer. The cross-difference clearly separates the cancer as an abnormality which does not exist in the other breast.

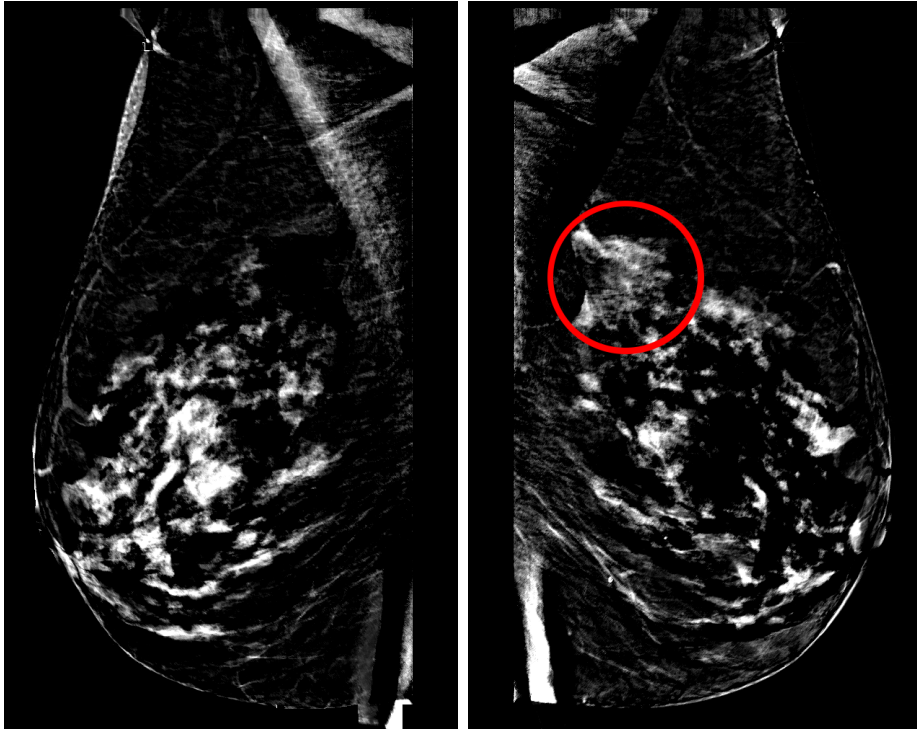


Figure 7.9: Mammogram from Fig. 7.8 - cross difference with highlighted cancer

In Fig. 7.8 we can see another example of the results of bilateral information fusion. This time there is a lesion in the left breast which does not visually differ from the surrounding texture. However, we can see in the cross-prediction difference (Fig. 7.9 that the area clearly protrudes. There are many false positive highlights in this example which we pointed out also in the previous example. We believe that they could be eliminated by incorporating the information from CC-MLO registration, which we intend to do in the future research. The important thing now is that the asymmetry is caught and clearly visible in the difference image, which has been our main aim.

7.2.3 Discussion

The results confirm that our proposed method is capable of highlighting abnormal differences in bilateral mammograms. There is a large rate of false positive highlights which is due to the differences between the breasts and possibly a too finely grained setting of the comparison model. However, the results can still be used as a guide during inspection of the breast both done by humans and computers and there are many possibilities of reducing the false positive rate which we aim at researching in our future work.

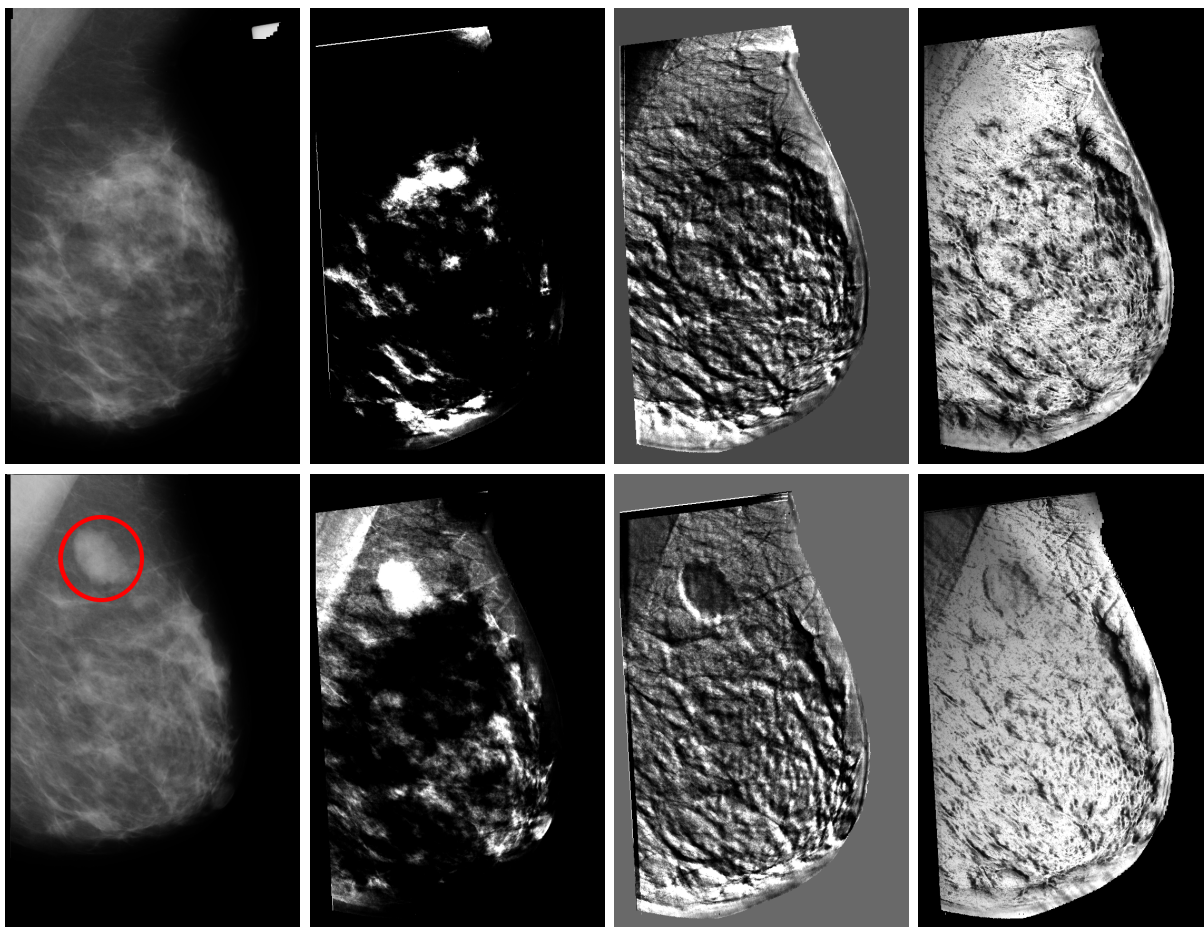


Figure 7.10: Multiple-view medio-lateral mammogram enhancement consecutively right-wards - ground truth, pixel difference between registered LMLO and RMLO, cross-predicted gradient, and cross-prediction probability density. The upper row contains LMLO, bottom row RMLO.

7.3 Pseudo Color Enhancement

The mammogram enhancement is based on efficient fusion of several hundred textural statistics, each describing different aspect of the mammogram texture, their subsequent decorrelation, and visualization of a weighted combination of the three most informative transformed features and the original X-ray mammogram. Fig. 7.11 shows the flowchart of the method, which is described in more detail in the following text.

To compute the mammogram enhancement features, the following statistics of the directional 2DCAR model (Sec. 4.2.1) are evaluated for each pixel in the original mammogram measurements for all directions, as well as in the smoothed variants obtained by median filters with window sizes 2, 3, 5, 8, and 10px (the filter sizes were selected based on the

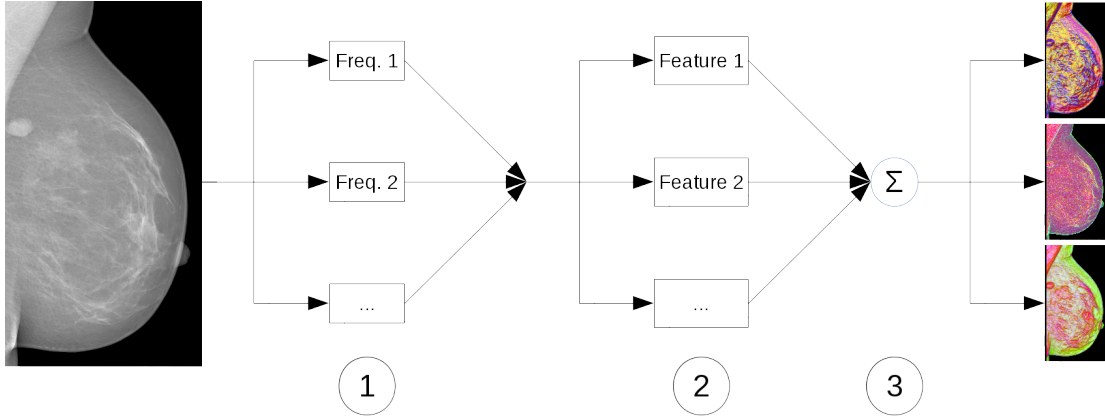


Figure 7.11: The enhancement method's flowchart.

resolution of the input mammograms):

Prediction error – the prediction error can be computed as

$$Err_{pred}^r = E \{Y_r | Y^{(r-1)}\} - Y_r . \quad (7.4)$$

This statistic is sensitive to smaller to medium-sized texture abnormalities, such as lymph nodes.

Absolute value of the prediction error – the absolute value of the previously defined Prediction Error

$$|Err_{pred}^r| = |E \{Y_r | Y^{(r-1)}\} - Y_r| . \quad (7.5)$$

This statistic is sensitive to small texture abnormalities such as lymph nodes, necrotic calcification, and larger benign calcifications.

Innovation error – this statistic combines the prediction error with the gradient:

$$Err_{in}^r = E \{Y_{r-1} | Y^{(r-2)}\} - Y_r . \quad (7.6)$$

The innovation error highlights very small texture abnormalities with sharp edges.

Absolute value of the innovation error – the absolute value of the previously defined Innovation Error

$$|Err_{in}^r| = |E \{Y_{r-1} | Y^{(r-2)}\} - Y_r| . \quad (7.7)$$

This statistic is sensitive to very small texture abnormalities, such as microcalcifications.

Prediction probability – equation (2.3). This statistic is sensitive to medium-sized and larger texture abnormalities, such as lesions and larger lymph nodes.

This way we get a number of new images corresponding to the original mammogram but emphasizing different texture features of the image. Because the 2DCAR model is directionally dependent, each analysis is also performed separately for each of the eight different basic directions ϕ .

The resulting model statistics (2.3) and (7.4) through (7.7) are stored in 240 planes (five different statistics computed on the original and five filtered images for each direction ϕ) with the same dimensions as the original image. These 240 computed features have various and spatially dependent mutual correlations. The Karhunen-Loeve transform is then performed on these planes in order to obtain the most informative transformed three components (99% of the overall eigenvalues), which are then assigned respectively to the red, green and blue color channels of the resulting enhanced image. The latter thus consists of the original X-ray measurement and a linear combination of the computed textural statistics. Different partial results are susceptible to different-sized abnormalities, in particular the prediction error components are better for enhancement of smaller findings, such as microcalcifications. The analysis based on prediction probability is, on the other hand, more susceptible to larger abnormalities, such as lesions and masses. Therefore, we split the results of our method into three different outputs:

1. Based purely on prediction probability (7.8) – these results tend to be smoother and work very well on larger areas, e.g., in Fig. 7.13–top row, second image.
2. Based purely on prediction errors (7.9) – good enhancement of smaller abnormalities such as microcalcifications , e.g., in Fig. 7.15–top row, third image.
3. All aspects combined (7.10) – joins the advantages of both of the previous methods, but does not have such good contrast, e.g., in Fig. 7.14–top row, fourth image.

$$\mathbb{Y}_r^b = T_b \left(p(Y_r | Y^{(r-1)}), \dots \right)^T, \quad (7.8)$$

$$\mathbb{Y}_r^s = T_s \left(Err_{pred}^r, |Err_{pred}^r|, Err_{in}^r, |Err_{in}^r|, \dots \right)^T, \quad (7.9)$$

$$\mathbb{Y}_r^m = T_m \left(Err_{pred}^r, |Err_{pred}^r|, Err_{in}^r, |Err_{in}^r|, p(Y_r | Y^{(r-1)}), \dots \right)^T, \quad (7.10)$$

where T are $3 \times \{48, 192, 240\}$ transformation matrices. Matrix rows are eigenvectors corresponding to the three largest eigenvalues from the actual data spaces.

Finally, the enhanced mammograms are optionally combined with the original image to enable the radiologist to perceive both the enhancement and the original structure of

the breast and customize the ratio:

$$\mathbb{Y}_r^{enh} = (1 - c) Y_r \begin{pmatrix} 1 \\ 1 \\ 1 \end{pmatrix} + c \mathbb{Y}_r ,$$

where parameter c depends on the radiologist's personal preference:

$$c = \begin{cases} 0.15 & \textit{light} \\ 0.3 & \textit{medium} \\ 0.6 & \textit{heavy} \\ 1.0 & \textit{full} . \end{cases}$$

7.3.1 Comparison with alternative methods

For comparison, we have implemented four state-of-the-art methods for mammogram image enhancement [41, 53, 54, 55]. These methods enhance mammograms in the grayscale format. We are not aware of any other mammogram enhancement method producing results in color.

7.3.2 Contrast measures

To evaluate our results, we have implemented three different contrast measures already used in the literature. The local contrast is computed using a slightly modified Second-derivative-like measure of enhancement (SDME) proposed by Panetta [54], Border contrast by Erdem et al. [80] and the Weighted-level framework with Retinal-like subsampling contrast (Wlf(Rsc)) proposed by Simone et al. [78]. Furthermore, we have evaluated the contrasts with our proposed contrast measure SRC (8.4).

7.3.3 Numerical contrast results

We present the mean results of the individual contrast measures applied to all the images in the INbreast database in Tab. 7.1. The contrast measures were computed on images subsampled to 1024px height, keeping aspect ratio, and with region of interest overlapping at 20px to cover the context of the computed ROI. The SDME and SRC contrast measures are computed on grayscale images, whereas the border contrast and Wlf(Rsc) are computed in the CIELAB color space. Furthermore, we distinguish between the contrasts computed for different types of ROIs: masses, calcifications and all ROIs together. The best results for each set are printed in boldface, and our presented methods' outputs in italics.

7.3.4 Numerical Evaluation

The four contrast measures exhibit different sensitivities, depending on the types of information measured. The most consistent results can be seen in the Wlf(Rsc) contrast,

Method	Wlf(Rsc)	SDME	Border	SRC
Masses				
Bhateja [55]	0.96	0.99	2.84	0.25
<i>Combined</i> (7.10)	1.02	1.00	7.96	0.29
Original	0.94	0.99	1.29	0.18
Panetta [54]	0.94	0.95	1.89	0.22
<i>Prediction errors</i> (7.9)	0.88	1.01	7.53	0.18
<i>Prediction probabilities</i> (7.8)	1.65	0.98	10.8	0.27
Tang [41]	0.76	1.00	2.35	0.22
Wang [53]	1.02	0.82	6.26	0.47
Calcifications				
Bhateja	0.98	0.98	2.90	0.14
<i>Combined</i>	1.79	1.00	7.76	0.16
Original	0.97	0.99	1.35	0.10
Panetta	0.98	0.97	2.20	0.11
<i>Prediction errors</i>	1.72	1.00	7.49	0.13
<i>Prediction probabilities</i>	1.05	0.99	10.8	0.15
Tang	0.82	0.99	2.16	0.15
Wang	1.03	0.90	6.39	0.25
All ROIs together				
Bhateja	0.97	0.99	2.87	0.16
<i>Combined</i>	1.78	1.00	7.78	0.19
Original	0.97	0.99	1.33	0.12
Panetta	0.97	0.96	2.13	0.14
<i>Prediction errors</i>	1.64	1.00	7.42	0.14
<i>Prediction probabilities</i>	1.27	0.99	10.7	0.17
Tang	0.81	0.99	2.15	0.17
Wang	1.02	0.88	6.26	0.30

Table 7.1: Enhancements' contrast comparison.

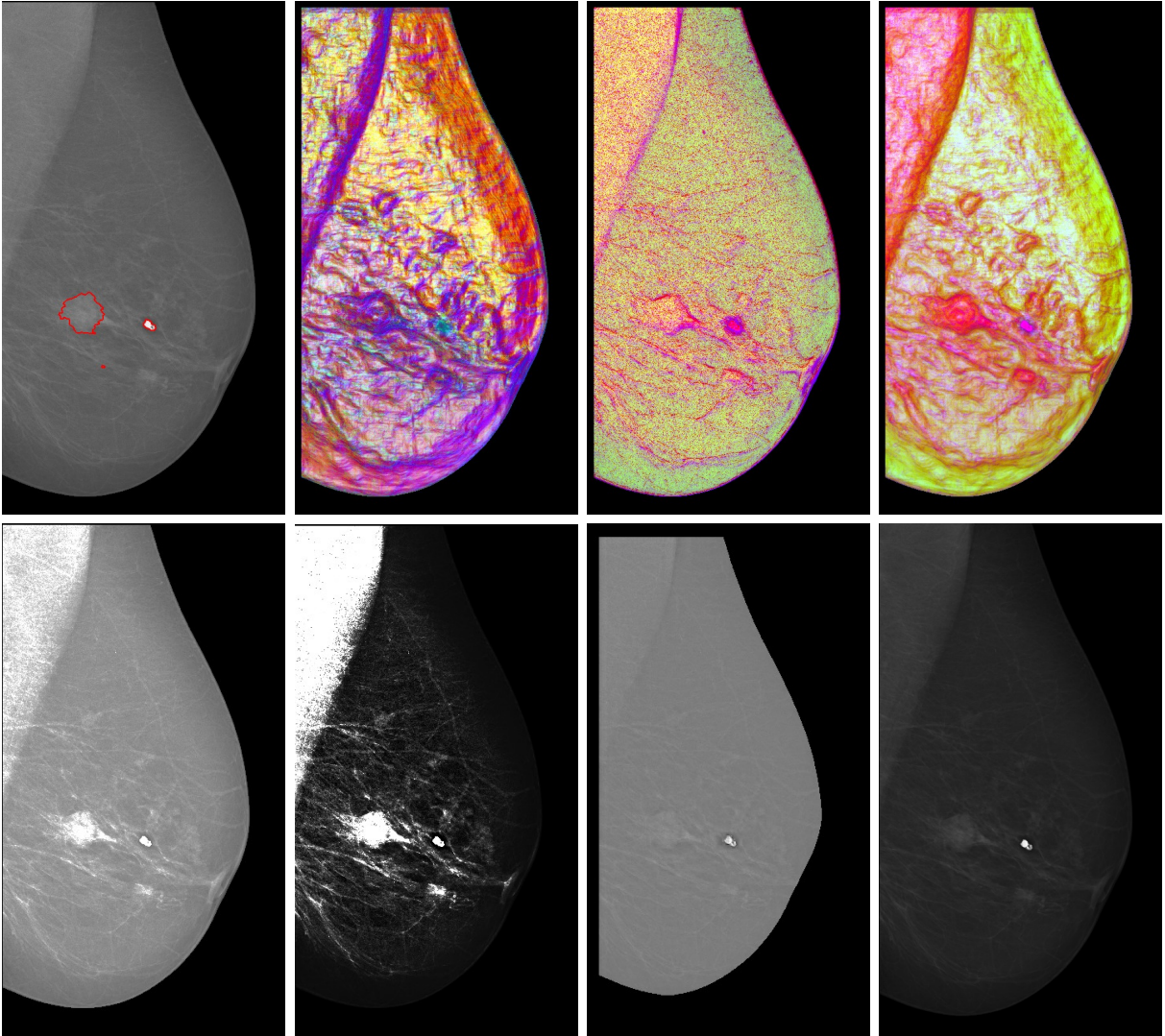


Figure 7.12: Enhanced mammogram example with a lesion and a big calcification. Top row from left to right: original with ground truth, enhancement based on prediction probabilities, enhancement based on prediction errors, and combined enhancement. Bottom row from left to right: comparison methods by [54], [53], [41] and [55].

which confirms our assumption that the prediction-probability-based enhancement is more suitable for enhancing masses while the prediction-error and combined methods are more suitable for calcifications. The combined method is more sensitive to lesions than the prediction-error-based method. Since calcifications cover most of the ROIs taken from the INbreast database, the overall results (bottom part of Tab 7.1) are more biased toward the calcification-focused approaches.

The contrast criteria suggest that our method significantly outperforms the compared

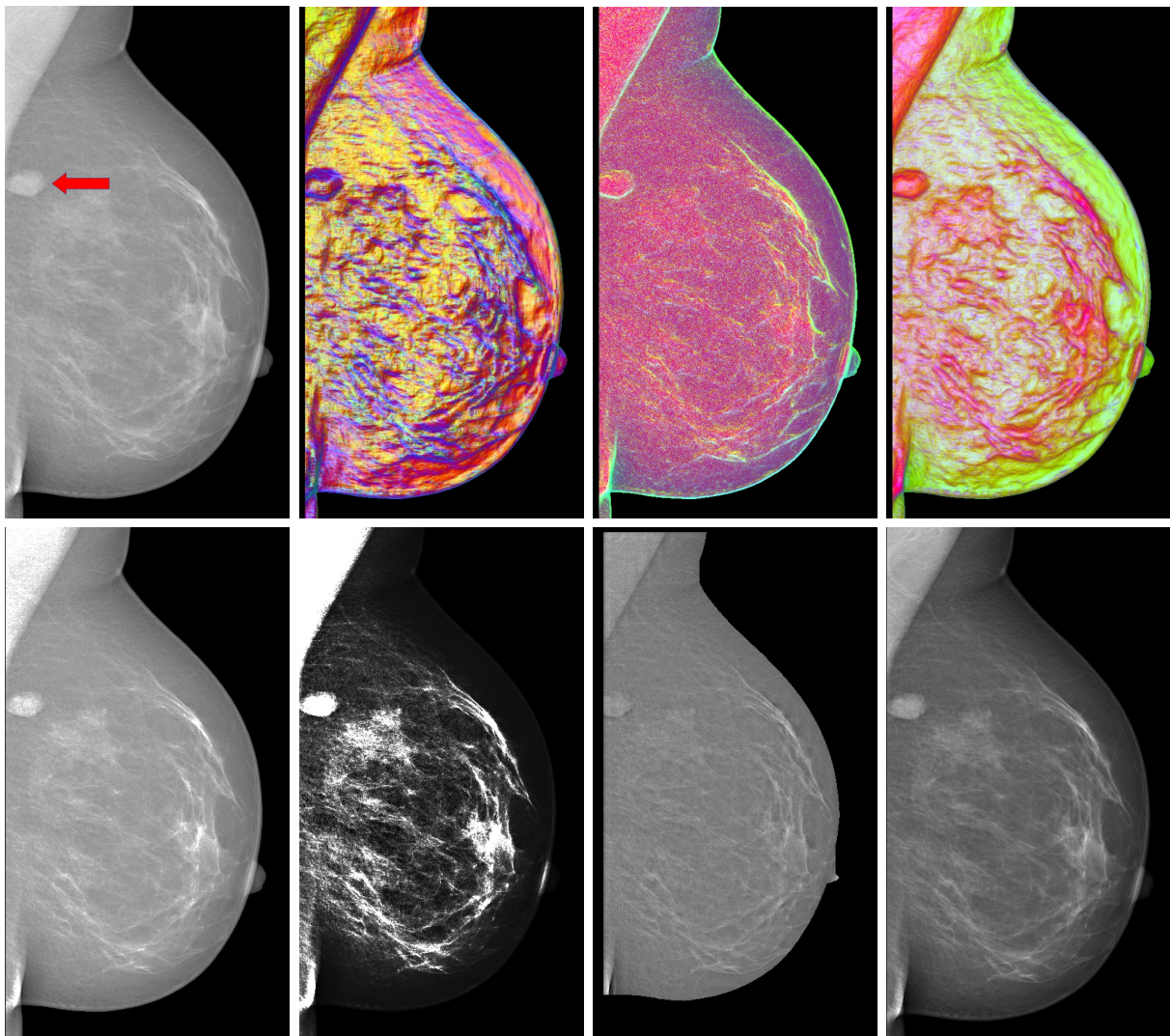


Figure 7.13: Examples of mammogram enhancement. Top row from left to right: original with ground truth, enhancement based on prediction probabilities, enhancement based on prediction errors, and combined enhancement. Bottom row from left to right: comparison methods by [54], [53], [41] and [55].

alternatives even in grayscale images. The alternative methods may occasionally exhibit contrast values even lower than those encountered in the original images. Our SRC contrast measure is the only contrast measure giving better values to an alternative enhancement method than to our enhancements. In all the measured cases, under the SRC contrast measure, the Wang method produced higher contrast than our enhancement methods. However, this is at the cost of the presented discriminative information in the enhanced mammogram. The SRC method takes into account only the local surroundings of the

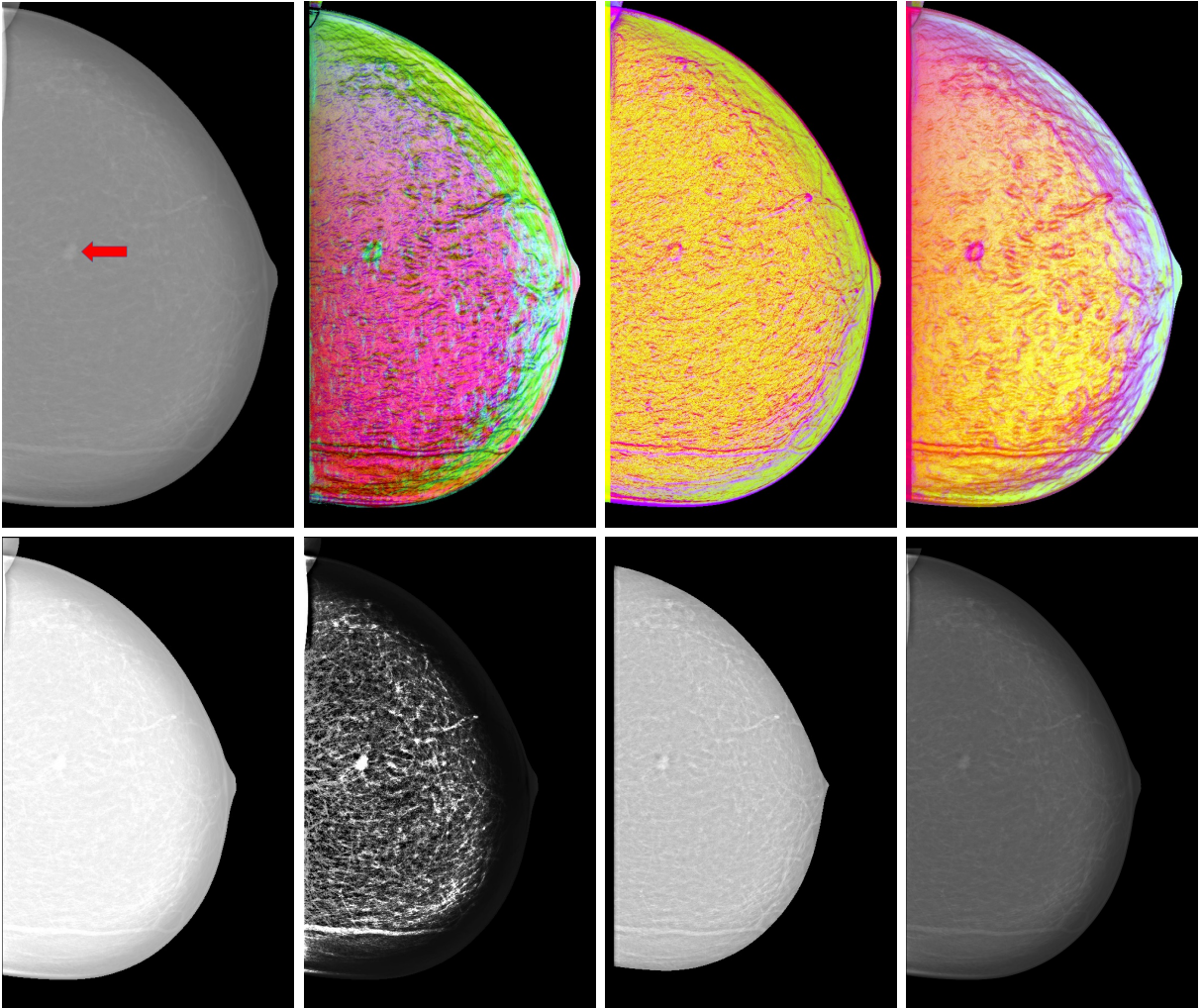


Figure 7.14: Enhanced mammogram example with a dimly visible cancer. Top row from left to right: original with ground truth, enhancement based on prediction probabilities, enhancement based on prediction errors, and combined enhancement. Bottom row from left to right: comparison methods by [54], [53], [41] and [55].

regions of interest, in which the Wang method doubtlessly has higher contrast, but forgoes the many false positive enhancements the Wang method produces.

7.3.5 Visual Evaluation

Fig. 7.12 shows an example of a medio-lateral oblique (MLO) mammogram with a low-contrast lesion and a big calcification. The lesion is better visible in the prediction-probability-based image, which on the other hand almost does not show the calcification, whereas the calcification is brightly highlighted in the prediction-error-based image. The

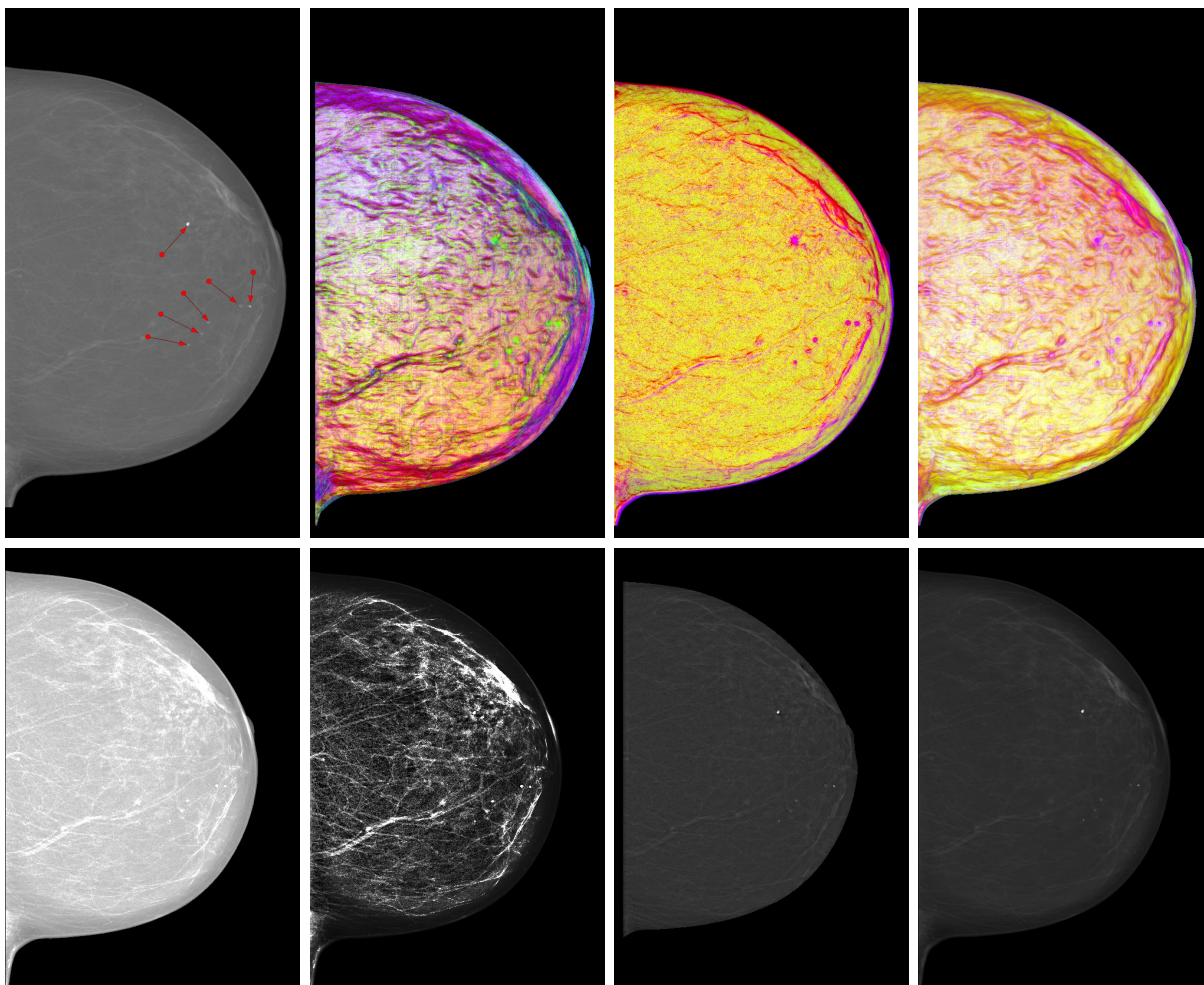


Figure 7.15: Enhanced mammogram example with a several microcalcifications. Top row from left to right: original with ground truth, enhancement based on prediction probabilities, enhancement based on prediction errors, and combined enhancement. Bottom row from left to right: comparison methods by [54], [53], [41] and [55].

combined image shows both abnormalities acceptably. Fig. 7.13 shows another MLO mammogram with an elliptical lesion near its edge. The lesion is visible with equal ease in all three enhanced images. In Fig. 7.14 there is a very small malignancy in a cranio-caudal (CC) mammogram. Because of its size and relatively low contrast in comparison with its surroundings, it is not very visible in either the prediction-probability-based enhancement or the prediction-error-based one. The combined view, however, shows it as a bright red circle.

There are several microcalcifications in the CC mammogram in Fig. 7.15. They are marked as thick blue dots in the prediction-error-based image and as rather bluish dots in the combined view. Because of their size and character, they are omitted by the prediction-

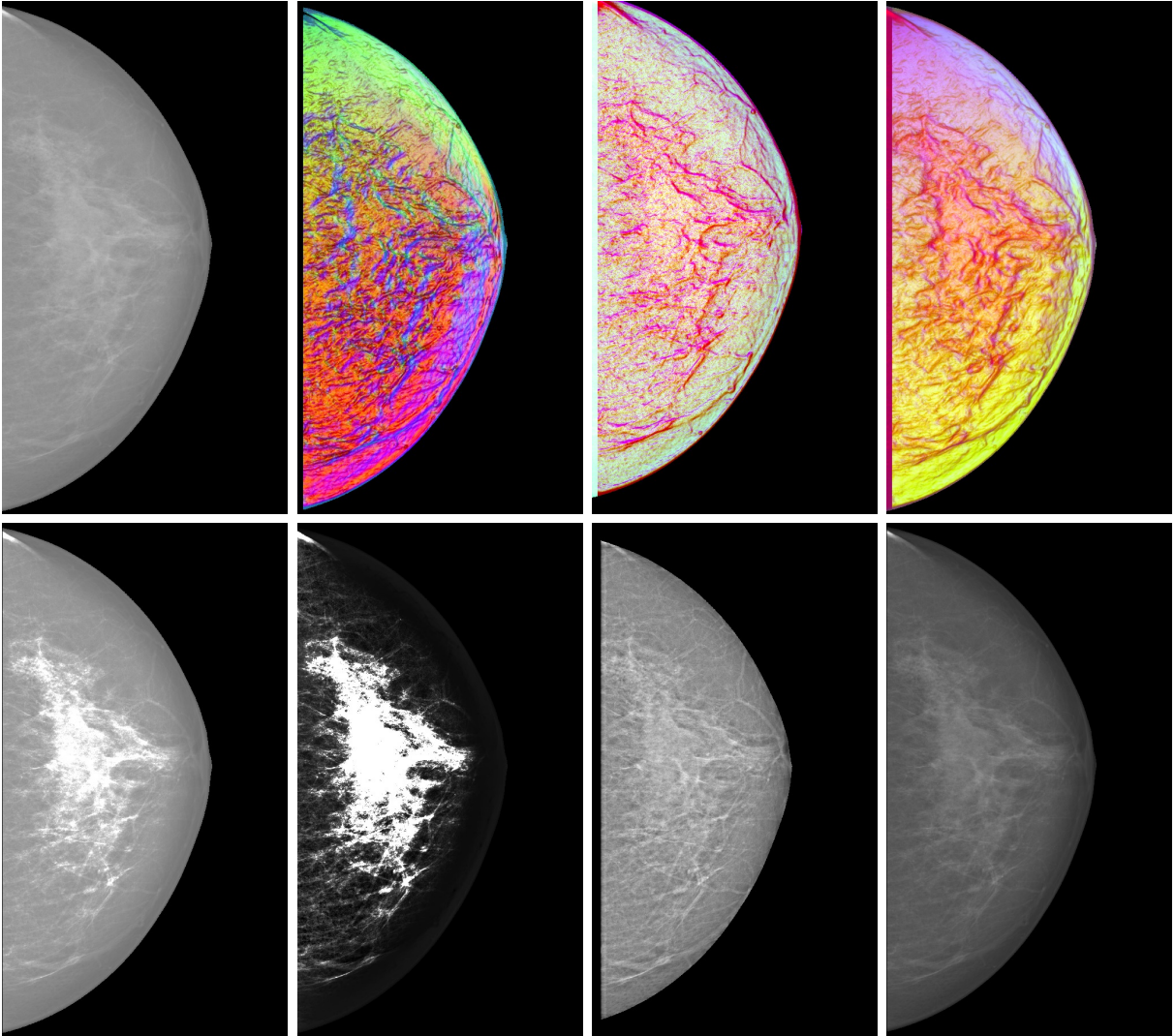


Figure 7.16: Enhanced benign mammogram example. Top row from left to right: original image, enhancement based on prediction probabilities, enhancement based on prediction errors, and combined enhancement. Bottom row from left to right: comparison methods by [54], [53], [41] and [55].

probability-based image.

In the bottom rows of Figs. 7.12, 7.13, 7.14, 7.15, and 7.16, we can see a comparison with methods by Panetta et al., Wang et al., Tang et al. and Bhateja et al. The advantage of our method is in making clearly visible contours around texture abnormalities, microcalcifications, and malignant findings while keeping non-suspicious mammograms (Fig. 7.16) fairly homogeneous in comparison with these alternative methods.

Fig. 7.17 shows an example of texture enhancement in one of the digital mammograph

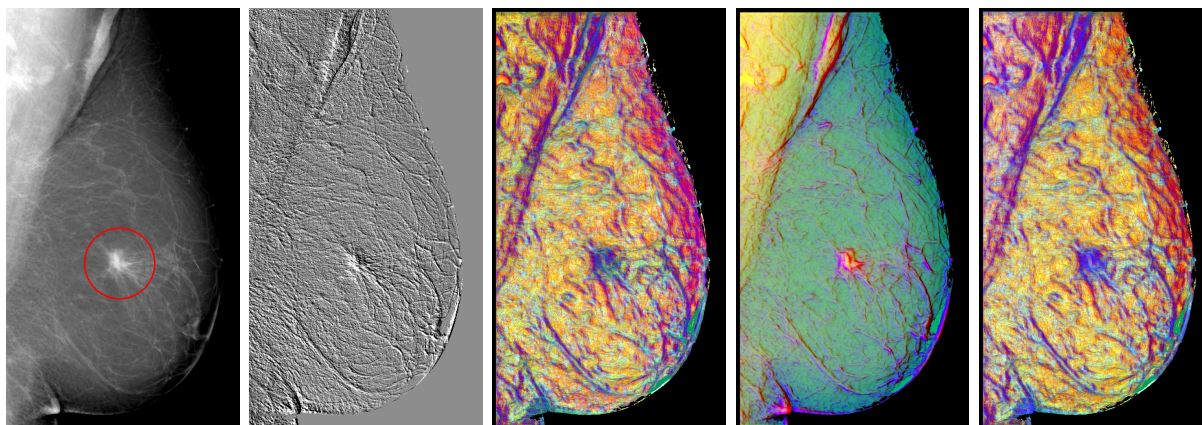


Figure 7.17: Example of the pseudocolour method compared with the unilateral result. Left to right: original with ground truth, enhancement by the unilateral method, enhancement based on prediction probabilities, enhancement based on prediction errors, and combined enhancement.

Senographe 2000 D MLO mammograms using single-directional rightward 2DCAR model using our previously published method [A.2] compared with our new method. It is clearly visible that the lesion and the lymph nodes are better visible in the colored images. The lesion is better visible in the prediction-probability-based enhancement and in the combined enhancement (which is not too different from the probability based one due to lower quality of input data) and the nodes are better visible in the prediction-error-based image.

The use of targeted frequency bands makes the algorithm more susceptible to abnormalities of different sizes, ranging from microcalcifications (Fig. 7.15) to medium-size lesions (Fig. 7.12) and lymph nodes. Larger lesions are enhanced with a somewhat lower contrast, but since they can easily be seen with the naked eye even by untrained people, we do not see this limitation as a serious drawback.

7.3.6 Radiologists' Verification

The presented method was consulted with five expert radiologists who focus solely on mammography. The radiologists underwent a test using a perceptual validation program working with the INbreast database images.

This program generates two types of tests: either the perceptual validation test on the original X-ray mammograms (blind test A) or the test where each window contains the X-ray measurements on the left half of the screen and its enhanced version using the presented method on the right half (enhanced test B, Fig. 7.18).

The radiologists were asked to click on all suspicious-looking spots in the mammogram. They could choose from the three different types of enhancement combined with one of the four enhancement levels (light, medium, heavy, full). All tests were performed with only a

Table 7.2: Tests A and B (radiologists 2 and 3 did not take test A, CS – correctly selected, TS – total selected, TPC – time per case).

Radiologist	#ROIs	#CS	#TS	TPC (s)
Test A				
1	5	5	26	28
2	-	-	-	-
3	-	-	-	-
4	5	5	9	11
5	8	7	22	16
Test B				
1	11	11	29	63
2	5	4	9	27
3	5	5	14	138
4	4(3)	3	17	36
5	7	6	14	42

two-minute introduction without any previous schooling or trials.

Single test screens for both test types were randomly chosen from the combined IN-breast database and the corresponding enhanced mammograms. The success rate of every radiologist was evaluated together with the time spent on evaluation of each spot, screen, and left or right image (for test B).

Each standard test (both A and B) contains 20 different screens, i.e., 40 screens total with images of both benign and malignant instances. However, due to time constraints of the participants, test A is missing and test B contains just 10 and 16 cases, respectively for radiologists numbers 2 and 3. Although any more definite conclusion would need a much larger study, we believe that these results indicate the positive trend of our method. Average time per case for test B is about three times longer than for test A, which is not surprising due to the novelty of the presented method and 12 different configurations of the enhancement settings. We expect comparable times in routine usage.

The results, shown in Tab. 7.2, were comparable. At first glance the results of test B might look a bit worse, which would speak against the proposed enhancement method since while the radiologists missed only one abnormality in test A, they missed two abnormalities in test B. However, the abnormality missed by radiologist No. 5 in test A was classified as BI-RADS 4c, which means higher than intermediate suspicion of malignancy, whereas the abnormalities omitted in test B were BI-RADS 2 and 3, which means benign (BI-RADS 2) and probably benign (BI-RADS 3) findings. Moreover, when we discussed the missed abnormalities with the experts after the test, we found out that radiologist No. 4 did not highlight the BI-RADS 2 finding deliberately as she found it to be a non-suspicious texture summation. Considering this, we added a third row to the summary Tab. 7.3 to show the corrected results. Our radiologist consultants expressed keen interest in the method and

7. MAMMOGRAM TEXTURE ENHANCEMENT

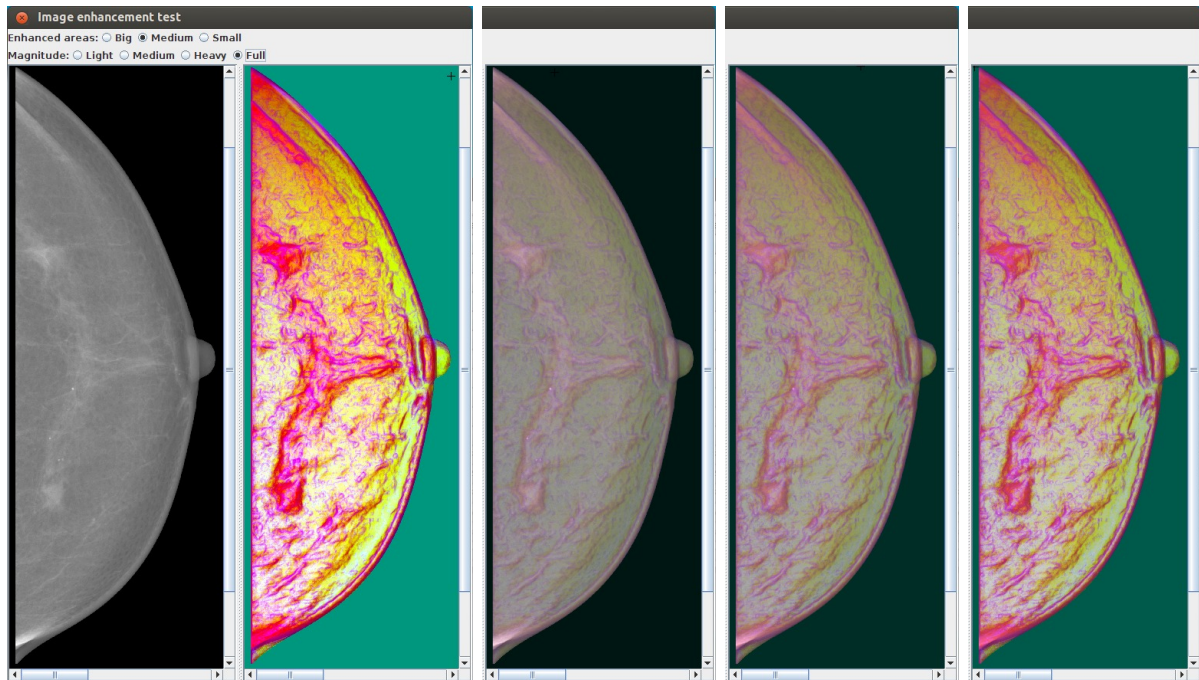


Figure 7.18: Screenshots of the radiologist validation program - test B.

Table 7.3: Summary (TP - true positives, FP - false positives, FN - false negatives).

Summary					
Test	TP	FP	FN	Time (s)	
A	94%	70%	5%	18	
B	90%	65%	9%	62	
B - corrected after discussion	96%	65%	4%	62	

appreciated its outputs.

Local Contrast Criteria

Image enhancement methods aim to improve human image interpretation accuracy by increasing visual distinguishability of single objects recorded in a visual scene. This requires an increase in image contrast which is the relative difference in luminance, colour or texture between multiple objects.

A typical important application for image enhancement is preventive mammography screening. Around 25% of radiologically visible cancers are missed by the radiologists at screening [115] which means that millions of cancer cases are missed every year. In such important image enhancement applications even a slightest improvement in the detection methods could have a huge impact and save many lives. A reliable quality contrast criterion is then the prerequisite for any monitoring of an image enhancement method development progress or for ranking existing methods.

During our work on mammogram enhancement, we encountered several different enhancement measures and contrast measures [75, 76, 77, 78, 79, 80]. When we applied them in our experiments, we found out that their results are rarely consistent with each other (i.e. that their results on different images are sorted in the same order).

In this chapter we investigate the behaviour of different contrast measures on various types and levels of image degradations. In Sec. 8.1 we describe different contrast measure categories and how to apply them for region based contrast estimation, Sec. 8.2 introduces our contrast criterion, Sec. 8.3 describes our contrast validation benchmark and Sec. 8.4 presents the experimental results.

8.1 Contrast Measure Categories

As we have already mentioned in Sec. 2.2.8, contrast criteria can be categorized into three different groups:

1. **Global contrast** measures compute the overall contrast of the whole image.
2. **Local contrast** measures compute the contrast for each and every pixel.

3. **Region contrast** measures compute the contrast of some region of interest with respect to its surroundings and/or the rest of the image.

8.1.1 Modifying Contrast Measures for Regions of Interest

Not all contrast measures can be utilized to computed region contrast directly. In the following sections we propose a simple modification to enable any contrast measure to be applied to region contrast computation.

8.1.1.1 Using global and local contrast measures for region contrast computation

Measuring the contrast for local abnormality enhancement is somewhat dubious since ideally we want to lower the contrast of normal texture as much as possible and only raise the contrast of the abnormalities. Denoting an object O and B as background, we propose the following modification to contrast measures to make them suitable for measuring the contrast of regions of interest:

$$ContrastFactor = \frac{C(O)}{C(B \setminus O)} , \quad (8.1)$$

where $C(.)$ is an arbitrary global contrast measure.

This way we can compute the factor by which the contrast at the abnormality is greater (or lower) than the contrast in the rest of the breast image. The same equation can be directly applied to all the global contrast measures such as the SDME (2.22). For local contrast measures, which give local contrast values for each pixel (denoted $L(x, y)$, where x, y are spatial indices), such as the Wlf_{Rsc} (2.30), we sum the values for each pixel beforehand and take their mean value:

$$ContrastFactor = \frac{|B \setminus O| \sum_{x,y \in O} L(x, y)}{|O| \sum_{x,y \in (B \setminus O)} L(x, y)} \quad (8.2)$$

8.1.1.2 Multispectral generalization of the grayscale contrast measures

The straightforward generalization of monospectral contrast measures $C(.)$ to any d number of spectral bands is

$$C_Q = [C_1, \dots, C_d] Q [C_1, \dots, C_d]^T , \quad (8.3)$$

where Q is some appropriate positive definite weighting matrix. Q can be the unity matrix $Q = diag[1, \dots, 1]$ or for colour images it can be their grayscale conversion, e.g., converted from the RGB colour space:

$$Q = \begin{pmatrix} 0.2989 & 0 & 0 \\ 0 & 0.587 & 0 \\ 0 & 0 & 0.114 \end{pmatrix} .$$

Other possibilities, e.g. those proposed by Simone et al. [78], include using the variance of each channel's values as the weight or $\frac{1}{\mu}$ where μ is the mean value in the colour channel, or simply converting the image to grayscale beforehand.

8.2 Our Proposed Contrast Criterion

We propose a contrast criterion loosely based on the Region contrast (2.32). The main idea is that the distinguishability of a region is mostly influenced by its direct surroundings. Let's define the surroundings $S_{i,d}$ of region i as all pixels which do not belong to the region i and their distance from the region in both x and y axes is at most d . The surrounding region contrast

$$SRC = \frac{\left| \left| \mu_i - \mu_{S_{i,d}} \right| \right|}{\left| \left| \mu_i + \mu_{S_{i,d}} \right| \right|}, \quad (8.4)$$

where μ_i is the mean value of region i and $\mu_{S_{i,d}}$ is the mean value of its surroundings up to the distance d .

The distance d of the surroundings can be determined as either a constant value or relative to the size of the region of interest.

8.3 Contrast Measures Benchmarking

To validate the contrast measures, we take a set of images on which we then apply several different degradations in varying amounts and observe the results of the contrast measures. Ideally, they should behave monotonously. The image degradations, an example of which can be seen in Fig. 8.1, are:

1. Additive Gaussian noise (**GN**), varying standard deviations ($\sigma \in \{10, 20, \dots, 100\}$),
2. Salt and pepper noise (**SP**), varying ratio of presence (10%, 20%, ..., 100%),
3. Linearly combined uniform noise (**U**) (0-255), ratio (10%, 20%, ..., 100%),
4. Gray level range reduction (**LC**) ($\frac{1}{2}, \frac{1}{4}, \dots, \frac{1}{1024}$),
5. Averaging (**AVG**) of values within windows of sizes (1, 3, 5, ..., 21).

8.4 Experimental Validation

We have validated the contrast criteria on the more than 100 grayscale images from the INbreast database [86] which include an abnormal mass and on 20 colour skin images with cancer-like abnormalities. The validated contrast measures are: AME (2.20), AMEE (2.21), EME (2.18), EMEE (2.19), SDME (2.22), C3 (2.27), Wlf_{Rsc} (2.30), BCC (2.33),

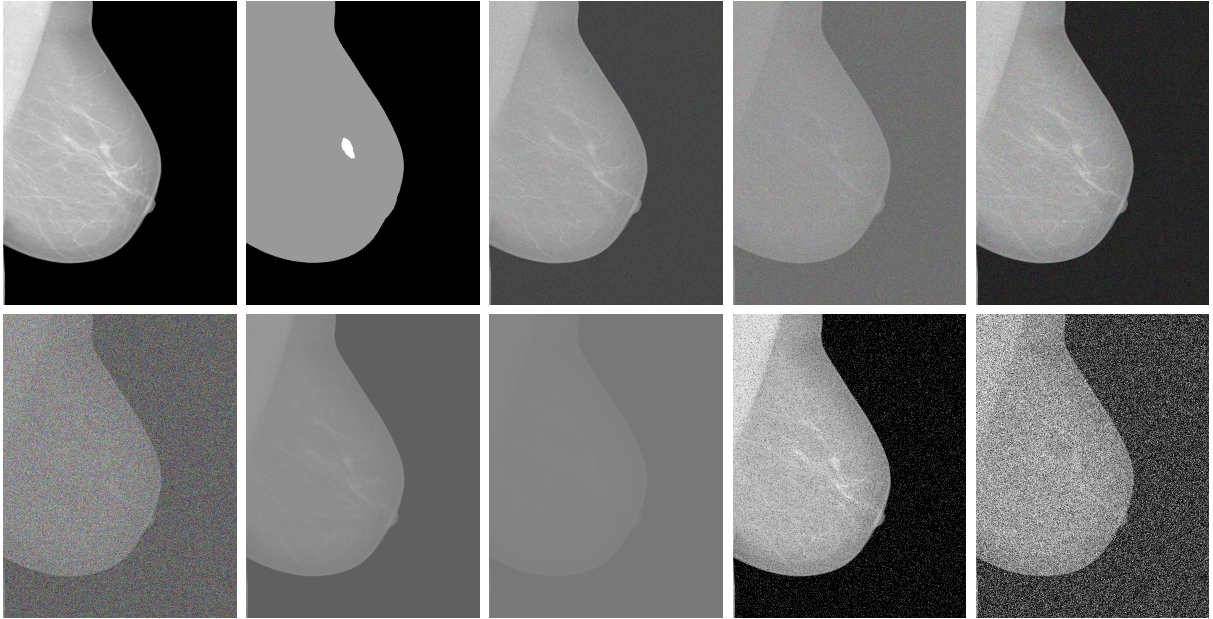


Figure 8.1: Example of image degradations applied to a mammogram. Top row, left to right: mammogram, its region of interest template, and its degradation using the additive Gaussian noise $\sigma = 30$, $\sigma = 100$, additive noise with uniform noise 30% blending. Bottom row, left to right: Additive noise with uniform noise 80%, range reduction 2 bits, range reduction 4 bits, salt and pepper noise 10%, and 50%.

RCC (2.32) and our proposed method, SRC (8.4). The global and local contrasts were modified using our proposed equations (8.1) and (8.2) respectively.

The experiments use the parameters $k_1 = width/5$, $k_2 = height/5$, $\alpha = 0.5$ for AME, AMEE, EME, EMEE, SDME, for C3 and Wlf_{Rsc} (2.29) $\rho_c = 1$, $\rho_s = 2$, $N_l = 5$, λ_l is the variance of pixel values in each channel at level l . For the BCC we have selected a window of size 3×3 , with the window's center 5 pixels distant from the border. Since the C1 (2.25) and C2 (2.26) criteria give values similar to C3 (correlation > 0.99), they are not included in the presented results.

In our proposed method, we set the parameter $d = 6$ to match the contrast measures with similarly parametrized distances.

For a correctly functioning contrast criterion, the corresponding degradation graph should be monotonous and consistent among the different image degradations. The results (plotted in the graphs in Figs. 8.2-8.6) demonstrate that the different contrast criteria are not consistently reliable. The sole two exceptions are the Region contrast criterion (2.32) which only fails in one case (averaging on the dermatological data), and our proposed Surrounding region contrast (8.4), which shows consistent results in all the experiments.

The presented graphs are normalized to the range $< 0; 1 >$ to provide better visual comparison. The horizontal axes start at 0 with the original images and the deterioration

then increase rightwards.

Tab. 8.1 shows a summary of the behaviour of the different contrast measures. We can see that except for the SRC measure, all the contrast measures exhibit non-monotony and the AME, BCC, SDME and $Wlfr_{sc}$ even show inconsistent monotonous behaviour (for some degradations, they are monotonously increasing while for others they are decreasing). The second best enhancement measure is the RCC which only exhibited one minor non-monotony in one case but otherwise behaved consistently.

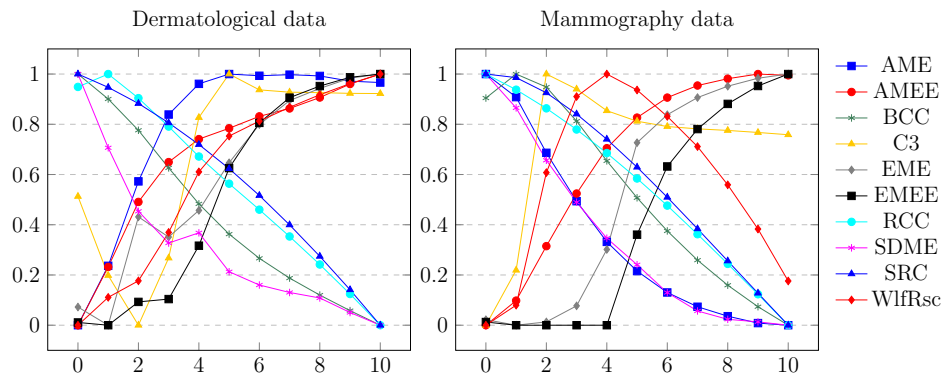


Figure 8.2: The criteria behaviour for the averaging image degradation. Left: dermatological data (colour), right: mammography data (grayscale).

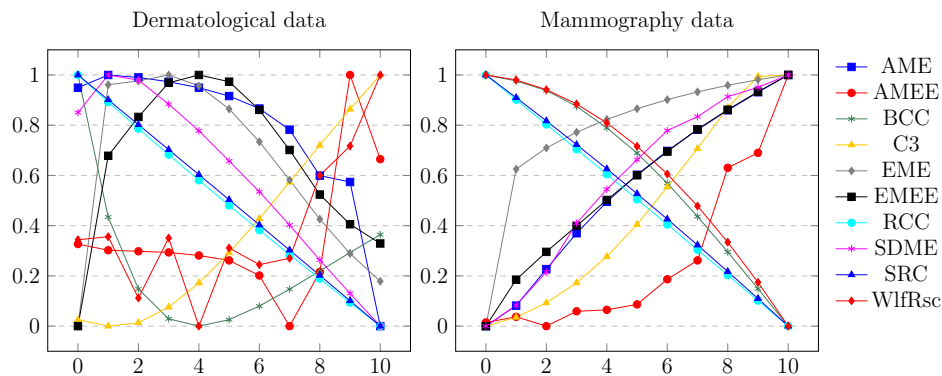


Figure 8.3: The criteria behaviour for the Gaussian noise image degradation. Left: dermatological data (colour), right: mammography data (grayscale).

8. LOCAL CONTRAST CRITERIA

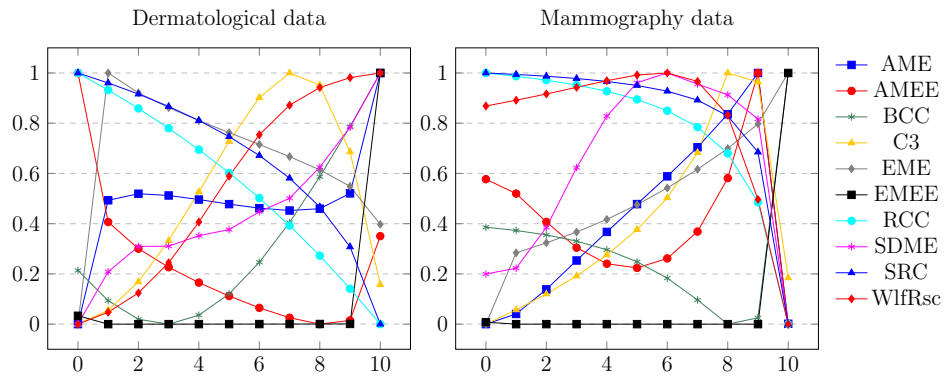


Figure 8.4: The criteria behaviour for the uniform noise image degradation. Left: dermatological data (colour), right: mammography data (grayscale).

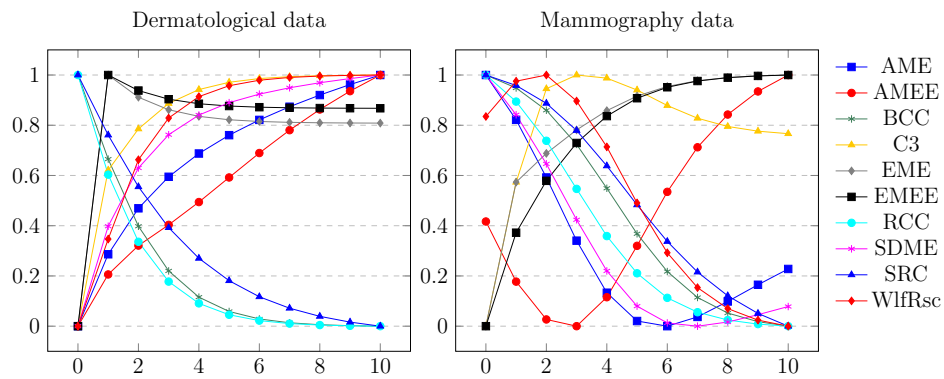


Figure 8.5: The criteria behaviour for the range reduction image degradation. Left: dermatological data (colour), right: mammography data (grayscale).

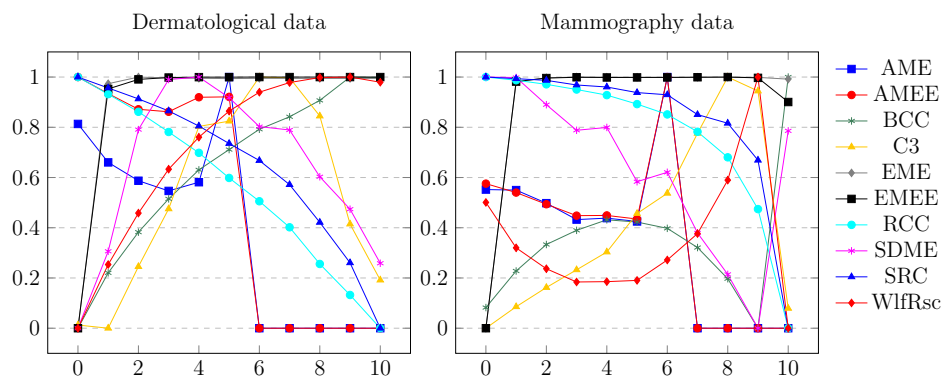


Figure 8.6: The criteria behaviour for the salt and pepper noise image degradation. Left: dermatological data (colour), right: mammography data (grayscale).

	Dermatological data (colour)					Mammography data (grayscale)				
	AVG	GN	U	LC	SP	AVG	GN	U	LC	SP
AME	x	x	x	↑	x	↓	↑	↑	x	x
AMEE	↑	x	x	↑	x	x	x	x	x	x
BCC	↓	x	x	↓	↑	x	↓	x	↓	x
C3	x	↑	x	↑	x	x	↑	x	x	x
EME	x	x	x	x	x	x	↑	↑	↑	x
EMEE	x	x	x	x	x	x	↑	x	↑	x
RCC	x	↓	↓	↓	↓	↓	↓	↓	↓	↓
SDME	x	x	↑	↑	x	↓	↑	x	x	x
SRC	↓	↓	↓	↓	↓	↓	↓	↓	↓	↓
Wlf_{Rsc}	↑	x	↑	↑	x	x	↓	x	x	x

Table 8.1: Summary of the behaviour of the different contrast measures among different degradations. ↑ means monotonous increasing, ↓ means monotonous decreasing and x means non-monotonous behaviour.

Developed Software

To our knowledge, there is no application or software library which would implement the texture models we are using for our work, so we had to implement all the methods on our own.

All the described methods were implemented in the Java programming language (mostly versions 7 and 8) taking into account object oriented programming best practices. The software bundle is actively used for texture synthesis and mammography analysis research at the Department of Pattern Recognition of the Institute of Information Theory and Automation of the Czech Academy of Sciences. The software is platform independent and takes advantage of modern multi-processor computers by automatically detecting the number of available CPU cores and scaling accordingly whenever the computation can be parallelized. The bundle consists of over 2 MiB of sources with over 70 000 lines of code.

In the following sections we present a short introduction into the developed software. Sec. 9.1 presents the applications developed for the study of the Potts model, Sec. 9.2 describes the application developed for mammography analysis, Sec. 9.3 introduces our supervised segmentation application, Sec. 9.4 deals with our framework for storing and analyzing the results of experiments, Sec. 9.5 describes our framework for easy parametrization of console applications and, finally, Sec. 9.6 provides a short list of external libraries that we used.

9.1 Potts Applications

We have developed two applications for the modeling of the Potts random field. One is for the hierarchical Potts mimicking (Sec. 9.1.1) and the other is for Potts mosaics (Sec. 9.1.2).

9.1.1 Hierarchical Potts Texture Mimicking

Fig. 9.1 shows our application for working with the hierarchical Potts field. It allows us to import an image, select different colours and group them together in hierarchy, select

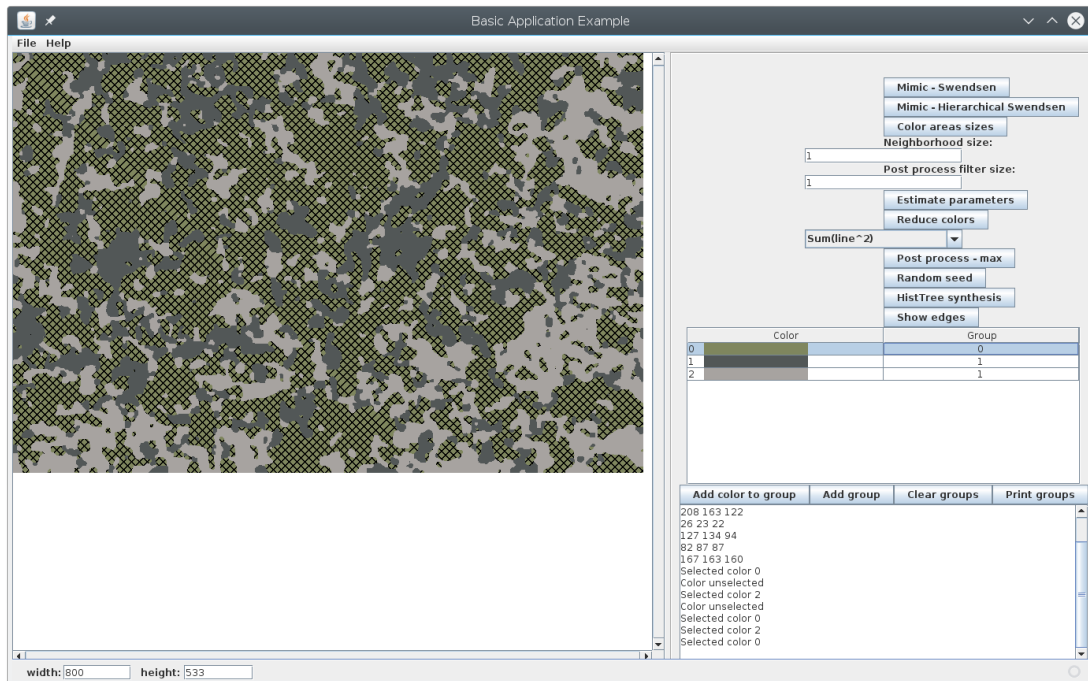


Figure 9.1: Example of our application for Potts hierarchical mimicking with one selected colour.

different measures for the Potts field synthesis (Sec. 5.1), run the mimicking synthesis and post process the resulting image.

9.1.2 Potts Mosaics

The Potts mosaic application (Fig. 9.2) has a very simple gui which allows us to import an image, filter it and run the mimicking synthesis procedure.

9.2 Mammograms

9.2.1 Graphical User Interface

The graphical user interface for mammogram analysis mostly comprises of the view of the mammogram database (Fig. 9.3). The table containing the information on the database's cases is procedurally generated and depends on the type of database displayed as all the mammogram databases provide different information.

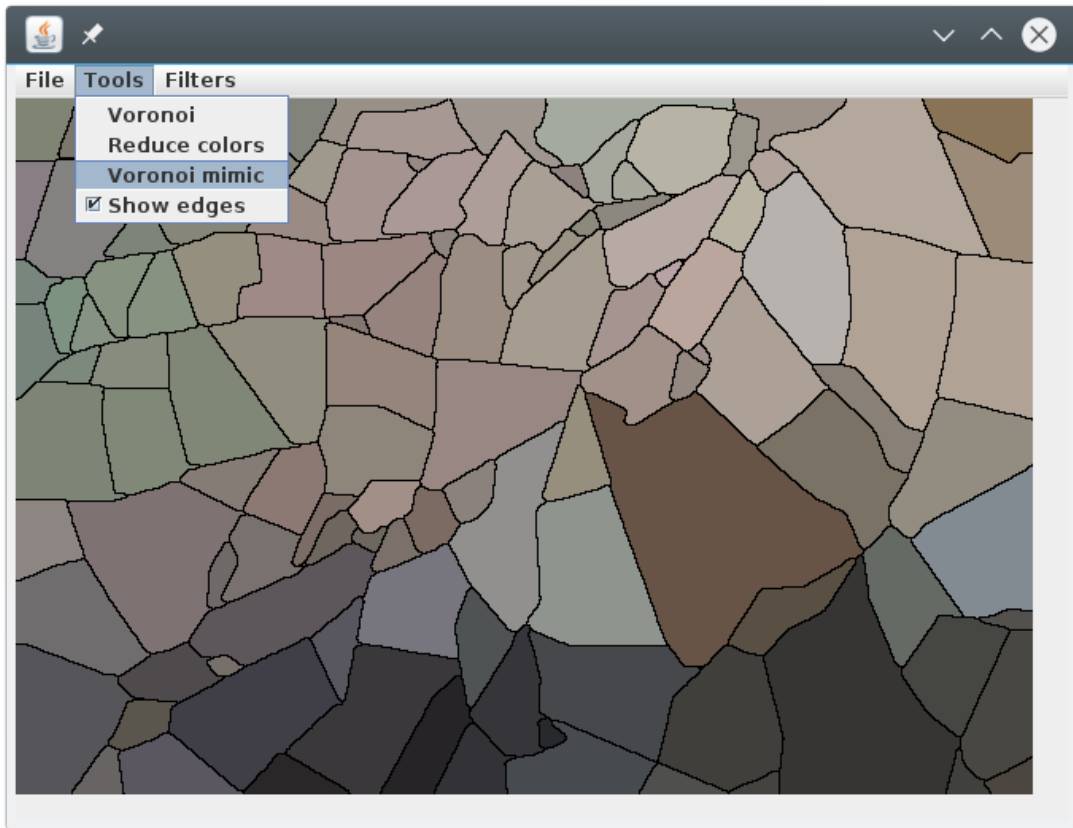


Figure 9.2: Example of our application for Potts mosaics.

9.2.2 Unified Interface for Mammogram Databases

Following the “low coupling - high cohesion” principle of object oriented design, we have one shared interface for all mammogram databases and database entries, as shown in Fig. 9.4. In the diagram, we can see that the *MammoDBEntry* is a class instead of an interface. This was caused historically by the class having some default implementations and can be implemented in an interface since Java 8, which will be done by simple refactoring in future work. This approach allows us to seamlessly switch between mammogram databases without any change to the developed algorithms for their analysis.

9.3 Supervised Texture Model Based Segmentation

We have developed a general application supervised segmentation using different texture models. Fig. 9.5 shows the segmentation application and segmentation result. An interesting option of the segmentation application is the possibility to visualize the features and feature space of the training samples as shown in Fig. 9.6

9. DEVELOPED SOFTWARE

ID	File Name	Laterality	View	Acquisition date	ACR	BI-Rads	Mass	Micros	Distortion	Asymmetry	Findings Note	Lesion Annota.	Pectoral Muscl.
91b13c59bcb...	22678622	R	CC	201001	4	1					normal	No annotation...	
91b13c59bcb...	22678646	L	CC	201001	4	3	X				nodulo	No annotation...	
91b13c59bcb...	22678670	R	MLO	201001	4	1					normal	No annotation...	
91b13c59bcb...	22678694	L	MLO	201001	4	3	X				nodulo	No annotation...	
9b0248042c...	22614074	R	CC	201001	2	5	X	X			nodulo QSE + ...		
9b0248042c...	22614097	L	CC	201001	2	2	X	X			nodulo + micros		
9b0248042c...	22614127	R	MLO	201001	2	5	X	X			nodulo QSE + ...		
9b0248042c...	22614150	L	MLO	201001	2	2	X	X			nodulo + micr...		
97ec8cafc7...	50997434	L	MLO	201001	3	2		X			micro		
97ec8cafc7...	50997460	R	MLO	201001	3	4a	X	X			nodulo QSE + ...		
97ec8cafc7...	50997488	L	CC	201001	3	2		X			micro		
97ec8cafc7...	50997515	R	CC	201001	3	4a	X	X			nodulo QSE + ...		
ac318518fd...	24055445	L	MLO	200801	1	4c	X	X			nodulo + micros		
ac318518fd...	24055468	R	MLO	200801	1	4c	X	X			nodulo + micros		
ac318518fd...	24055483	L	CC	200801	1	4c	X	X			nodulo + micros		
ac318518fd...	24055502	R	CC	200801	1	4c	X	X			nodulo + micros		
5530d5782fc...	22580192	R	CC	201001	2	3		X			nodulo benigno		
5530d5782fc...	22580218	L	CC	201001	2	1		X			normal	No annotation...	
5530d5782fc...	22580244	R	MLO	201001	2	3		X			nodulo benigno		
5530d5782fc...	22580270	L	MLO	201001	2	1		X			normal	No annotation...	
66adfb0f19c...	50998933	R	CC	201001	3	2					micros + calcif...		
66adfb0f19c...	50998958	L	MLO	201001	3	5		X			micros		
66adfb0f19c...	50998986	R	MLO	201001	3	2		X			micros + calcif...		
66adfb0f19c...	50999113	L	CC	201001	3	5		X			micros		
66bfc58a81e...	50997742	L	MLO	201001	1	3		X			micros		
66bfc58a81e...	50997769	R	MLO	201001	1	3		X			micros		
66bfc58a81e...	50997796	L	CC	201001	1	3		X			micros		
66bfc58a81e...	50997823	R	CC	201001	1	3		X			micros		
e15a1697b4f...	22670620	R	CC	201001	1	2		X			nodulo QSE ...		
e15a1697b4f...	22670643	L	CC	201001	1	1		X			normal	No annotation...	
e15a1697b4f...	22670673	R	MLO	201001	1	2		X			nodulo QSE ...		
e15a1697b4f...	22670703	L	MLO	201001	1	1		X			normal	No annotation...	
b231a8b44d5...	53581376	L	MLO	201001	1	1		X			normal	No annotation...	
b231a8b44d5...	53581406	R	MLO	201001	1	6	X	X			nodulo QSE		
b231a8b44d5...	53581460	R	CC	201001	1	6	X	X			nodulo QSE	No annotation...	
c01183a1eb28...	24058533	L	MLO	200802	3	2		X			micros		
c01183a1eb28...	24058560	R	MLO	200802	3	2		X			micros		
c01183a1eb28...	24058587	L	CC	200802	3	2		X			micros		
c01183a1eb28...	24058614	R	CC	200802	3	2		X			micros		
839819f2e8d...	24055877	L	MLO	200901	1	2		X			micro		
839819f2e8d...	24055904	R	MLO	200901	1	2		X			calcifications		
839819f2e8d...	24055931	L	CC	200901	1	2		X			micro		
839819f2e8d...	24055958	R	CC	200901	1	2		X			calcifications		
d2bfe622a1...	53587427	L	MLO	201001	2	2		X			micro		
d2bfe622a1...	53587454	R	MLO	201001	2	2		X			micros		
d2bfe622a1...	53587481	L	CC	201001	2	2		X			micros		
d2bfe622a1...	53587508	R	CC	201001	2	2		X			micro		
964793957f...	51048462	L	MLO	201001	2	2		X			micros		
964793957f...	51048489	R	MLO	201001	2	2		X			microcalcificac...		
964793957f...	51049516	L	CC	201001	2	2		X			micros		
964793957f...	51049543	R	CC	201001	2	2		X			calcifications		
964793957f...	51049628	L	MLO	200901	2	2		X			micros		
964793957f...	51049655	R	MLO	200901	2	2		X			calcifications		
964793957f...	51049682	L	CC	200901	2	2		X			micros		
964793957f...	51070197	R	CC	200901	2	2		X			microcalcificac...		
40e22f2e2321...	53580638	R	MLO	201001	1	3		X			micros		
40e22f2e2321...	53580665	L	CC	201001	1	2		X			microcalcificac...		
40e22f2e2321...	53580692	R	CC	201001	1	3		X			microcalcificac...		
80be343339f...	53580660	L	MLO	201001	1	2	X	X			add-structure...		

Figure 9.3: Example of our application for mammogram analysis.

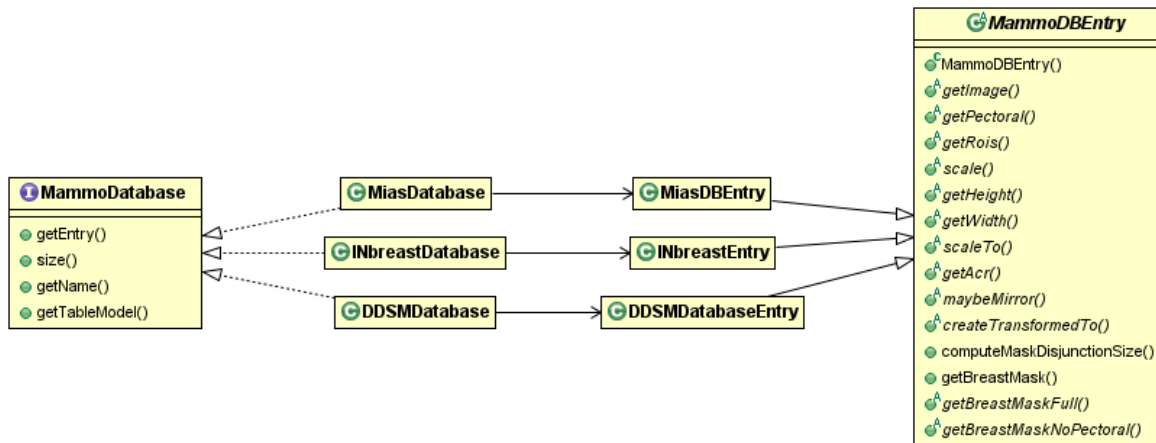


Figure 9.4: Class diagram of the mammogram databases.

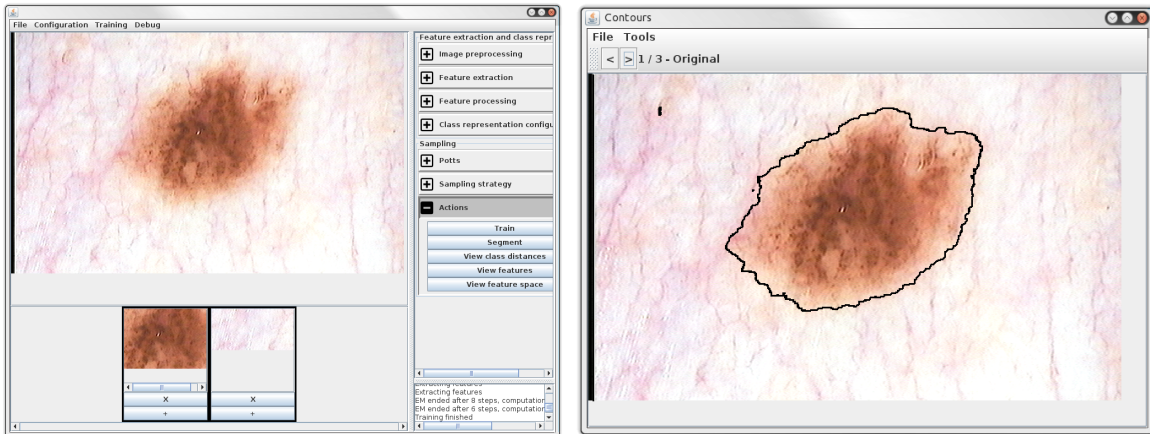


Figure 9.5: Segmentation application example. Left: the application with training samples, right: the segmentation result.

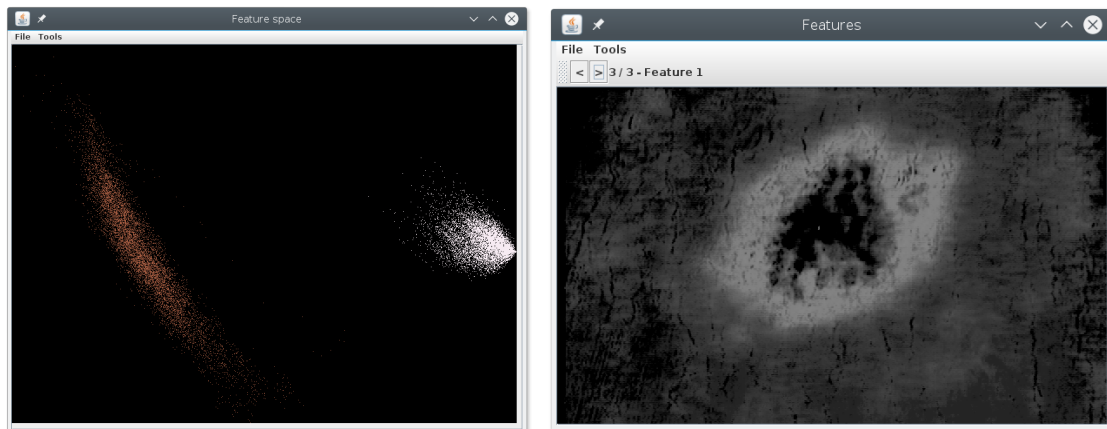


Figure 9.6: Visualization of the feature space (left) and features for each pixel (right).

The segmentation model and trained parameters are designed to be easily storable in human readable configuration files. These can later be easily loaded and executed as shown for example in Fig. 9.7 which presents code used for the segmentation of digitized mammograms from the MIAS database.

9.4 Storing and Analyzing Results

During our work, we have designed a unified approach of storing and analyzing the measured results of our experiments. The way the results are stored can be seen in Fig. 9.8 (this figure shows an actual code from our project). We can see that every result data can have multiple parameters on which it depends and can also store multiple result values

9. DEVELOPED SOFTWARE

```
// load configuration from file
SegmentationConfiguration configuration =
    ResourceHelper.loadYamlObjectFromResource("yaml/mias_gray.yml", SegmentationConfiguration.class);

// initialize segmentation worker
SegmentationWorker segmentationWorker = new SegmentationWorker(configuration);

// perform segmentation
int [][] segmentation = segmentationWorker.runSynchronousSegmentation(sourceImage);

// postprocessing - smoothen
ClassificationUtils.postProcess(segmentation, 2, 2);

// final result
boolean [][] mask = ClassificationUtils.extractLargestArea(segmentation, 0);
```

Figure 9.7: Sample code for digitized mammogram segmentation.

```
// set the results to be stored into the given output file
ResultSet rs = new ResultSet(outputFile);

ResultsData rd = new ResultsData();
rd.putParam("discretization", disc);
rd.putParam("size", size);
rd.putParam("neighborhood", neighborhood);
rd.putResult("#correctly classified", result);
rd.putData("contingency table", new ContingencyTableHolder(contingencyTable));

rs.addResultData(rd);
```

Figure 9.8: Sample code for our results management.

(although the example shows only one). Apart from that, every result data can also hold a number of additional information about the result, e.g. the configuration of the segmenter. Several different types of values can be stored ranging from numbers, text, contingency tables to neighbourhood information for the CAR model. The data is stored using the YAML format.

The stored set of results can be easily read and analyzed either programmatically or using our result viewing application (see Fig. 9.9). The gui changes according to the structure of the results data. All the results, plots, contingency tables, etc., can be exported to \LaTeX on one click.

9.5 Parametrizing Runnables

Graphical user interface is not always the most convenient means of executing experiments. Using command line interface is quite often more suitable, e.g. when executing various batches of data or when accessing a remote computer through ssh.

9.5. Parametrizing Runnables

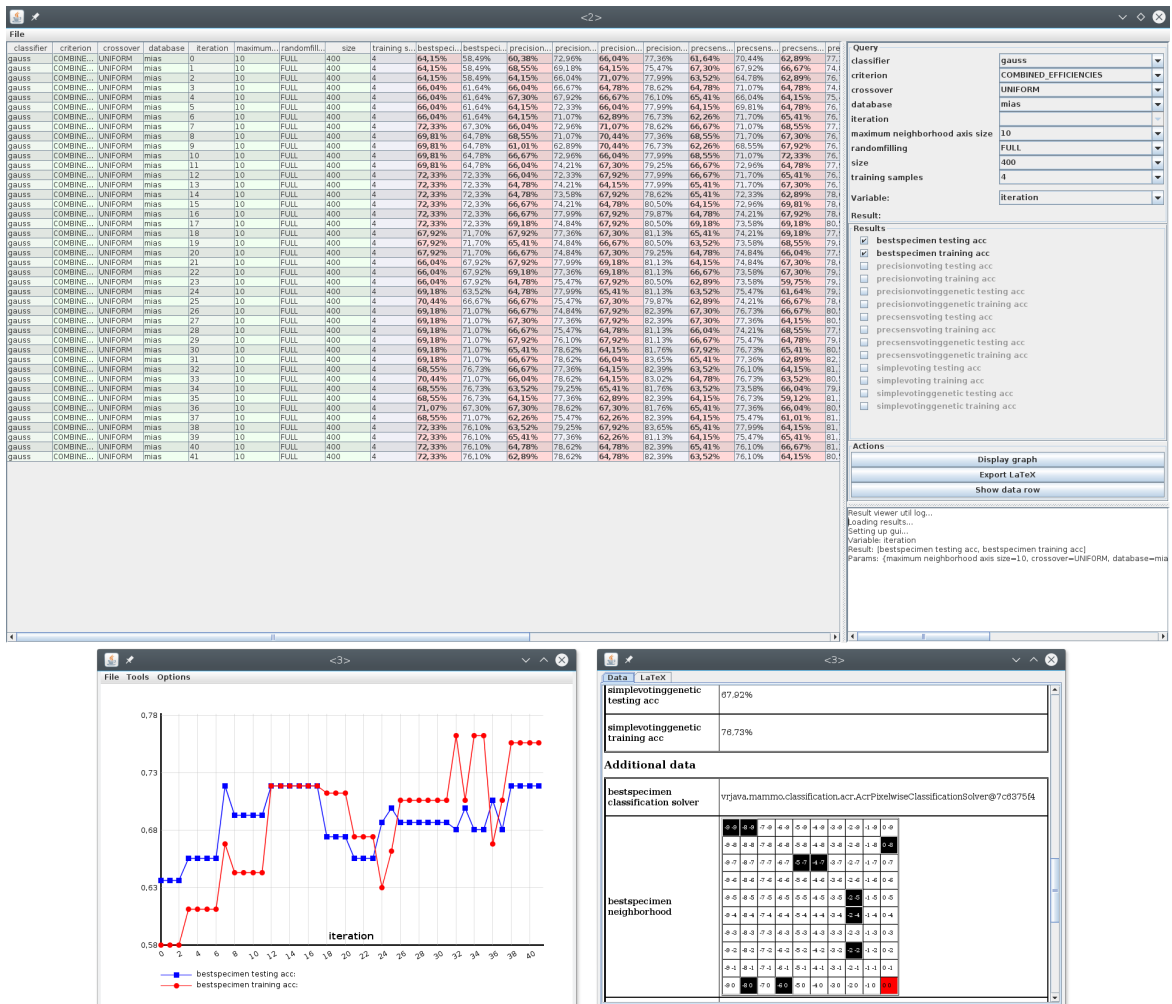


Figure 9.9: Results viewer application example. Top row: overall view of all the results with results, parameters and additional information distinguished by colour. Bottom row, left: plot of two different results depending on the same variable, right: detail of one results data showing the neighbourhood of the CAR model along with some results.

9. DEVELOPED SOFTWARE

```
@ParameterField
public static int someValue = 10;

>Action(value="init database", calledAlways=true, isInit=true, initOrder=0)
public static void initDatabase(String db, String dbPath) { ... }

>Action(value="analyze")
public static void runAnalyzeDatabase(String [] fileNameTemplates, int discretization,
    int startSize, int startNeighborhood) { ... }

public static void main(String[] args) throws Exception {
    ArgumentsHelper.processArguments(args, Main.class);
}
```

Figure 9.10: Sample code for our arguments annotations.

```
action=genetics
db=mias
dbPath=/dev/shm/MIAS/data.txt
inputDirPath=./
fileNameTemplates=mias_, inbreast_, dds_
outputFile=output.yml
keptBestSpecimenRatio=0.05
randomSpecimenRatio=0.02
geneticSurvivability=0.95
fillRatio=0.2
nIterations=10000
maxThreadRatio=0.7
```

Figure 9.11: Sample configuration of a console application.

We have implemented a user friendly way of parametrizing our console application without the need of manually parsing the command line arguments or configuration files. Each parametrized variable or method can be decorated with an **Annotation** providing the information on its parametrization (a sample code can be seen in Fig. 9.10). The `ArgumentsHelper.processArguments(...)` method then analyzes the given class, finds all the annotations and sets the parameters according to their type. The parameters can be passed either as command line arguments or within a configuration file. An example configuration can be seen in Fig. 9.11. If the arguments are set incorrectly, the application prints the error line along with an automatically generated help and exits.

If the application has too many different parameters, writing them down by memory or from help text could be cumbersome. For this case we have implemented a graphical application which automatically generates a form for the arguments of a given executable, checks the validity of the arguments and in the end either outputs a configuration file or directly runs the application (see Fig. 9.12).

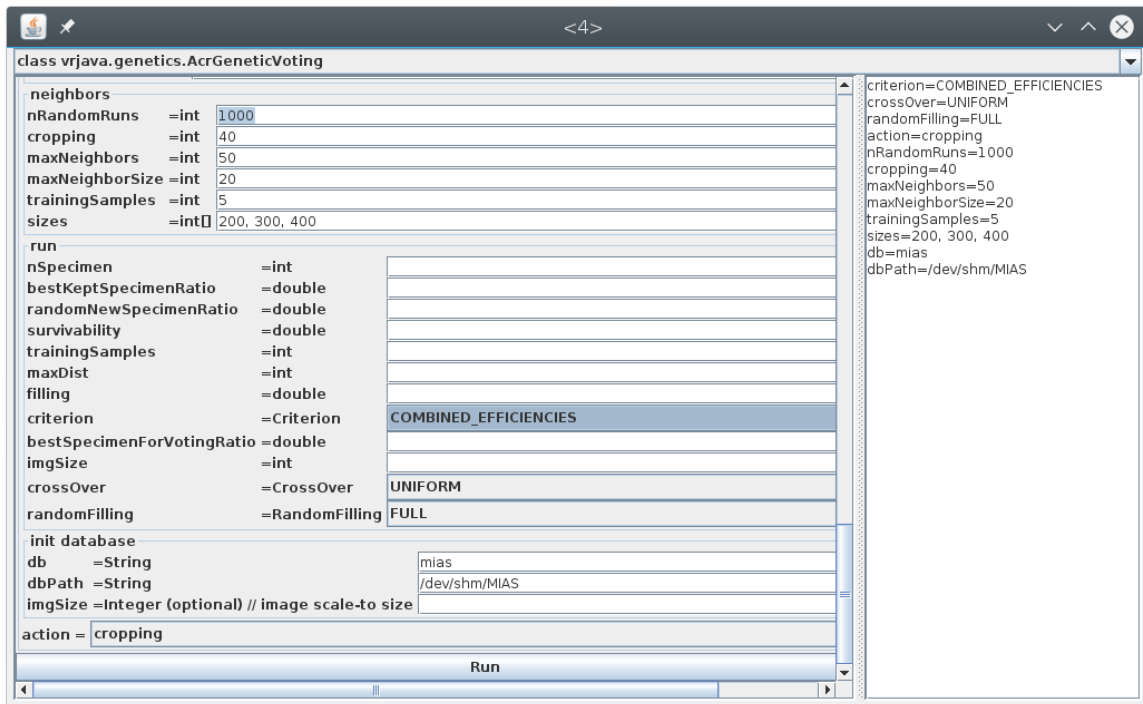


Figure 9.12: Arguments viewer application example.

9.6 External Libraries Used

We used the external libraries listed in Tab. 9.1 for the development of our software. They are all opensource and thus enabled us to make modifications to better work with our own code where necessary.

Name	Url	Licence	Notes
JWave	https://github.com/cscheiblich/JWave	Apache 2.0	Used for fast wavelet transform.
ImageJ	https://imagej.net/ImageJ	BSD, GPL	Used for reading DICOM images.
JLatexMath	https://github.com/opencollab/jlatexmath	GPL	Used for drawing latex equations in Java applications.
opencsv	http://opencsv.sourceforge.net/	Apache 2.0	Used for reading / writing CSV files.
YamlBeans	https://github.com/EsotericSoftware/yamlbeans	Free	Used for parsing / writing yaml files.
Guava	https://github.com/google/guava	Apache 2.0	Utilities for easier Java development.

Table 9.1: External libraries used in our project.

Conclusions

We have developed several state-of-the-art descriptive multidimensional textural models of the Markovian type together with corresponding methods for their statistics estimation and efficient synthesis. The models allow for seamless multispectral/BTF texture synthesis and enlargement with an extremely high compression rate independent of the size of the desired resulting texture. The data needed to be stored is comprised of only several dozens of parameters. Using a simple modification of the method we can use it for texture editing (by changing the local texture models for several indices of the control field) or even the synthesis of new, unmeasured textures by manually assigning the models' parameters. We have successfully applied these models to physically correct surface materials' appearance synthesis and editing as well as to mammography applications.

We have presented two methods for breast density classification in X-ray mammography. The methods were tested on the widely known MIAS database and the state-of-the-art INbreast database, and our results are promising and competitive. Furthermore, the intermediate results of our method can be used for preliminary breast tissue type classification.

We have developed several methods for completely automatic mammogram enhancement. These methods are based on the descriptive textural models developed in the thesis which automatically adapt to the analyzed X-ray texture, thus being universal for any type of input without the need of further manual tuning of specific parameters. Although the algorithms use random-field-type models, the models are very fast thanks to efficient recursive and numerically robust model estimation, and therefore it is much faster than the usual alternative Markov random field models, which require an approach based on the Markov chain Monte Carlo estimation.

Our methods' outputs highlight regions of interest, detected as textural abnormalities. Cancerous areas typically manifest themselves in X-ray images as such textural defects. The methods provide the possibility of enhancement tuned to specific types of mammogram tissue. Thus, the enhanced mammograms can help radiologists to decrease their false negative evaluation rate. It has been shown that the algorithms work well both for small findings, such as microcalcifications, and for bigger lesions. In the examples it can be

seen that even barely visible abnormalities, with the same average gray level as their surroundings, are highlighted very well using our methods, and this could be of great benefit in breast cancer detection.

The pseudocolour method offers a unique way of mammogram feature fusion for visual evaluation and vastly enriches the the information content of the enhanced mammogram. We have compared our pseudocolour enhancement method with four state-of-the-art methods and visually and numerically evaluated the results. Our method shows better sensitivity for enhancing both larger and smaller abnormalities. These observations are confirmed by numerical state-of-the-art contrast criteria, and also by our radiologist consultants.

We have implemented a new contrast criterion and compared it with nine different existing contrast criteria using our developed benchmark. It has been shown that for the purposes of region of interest enhancement validation, very few contrast measures can be trusted.

10.1 Contributions

The thesis contributions are summarized in the following list:

1. Descriptive multidimensional texture models development for texture analysis and synthesis applications
 - a) Hierarchical Potts MRF model (Sec. 4.1.2).
 - b) Directional CAR models (Sec. 4.2.1)
 - c) Spiral CAR models (Sec. 4.2.2)
 - d) Compound Potts MRF model (CMRF^{P3AR}) (Sec. 5.1.1)
 - e) Compound Potts Voronoi MRF model (CMRF^{PV3AR}) (Sec. 5.2).
 - f) Algorithm for estimation of Potts model parameters for texture mimicking (Sec. 5.1.3)
2. X-ray mammograms tissue analysis based on the descriptive multidimensional texture models
 - a) Algorithm for breast composition classification (Sec. 6.2)
 - o A sub-result is the classification of texture in mammograms into fatty and dense (Sec. 6.2)
 - b) Potts model based classification of breast composition (Sec. 6.4)
3. Development of methods for mammogram parenchymal patterns enhancement
 - a) Unilateral method for mammogram enhancement with three specific tissue targeted outputs (Sec. 7.1)
 - b) Nonrigid bilateral comparison method (Sec. 7.2.1)

- c) Texture model based bilateral comparison method (Sec. 7.2.2)
 - d) Pseudocolour enhancement method (Sec. 7.3)
4. Development of image enhancement criteria and their verification
- a) Contrast criteria comparison using our benchmark (Sec. 8.3)
 - b) Region contrast criterion SRC which passes all our benchmarking conditions (Sec. 8.4)

10.2 Future Work

Not all the theoretical results achieved in the thesis were already applied and published. In the near future, we would like to verify the spiral CAR models, derive Markovian rotational invariance and apply them to rotational invariant material recognition.

The Compound MRF models will be exploited in texture editing applications.

We would also like to further our focus on mammography analysis. We would like to apply the probability models to risk assessment based on the mammogram composition recognition.

As we have recently acquired a database of dermatological images, we would like to broaden our medical imaging focus in this area, where we will apply our models in skin lesion analysis and illness progress monitoring.

10.2.1 Mammography Analysis

Our research in mammography is anything but finished. We have shown that our methods lead to an improvement of automated mammogram analysis but further research in this area is still necessary.

10.2.1.1 Segmentation of Regions of Interest

The main focus of all automated mammogram analysis is the effort to automatically find regions in the mammograms which could be of help for the radiologists during diagnosis. In this work we focused on accentuating the areas of mammograms which differed from their counterparts in the mammogram of the other breast or from its own breast's texture. The natural advancement is that we would like to be able to help the radiologists find the carcinomas. Therefore we would like to further lead our research to segmentation of microcalcifications, lymphatic nodes and mass lesions.

10.2.1.2 Mammogram Modeling

Thanks to the descriptive textural models, we could not only more accurately analyze the measured visual data, but if we were immodest, we could synthesize artificial mammogram phantoms to e.g. help with the training of new radiologists.

10.2.2 Multidimensional Random Fields

Nontrivial Markov random fields are one of the best means of texture modeling, which is the reason why we are using them for medical image analysis. We would also like to further explore them in general and hopefully further develop novel MRF models which could be more suitable for medical image purposes.

Bibliography

- [1] Tweed, T.; Miguet, S. Automatic Detection of Regions of Interest in Mammographies Based on a Combined Analysis of Texture and Histogram. In *Pattern Recognition, 2002. Proceedings. 16th International Conference on*, volume 2, Los Alamitos, CA, USA: IEEE Computer Society, 2002, pp. 448–452, doi:<http://doi.ieeecomputersociety.org/10.1109/ICPR.2002.1048335>.
- [2] Qi, H.; Diakides, N. A. Thermal Infrared Imaging in Early Breast Cancer Detection - A Survey of Recent Research. In *Proceedings of the 25th Annual International Conference of the IEEE Engineering in Medicine and Biology Society*, volume 2, IEEE, 2003, pp. 1109–1112.
- [3] Taylor, P. and Champness, J. and Given-Wilson, R. and Johnston, K. and Potts, H. Impact of computer-aided detection prompts on the sensitivity and specificity of screening mammography. 2005.
- [4] Freer, T.W. and Ulissey, M.J. Screening mammography with computer-aided detection: Prospective study of 12,860 patients in a community breast center1. *Radiology*, volume 220, no. 3, 2001: pp. 781–786.
- [5] Brem, R.F. and Schoonjans, J.M. Radiologist detection of microcalcifications with and without computer-aided detection: a comparative study. *Clinical radiology*, volume 56, no. 2, 2001: pp. 150–154.
- [6] Astley, SM and Gilbert, FJ. Computer-aided detection in mammography. *Clinical Radiology*, volume 59, no. 5, 2004: pp. 390–399.
- [7] Haindl, M.; Filip, J. *Visual Texture*. Advances in Computer Vision and Pattern Recognition, London: Springer-Verlag London, January 2013, ISBN 978-1-4471-4901-9 (Print) 978-1-4471-4902-6 (Online), 1-284 pp., doi:<http://dx.doi.org/10.1007/978-1-4471-4902-6>.

- [8] Haindl, M.; Šimberová, S. A multispectral image line reconstruction method. *Theory & Applications of Image Analysis*, 1992: pp. 306–315.
- [9] Haindl, M. Visual Data Recognition and Modeling Based on Local Markovian Models. In *Mathematical Methods for Signal and Image Analysis and Representation, Computational Imaging and Vision*, volume 41, edited by L. Florack; R. Duits; G. Jongbloed; M.-C. Lieshout; L. Davies, chapter 14, Springer London, 2012, ISBN 978-1-4471-2353-8, pp. 241–259, 10.1007/978-1-4471-2353-8_14. Available from: http://dx.doi.org/10.1007/978-1-4471-2353-8_14
- [10] Haindl, M.; Havlíček, V. A multiscale colour texture model. In *Proceedings of the 16th International Conference on Pattern Recognition*, edited by R. Kasturi; D. Laurendeau; C. Suen, Los Alamitos: IEEE Computer Society, August 2002, pp. 255–258. Available from: <http://dx.doi.org/10.1109/ICPR.2002.1044676>
- [11] Potts, R. B.; Domb, C. Some generalized order-disorder transformations. *Proceedings of the Cambridge Philosophical Society*, volume 48, 1952: p. 106, doi: 10.1017/S0305004100027419.
- [12] Wu, F. Y. The Potts model. *Rev. Mod. Phys.*, volume 54, no. 1, Jan 1982: pp. 235–268, doi:10.1103/RevModPhys.54.235.
- [13] Ising, E. Beitrag zur Theorie des Ferromagnetismus. *Zeitschrift fur Physik*, volume 31, Feb. 1925: pp. 253–258, doi:10.1007/BF02980577.
- [14] McCoy, B.M. and Wu, T.T. The Two-Dimensional Ising Model. 1973.
- [15] Levada, A. and Mascarenhas, N. and Tannus, A. Pseudolikelihood Equations for Potts MRF Model Parameter Estimation on Higher Order Neighborhood Systems. *Geoscience and Remote Sensing Letters, IEEE*, volume 5, no. 3, July 2008: pp. 522–526, ISSN 1545-598X, doi:10.1109/LGRS.2008.920909.
- [16] Levada, A. and Mascarenhas, N. and Tannus, A. Improving Potts MRF model parameter estimation using higher-order neighborhood systems on stochastic image modeling. In *Systems, Signals and Image Processing, 2008. IWSSIP 2008. 15th International Conference on*, 2008, pp. 385–388, doi:10.1109/IWSSIP.2008.4604447.
- [17] Frigessi, A. and Di Stefano, P. and Hwang, C.R. and Sheu, S.J. Convergence rates of the Gibbs sampler, the Metropolis algorithm and other single-site updating dynamics. *Journal of the Royal Statistical Society. Series B (Methodological)*, 1993: pp. 205–219.
- [18] Wolff, U. Collective Monte Carlo updating for spin systems. *Physical Review Letters*, volume 62, no. 4, 1989: p. 361.
- [19] Swendsen, R.H. and Wang, J.S. Nonuniversal critical dynamics in Monte Carlo simulations. *Physical Review Letters*, volume 58, no. 2, 1987: p. 86.

-
- [20] Dana, K. J.; Van Ginneken, B.; Nayar, S. K.; et al. Reflectance and texture of real-world surfaces. *ACM Transactions On Graphics (TOG)*, volume 18, no. 1, 1999: pp. 1–34.
- [21] Schlesinger, M. I. Relation between learning and self-learning in pattern recognition. *Kibernetika (Kiev)*, volume 6, no. 2, 1968: pp. 81–88.
- [22] Dempster, A. P.; Laird, N. M.; Rubin, D. B. Maximum likelihood from incomplete data via the EM algorithm. *Journal of the royal statistical society. Series B (methodological)*, 1977: pp. 1–38.
- [23] Kullback, S.; Leibler, R. A. On information and sufficiency. *The annals of mathematical statistics*, volume 22, no. 1, 1951: pp. 79–86.
- [24] Hershey, J. R.; Olsen, P. A. Approximating the Kullback Leibler divergence between Gaussian mixture models. In *Acoustics, Speech and Signal Processing, 2007. ICASSP 2007. IEEE International Conference on*, volume 4, IEEE, 2007, pp. IV–317.
- [25] Matas, J.; Chum, O.; Urban, M.; et al. Robust wide-baseline stereo from maximally stable extremal regions. *Image and vision computing*, volume 22, no. 10, 2004: pp. 761–767.
- [26] Neumann, L.; Matas, J. Real-time scene text localization and recognition. In *Computer Vision and Pattern Recognition (CVPR), 2012 IEEE Conference on*, IEEE, 2012, pp. 3538–3545.
- [27] of Radiology, A. C.; Committee, B.-R.; et al. *ACR BI-RADS breast imaging and reporting data system: breast imaging atlas*. American College of Radiology, 2003.
- [28] Abubaker, A. and Qahwaji, RS and Aqel, M.J. and Saleh, M.H. Average Row Thresholding Method for Mammogram Segmentation. In *Engineering in Medicine and Biology Society, 2005. IEEE-EMBS 2005. 27th Annual International Conference of the*, IEEE, 2006, pp. 3288–3291.
- [29] Wirth, M.; Nikitenko, D.; Lyon, J. Segmentation of the Breast Region in Mammograms using a Rule-Based Fuzzy Reasoning Algorithm. *ICGST International Journal on Graphics, Vision and Image Processing*, volume 05, January 2005: pp. 45–54.
- [30] Norhayati Ibrahim and Hiroshi Fujita and Takeshi Hara and Tokiko Endo. Automated detection of clustered microcalcifications on mammograms: CAD system application to MIAS database. *Physics in Medicine and Biology*, volume 42, no. 12, 1997: p. 2577. Available from: <http://stacks.iop.org/0031-9155/42/i=12/a=021>
- [31] Dengler, J.; Behrens, S.; Desaga, J. Segmentation of microcalcifications in mammograms. *Medical Imaging, IEEE Transactions on*, volume 12, no. 4, 1993: pp. 634–642.

- [32] Haindl, M. and Mikes, S. Unsupervised mammograms segmentation. In *Pattern Recognition, 2008. ICPR 2008. 19th International Conference on*, IEEE, 2008, pp. 1–4.
- [33] Haindl, M. and Mikeš, S. and Scarpa, G. Unsupervised detection of mammogram regions of interest. In *Knowledge-Based Intelligent Information and Engineering Systems*, Springer, 2007, pp. 33–40.
- [34] Grim, J. and Somol, P. and Haindl, M. and Danes, J. Computer-aided evaluation of screening mammograms based on local texture models. *Image Processing, IEEE Transactions on*, volume 18, no. 4, 2009: pp. 765–773.
- [35] He, W. and Muhimmah, I. and Denton, E. and Zwiggelaar, R. Mammographic segmentation based on texture modelling of tabar mammographic building blocks. *Digital Mammography*, 2008: pp. 17–24.
- [36] Tabár, L. and Tot, T. and Dean, P.B. *Breast cancer: the art and science of early detection with mammography: perception, interpretation, histopathologic correlation*. George Thieme Verlag, 2005.
- [37] Timp, S. and Karssemeijer, N. A new 2D segmentation method based on dynamic programming applied to computer aided detection in mammography. *Medical Physics*, volume 31, 2004: p. 958.
- [38] Kupinski, M.; Giger, M. Automated seeded lesion segmentation on digital mammograms. *Medical Imaging, IEEE Transactions on*, volume 17, no. 4, 1998: pp. 510–517.
- [39] Muhimmah, I.; Zwiggelaar, R. Mammographic density classification using multiresolution histogram information. In *Proceedings of the International Special Topic Conference on Information Technology in Biomedicine, ITAB*, Citeseer, 2006.
- [40] Muštra, M.; Grgić, M.; Delač, K. Breast density classification using multiple feature selection. *AUTOMATIKA: časopis za automatiku, mjerenje, elektroniku, računarstvo i komunikacije*, volume 53, no. 4, 2012: pp. 362–372.
- [41] Tang, J.; Liu, X.; Sun, Q. A Direct Image Contrast Enhancement Algorithm in the Wavelet Domain for Screening Mammograms. *Selected Topics in Signal Processing, IEEE Journal of*, volume 3, no. 1, Feb 2009: pp. 74–80, ISSN 1932-4553, doi:10.1109/JSTSP.2008.2011108.
- [42] Chang, C.-M.; Laine, A. Coherence of multiscale features for enhancement of digital mammograms. *IEEE Transactions on Information Technology in Biomedicine*, volume 3, no. 1, 1999: pp. 32–46.
- [43] Sakellaropoulos, P.; Costaridou, L.; Panayiotakis, G. A wavelet-based spatially adaptive method for mammographic contrast enhancement. *Physics in medicine and biology*, volume 48, no. 6, 2003: p. 787.

-
- [44] Mencattini, A.; Caselli, F.; Salmeri, M.; et al. Wavelet based adaptive algorithm for mammographic images enhancement and denoising. In *Image Processing, 2005. ICIP 2005. IEEE International Conference on*, volume 1, IEEE, 2005, pp. I–1141.
- [45] Dhawan, A. P.; Buelloni, G.; Gordon, R. Enhancement of mammographic features by optimal adaptive neighborhood image processing. *IEEE Transactions on Medical Imaging*, volume 5, no. 1, 1986: pp. 8–15.
- [46] Grim, J.; Somol, P.; Haindl, M.; et al. Computer-Aided Evaluation of Screening Mammograms Based on Local Texture Models. *IEEE Transactions on Image Processing*, volume 18, no. 4, 2009: pp. 765 – 773, ISSN 1057-7149, doi: <http://doi.ieeecomputersociety.org/10.1109/TIP.2008.2011168>.
- [47] Dippel, S.; Stahl, M.; Wiemker, R.; et al. Multiscale contrast enhancement for radiographies: Laplacian pyramid versus fast wavelet transform. *Medical Imaging, IEEE Transactions on*, volume 21, no. 4, 2002: pp. 343–353.
- [48] Salvado, J.; Roque, B. Detection of calcifications in digital mammograms using wavelet analysis and contrast enhancement. In *Intelligent Signal Processing, 2005 IEEE International Workshop on*, IEEE, 2005, pp. 200–205.
- [49] Yan, Z.; Zhang, Y.; Liu, B.; et al. Extracting hidden visual information from mammography images using conjugate image enhancement software. In *Information Acquisition, 2005 IEEE International Conference on*, IEEE Engineering in Medicine and Biology Society, IEEE, Aug. 2005, pp. 4775 – 4778.
- [50] Thangavel, K.; Karnan, M.; Sivakumar, R.; et al. CAD System for Preprocessing and Enhancement of Digital Mammograms. *Graphics, Vision and Image Processing*, 2007: pp. 55–60. Available from: <http://www.icgst.com/gvip/v7/P1150527002.html>
- [51] Mencattini, A.; Salmeri, M.; Lojacono, R.; et al. Mammographic images enhancement and denoising for breast cancer detection using dyadic wavelet processing. *Instrumentation and Measurement, IEEE Transactions on*, volume 57, no. 7, 2008: pp. 1422–1430.
- [52] Pratt, W. K. *Digital image processing: PIKS inside*. John Wiley & Sons, Inc, 2007, ISBN 978-0-471-76777-0.
- [53] Wang, H.; Li, J.-B.; Wu, L.; et al. Mammography visual enhancement in CAD-based breast cancer diagnosis. *Clinical imaging*, volume 37, no. 2, 2013: pp. 273–282.
- [54] Panetta, K.; Zhou, Y.; Agaian, S.; et al. Nonlinear unsharp masking for mammogram enhancement. *Information Technology in Biomedicine, IEEE Transactions on*, volume 15, no. 6, 2011: pp. 918–928.

- [55] Bhateja, V.; Misra, M.; Urooj, S. Non-linear polynomial filters for edge enhancement of mammogram lesions. *Computer methods and programs in biomedicine*, volume 129, 2016: pp. 125–134.
- [56] Georgsson, F.; Olsn, C. The accuracy of geometric approximation of the mamilla in mammograms. In *CARS'03*, 2003, pp. 956–961.
- [57] Samulski, M. and Karssemeijer, N. Matching mammographic regions in mediolateral oblique and cranio caudal views: A probabilistic approach. In *Proceedings of SPIE, Medical Imaging*, volume 6915, 2008.
- [58] Yang, Sheng-Chih and Hsu, Hsian-He and Hsu, Giu-Cheng and Chung, Pau-Choo and Guo, Shu-Mei and Lo, Chien-Shen and Yang, Ching-Wen and Lee, San-Kan and Chang, Chein-I. 3D localization of clustered microcalcifications using cranio-caudal and medio-lateral oblique views. *Computerized medical imaging and graphics the official journal of the Computerized Medical Imaging Society*, volume 29, no. 7, 2005: pp. 521–532. Available from: <http://www.ncbi.nlm.nih.gov/pubmed/15996852>
- [59] Marias, K.; Behrenbruch, C. P.; Brady, M.; et al. Multi-scale landmark selection for improved registration of temporal mammograms. In *International Workshop on Database Machines*, 2000.
- [60] Marias, K. and Behrenbruch, C. and Parbhoo, S. and Seifalian, A. and Brady, M. A registration framework for the comparison of mammogram sequences. *Medical Imaging, IEEE Transactions on*, volume 24, no. 6, June 2005: pp. 782–790, ISSN 0278-0062, doi:10.1109/TMI.2005.848374.
- [61] Harder, R L and Desmarais, R N. Interpolation using surface splines. *Journal of Aircraft*, volume 9, no. 2, 1972: pp. 189–191. Available from: <http://www.mendeley.com/research/interpolation-using-surface-splines-1/>
- [62] Highnam, R.P. and Brady, J.M. and Shepstone, B.J. In *Digital Mammography, IEE Colloquium on*, title=*A representation for mammographic image processing*, mar 1996, pp. 4/1 –4/6, doi:10.1049/ic:19960487.
- [63] Highnam, R. and Pan, X. and Warren, R. and Jeffreys, M. and Davey Smith, G. and Brady, M. Breast composition measurements using retrospective standard mammogram form (SMF). *Physics in medicine and biology*, volume 51, 2006: p. 2695.
- [64] Wirth, M. A.; Narhan, J.; Gray, D. A model for nonrigid mammogram registration using mutual information. In *In International Workshop on Digital Mammography*, 2002.
- [65] Timp, S. A regional registration method to find corresponding mass lesions in temporal mammogram pairs. *Medical Physics*, volume 32, 2005: p. 2629, doi: 10.1118/1.1984323.

-
- [66] Hachama, M. and Richard, F. and Desolneux, A. A mammogram registration technique dealing with outliers. In *Biomedical Imaging: Nano to Macro, 2006. 3rd IEEE International Symposium on*, April 2006, pp. 458–461, doi:10.1109/ISBI.2006.1624952.
- [67] Georgsson, F. Anatomical coordinate system for bilateral registration of mammograms. In *Proceedings of the 13th Scandinavian conference on Image analysis, SCIA'03*, Berlin, Heidelberg: Springer-Verlag, 2003, ISBN 3-540-40601-8, pp. 335–342. Available from: <http://dl.acm.org/citation.cfm?id=1763974.1764026>
- [68] Reig-Bolao, R.; Baradad, V.; Marti-Puig, P. A Contour Based Approach for Bilateral Mammogram Registration Using Discrete Wavelet Analysis. In *International Symposium on Distributed Computing and Artificial Intelligence 2008 (DCAI 2008), Advances in Soft Computing*, volume 50, edited by J. Corchado; S. Rodriguez; J. Llinas; J. Molina, Springer Berlin / Heidelberg, 2009, ISBN 978-3-540-85862-1, pp. 347–356. Available from: http://dx.doi.org/10.1007/978-3-540-85863-8_41
- [69] Simone, G.; Pedersen, M.; Hardeberg, J. Y. Measuring perceptual contrast in digital images. *Journal of Visual Communication and Image Representation*, volume 23, no. 3, 2012: pp. 491–506.
- [70] Weber, E. H. *The Sense of Touch*. Academic Press, 1978.
- [71] Michelson, A. A. *Studies in Optics*. Chicago, Illinois: University of Chicago Press, 1927.
- [72] Burkhardt, D. A.; Gottesman, J.; Kersten, D.; et al. Symmetry and constancy in the perception of negative and positive luminance contrast. *JOSA A*, volume 1, no. 3, 1984: pp. 309–316.
- [73] King-Smith, P. E.; Kulikowski, J. Pattern and flicker detection analysed by sub-threshold summation. *The Journal of physiology*, volume 249, no. 3, 1975: p. 519.
- [74] Whittle, P. Increments and decrements: Luminance discrimination. *Vision research*, volume 26, no. 10, 1986: pp. 1677–1691.
- [75] Agaian, S. S.; Panetta, K.; Grigoryan, A. M. Transform-based image enhancement algorithms with performance measure. *IEEE Transactions on Image Processing*, volume 10, no. 3, Mar 2001: pp. 367–382, ISSN 1057-7149, doi:10.1109/83.908502.
- [76] Agaian, S. S.; Silver, B.; Panetta, K. A. Transform Coefficient Histogram-Based Image Enhancement Algorithms Using Contrast Entropy. *IEEE Transactions on Image Processing*, volume 16, no. 3, March 2007: pp. 741–758, ISSN 1057-7149, doi:10.1109/TIP.2006.888338.

- [77] Tadmor, Y.; Tolhurst, D. Calculating the contrasts that retinal ganglion cells and {LGN} neurones encounter in natural scenes. *Vision Research*, volume 40, no. 22, 2000: pp. 3145 – 3157, ISSN 0042-6989, doi:[http://dx.doi.org/10.1016/S0042-6989\(00\)00166-8](http://dx.doi.org/10.1016/S0042-6989(00)00166-8). Available from: <http://www.sciencedirect.com/science/article/pii/S0042698900001668>
- [78] Simone, G.; Pedersen, M.; Hardeberg, J. Y. Measuring perceptual contrast in digital images. *Journal of Visual Communication and Image Representation*, volume 23, no. 3, 2012: pp. 491–506.
- [79] Levine, M. D.; Nazif, A. M. Dynamic Measurement of Computer Generated Image Segmentations. *IEEE Transactions on Pattern Analysis and Machine Intelligence*, volume 7, 1985: pp. 155–164.
- [80] Erdem, Ç. E.; Sankur, B.; et al. Performance measures for video object segmentation and tracking. *Image Processing, IEEE Transactions on*, volume 13, no. 7, 2004: pp. 937–951.
- [81] Haindl, M. Texture synthesis. *CWI Quarterly*, volume 4, no. 4, December 1991: pp. 305–331.
- [82] Suckling, J.; Parker, J.; Dance, D.; et al. The mammographic image analysis society digital mammogram database. In *2nd International Workshop on Digital Mammography*, International Congress Series, Excerta Medica, 1994, pp. 1069: 375–378.
- [83] LLNL. Lawrence Livermore National Library / UCSF Digital Mammogram Database. Technical report, Center for Health Care Technologies Livermore, Lawrence Livermore National Library, Livermore, CA, USA, 1995.
- [84] Heath, M.; Bowyer, K.; Kopans, D.; et al. The Digital Database for Screening Mammography. In *Proc. of the 5th Int. Workshop on Digital Mammography*, Medical Physics Publishing, June 2000.
- [85] Oliveira, J. E.; Gueld, M. O.; Araújo, A. d. A.; et al. Toward a standard reference database for computer-aided mammography. In *Medical Imaging*, International Society for Optics and Photonics, 2008, pp. 69151Y–69151Y.
- [86] Moreira, I. C.; Amaral, I.; Domingues, I.; et al. INbreast: toward a full-field digital mammographic database. *Academic radiology*, volume 19, no. 2, 2012: pp. 236–248.
- [87] Patel, M.; Looney, P.; Young, K.; et al. Automated collection of medical images for research from heterogeneous systems: trials and tribulations. In *SPIE Medical Imaging*, International Society for Optics and Photonics, 2014, pp. 90390C–90390C.
- [88] Matheus, B. R. N.; Schiabel, H. Online mammographic images database for development and comparison of CAD schemes. *Journal of digital imaging*, volume 24, no. 3, 2011: pp. 500–506.

-
- [89] Haindl, M.; Havlíček, V. A multiscale colour texture model. In *Pattern Recognition, 2002. Proceedings. 16th International Conference on*, volume 1, IEEE, 2002, pp. 255–258.
- [90] Levada, A.; Mascarenhas, N.; Tannus, A. Pseudolikelihood Equations for Potts MRF Model Parameter Estimation on Higher Order Neighborhood Systems. *Geoscience and Remote Sensing Letters, IEEE*, volume 5, no. 3, July 2008: pp. 522–526, ISSN 1545-598X, doi:10.1109/LGRS.2008.920909.
- [91] Haindl, M.; Mikeš, S.; Pudil, P. Unsupervised Hierarchical Weighted Multi-Segmenter. In *Lecture Notes in Computer Science, MCS 2009*, volume 5519 (2009), edited by J. Benediktsson; J. Kittler; F. Roli, Springer, 2009, ISBN 978-3-642-02325-5, ISSN 0302-9743, pp. 272–282, doi:http://dx.doi.org/.
- [92] Haindl, M.; Mikeš, S. Texture Segmentation Benchmark. In *Proceedings of the 19th International Conference on Pattern Recognition, ICPR 2008*, edited by B. Lovell; D. Laurendeau; R. Duin, Los Alamitos: IEEE Computer Society, December 2008, ISBN 978-1-4244-2174-9, ISSN 1051-4651, pp. 1–4, doi:http://dx.doi.org/10.1109/ICPR.2008.4761118. Available from: <http://doi.ieeecomputersociety.org/>
- [93] Jeng, F.-C.; Woods, J. W. Compound Gauss-Markov Random Fields for Image Estimation. *IEEE Transactions on Signal Processing*, volume 39, no. 3, 1991: pp. 683–697.
- [94] Geman, S.; Geman, D. Stochastic Relaxation, Gibbs Distributions and Bayesian Restoration of Images. *IEEE Transactions on Pattern Analysis and Machine Intelligence*, volume 6, no. 11, November 1984: pp. 721–741.
- [95] Figueiredo, M.; Leitao, J. Unsupervised image restoration and edge location using compound Gauss - Markov random fields and the MDL principle. *Image Processing, IEEE Transactions on*, volume 6, no. 8, April 1997: pp. 1089–1102.
- [96] Molina, R.; Mateos, J.; Katsaggelos, A.; et al. Bayesian Multichannel Image Restoration Using Compound Gauss-Markov Random Fields. *IEEE Trans. Image Proc.*, volume 12, no. 12, December 2003: pp. 1642–1654.
- [97] Wu, J.; Chung, A. C. S. A Segmentation Model Using Compound Markov Random Fields Based on a Boundary Model. *IEEE Trans. Image Processing*, volume 16, no. 1, Jan 2007: pp. 241–252.
- [98] Haindl, M.; Havlíček, V. A Compound MRF Texture Model. In *Proceedings of the 20th International Conference on Pattern Recognition, ICPR 2010*, Los Alamitos: IEEE Computer Society CPS, August 2010, ISBN 13: 978-0-7695-4109-9, ISSN 1051-4651, pp. 1792–1795, doi:10.1109/ICPR.2010.442. Available from: <http://doi.ieeecomputersociety.org/10.1109/ICPR.2010.442>

- [99] Haindl, M.; Havlíček, V. A Plausible Texture Enlargement and Editing Compound Markovian Model. In *Computational Intelligence for Multimedia Understanding, Lecture Notes in Computer Science*, volume 7252, edited by E. Salerno; A. etin; O. Salvetti, Springer Berlin / Heidelberg, 2012, ISBN 978-3-642-32435-2, pp. 138–148, doi:http://dx.doi.org/10.1007/978-3-642-32436-9_12, 10.1007/978-3-642-32436-9_12. Available from: <http://www.springerlink.com/content/047124j43073m202/>
- [100] Swendsen, R. H.; Wang, J.-S. Nonuniversal critical dynamics in Monte Carlo simulations. *Phys. Rev. Lett.*, volume 58, no. 2, Jan 1987: pp. 86–88, doi:10.1103/PhysRevLett.58.86.
- [101] Ahuja, N.; Schachter, B. *Pattern models*. J. Wiley, 1983, ISBN 0-471-86194-4.
- [102] Aurenhammer, F. Voronoi diagrams a survey of a fundamental geometric data structure. *ACM Computing Surveys (CSUR)*, volume 23, no. 3, 1991: pp. 345–405.
- [103] Potts, R.; Domb, C. Some generalized order-disorder transformations. In *Proceedings of the Cambridge Philosophical Society*, volume 48, 1952, pp. 106–109.
- [104] Wu, F. The Potts model. *Reviews of modern physics*, volume 54, no. 1, 1982: pp. 235–268.
- [105] Metropolis, N.; Rosenbluth, A. W.; Rosenbluth, M. N.; et al. Equation of State Calculations by Fast Computing Machines. *Journal of Chemical Physics*, volume 21, 1953: pp. 1087–1092.
- [106] Haindl, M.; Havlíček, V. A Multiresolution Causal Colour Texture Model. *Lecture Notes in Computer Science*, , no. 1876, August 2000: pp. 114–122, ISSN 0302-9743.
- [107] Haindl, M.; Filip, J. Extreme Compression and Modeling of Bidirectional Texture Function. *IEEE Transactions on Pattern Analysis and Machine Intelligence*, volume 29, no. 10, 2007: pp. 1859–1865, ISSN 0162-8828, doi:<http://doi.ieeecomputersociety.org/10.1109/TPAMI.2007.1139>.
- [108] Carney, P. A.; Miglioretti, D. L.; Yankaskas, B. C.; et al. Individual and Combined Effects of Age, Breast Density, and Hormone Replacement Therapy Use on the Accuracy of Screening Mammography. *Annals of Internal Medicine*, volume 138, no. 3, 2003: pp. 168–175, doi:10.7326/0003-4819-138-3-200302040-00008. Available from: [+http://dx.doi.org/10.7326/0003-4819-138-3-200302040-00008](http://dx.doi.org/10.7326/0003-4819-138-3-200302040-00008)
- [109] Karssemeijer, N. Automated classification of parenchymal patterns in mammograms. *Physics in medicine and biology*, volume 43, no. 2, 1998: p. 365.
- [110] Bovis, K.; Singh, S. Classification of mammographic breast density using a combined classifier paradigm. In *Medical Image Understanding and Analysis (MIUA) Conference, Portsmouth, Citeseer, 2002*.

- [111] Oliver, A.; Freixenet, J.; Zwiggelaar, R. Automatic classification of breast density. In *Image Processing, 2005. ICIIP 2005. IEEE International Conference on*, volume 2, IEEE, 2005, pp. II-1258.
- [112] Oliver, A.; Freixenet, J.; Marti, R.; et al. A novel breast tissue density classification methodology. *Information Technology in Biomedicine, IEEE Transactions on*, volume 12, no. 1, 2008: pp. 55-65.
- [113] Torrent, A.; Bardera, A.; Oliver, A.; et al. Breast density segmentation: a comparison of clustering and region based techniques. In *Digital Mammography*, Springer, 2008, pp. 9-16.
- [114] Besag, J. On the statistical analysis of dirty pictures. *Journal of the Royal Statistical Society. Series B (Methodological)*, 1986: pp. 259-302.
- [115] Taylor, P. and Champness, J. and Given-Wilson, R. and Johnston, K. and Potts, H. Impact of computer-aided detection prompts on the sensitivity and specificity of screening mammography. *Health Technology Assessment*, volume 9, no. 6, 2005.

Reviewed Publications of the Author Relevant to the Thesis

- [A.1] Haindl, M.; Remeš, V.; Havlíček, V. Potts Compound Markovian Texture Model. In *Proceedings of the 21st International Conference on Pattern Recognition, ICPR 2012*, Los Alamitos: IEEE Computer Society CPS, November 2012, ISBN 978-4-9906441-1-6, pp. 29 – 32.
- [A.2] Haindl, M.; Remeš, V. *Efficient Textural Model-Based Mammogram Enhancement*. In *2013 IEEE 26th International Symposium on Computer-Based Medical Systems (CBMS)*, edited by P. P. Rodrigues; M. Pechenizkiy; J. ao Gama; R. Cruz-Correia; J. Liu; A. Traina; P. Lucas; P. Soda, Hoes Lane, P.O. Box 1331, Piscataway, NJ 08855-1331, USA: IEEE, June 2013, ISBN 978-1-4799-1053-3, pp. 522–523, doi:10.1109/CBMS.2013.6627859.
- [A.3] Haindl, M.; Remeš, V. Adaptive Model-Based Mammogram Enhancement. In *Signal-Image Technology and Internet-Based Systems (SITIS), 2014 Tenth International Conference on*, IEEE, 2014, pp. 65–72.
- [A.4] Haindl, M.; Remeš, V.; Havlíček, V. BTF Potts compound texture model. In *IS&T/SPIE Electronic Imaging*, International Society for Optics and Photonics, 2015, pp. 939807–939807.
- [A.5] Haindl, M.; Remeš, V. Digital Mammogram Enhancement. In *Mammography Techniques and Review*, InTech, 2015.
- [A.6] Remeš, V.; Haindl, M. Classification of breast density in X-ray mammography. In *Computational Intelligence for Multimedia Understanding (IWCIM), 2015 International Workshop on*, IEEE, 2015, pp. 1–5.

Journal papers under review:

- [A.7] Remeš, V.; Haindl, M. Image contrast criteria validation. In *Kybernetika*.
- [A.8] Remeš, V.; Haindl, M. Mammogram texture enhancement with multichannel output. In *IET Image Processing*.

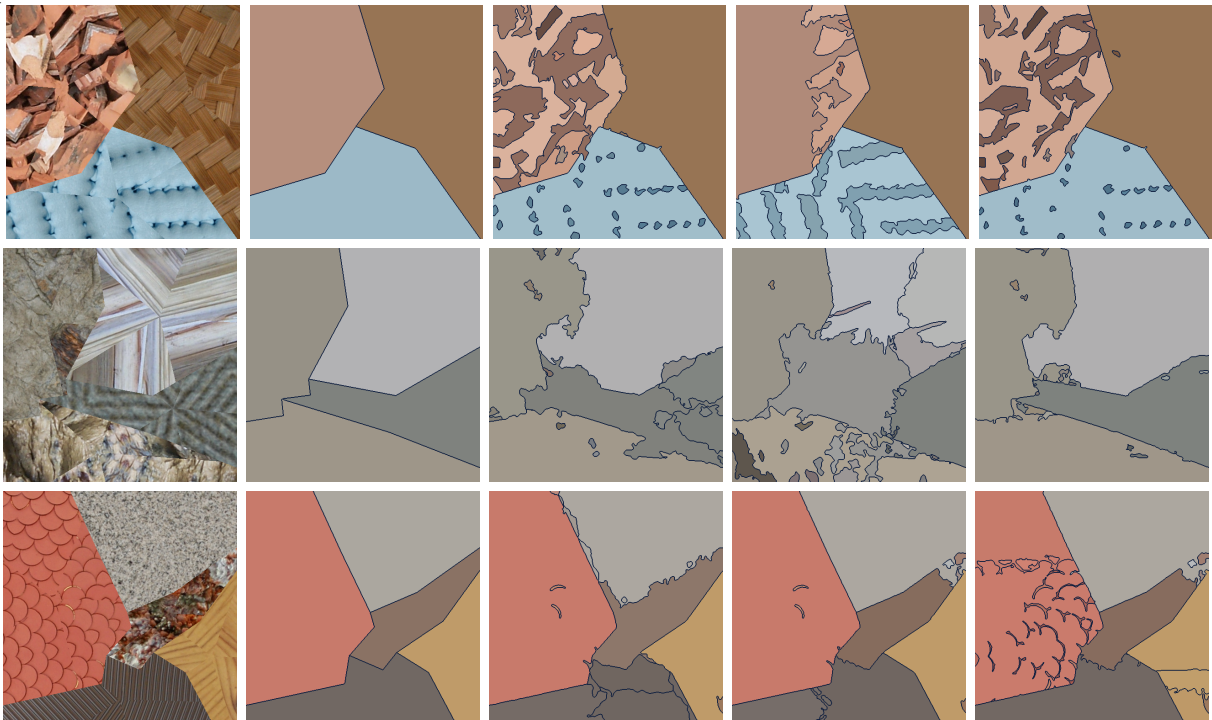
Remaining Publications of the Author Relevant to the Thesis

- [A.9] Václav Remeš *Digital analysis of mammograms*. Ph.D. Minimum Thesis, Faculty of Information Technology, Prague, Czech Republic, 2012.
- [A.10] Václav Remeš, Michal Haindl *Potts Model-Based Texture Synthesis*. Poster at 7th International Workshop Data - Algorithms - Decision Making, Mariánská, Czech Republic 2011.

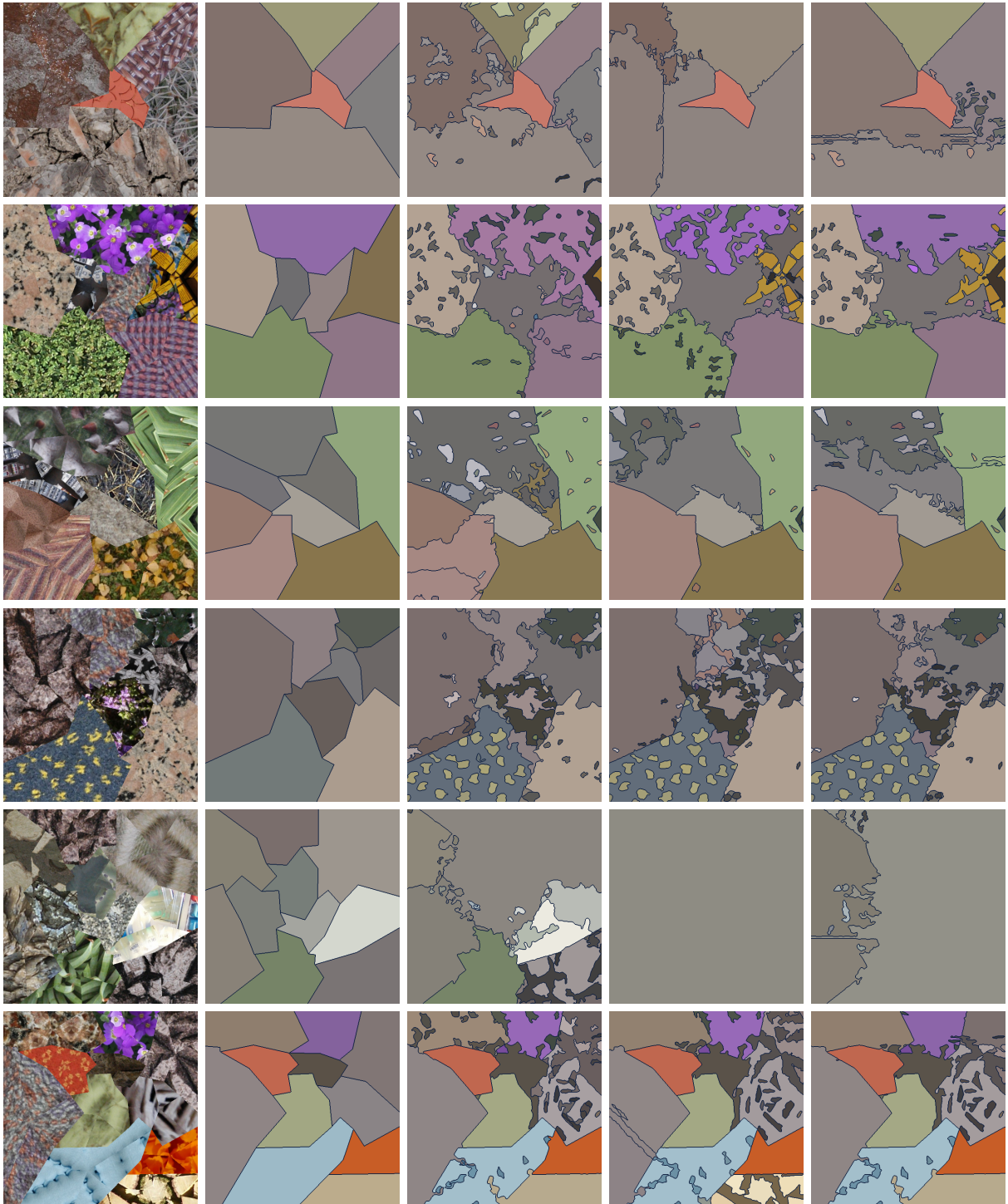
Unsupervised segmentation results

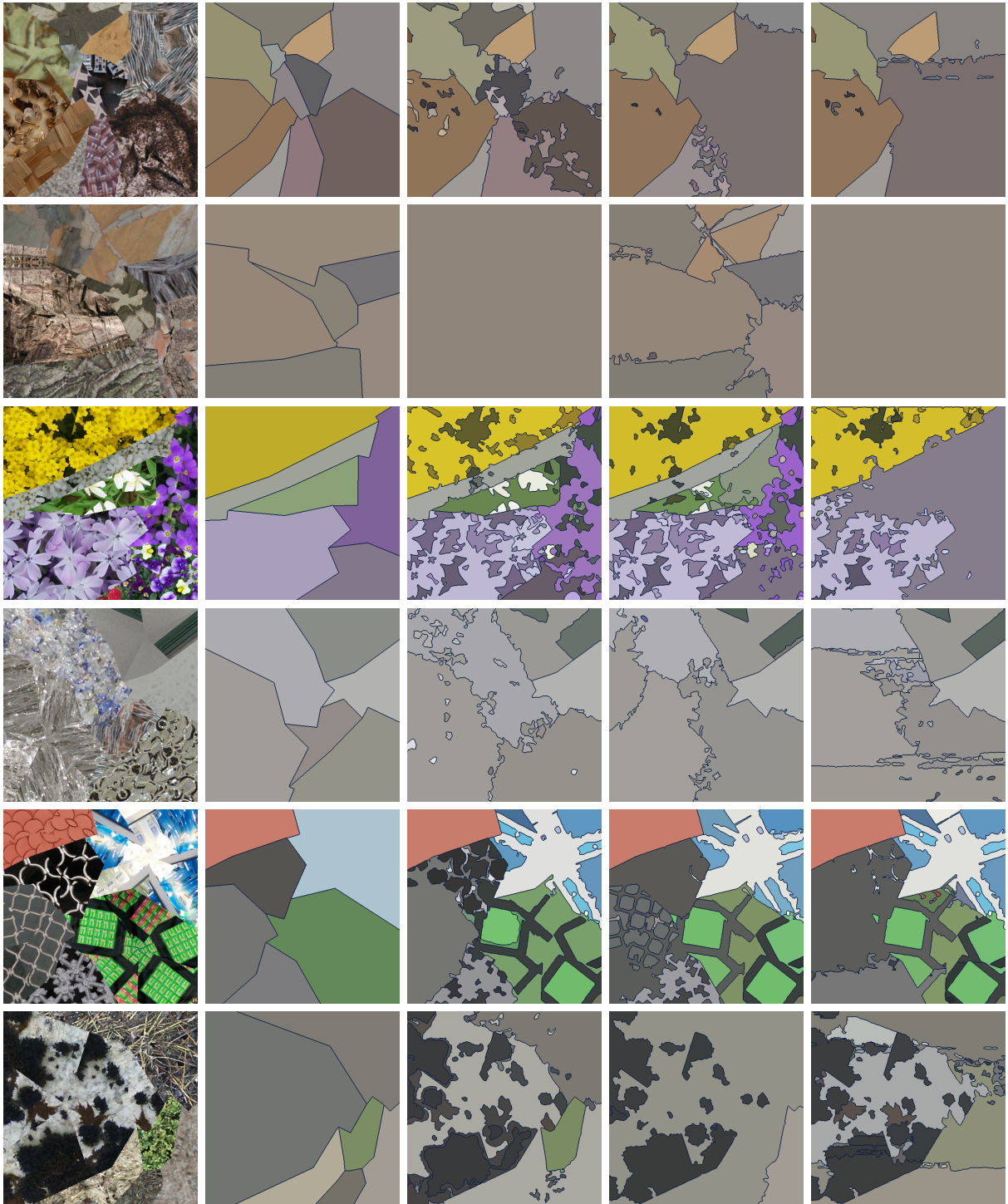
Here are the preliminary results of using our proposed spiral and directional 3DCAR model when used as features for unsupervised segmentation using the method published in [91], compared to just 3DCAR features.

Left to right: segmented image, ground truth, segmentation based on spiral 3DCAR features, segmentation based on multidirectional 3DCAR features, segmentation based on pure 3DCAR features.



A. UNSUPERVISED SEGMENTATION RESULTS





A. UNSUPERVISED SEGMENTATION RESULTS

